



저작자표시-비영리-변경금지 2.0 대한민국

이용자는 아래의 조건을 따르는 경우에 한하여 자유롭게

- 이 저작물을 복제, 배포, 전송, 전시, 공연 및 방송할 수 있습니다.

다음과 같은 조건을 따라야 합니다:



저작자표시. 귀하는 원저작자를 표시하여야 합니다.



비영리. 귀하는 이 저작물을 영리 목적으로 이용할 수 없습니다.



변경금지. 귀하는 이 저작물을 개작, 변형 또는 가공할 수 없습니다.

- 귀하는, 이 저작물의 재이용이나 배포의 경우, 이 저작물에 적용된 이용허락조건을 명확하게 나타내어야 합니다.
- 저작권자로부터 별도의 허가를 받으면 이러한 조건들은 적용되지 않습니다.

저작권법에 따른 이용자의 권리는 위의 내용에 의하여 영향을 받지 않습니다.

이것은 [이용허락규약\(Legal Code\)](#)을 이해하기 쉽게 요약한 것입니다.

[Disclaimer](#)

Thesis for the Degree of Ph.D. in Engineering

**산화아연 나노입자의 표면 개선을 통한 광촉매  
특성 향상**

**Surface modification of zinc oxide  
nanoparticles for improved photocatalytic  
properties**

**The Graduate School of The University of Ulsan  
School of Chemical Engineering**

**Chatchai Rodwihok**

June 2020

산화아연 나노입자의 표면 개선을 통한 광촉매 특성 향상

**Surface modification of zinc oxide nanoparticles for  
improved photocatalytic properties**

Supervised by Professor Jin Suk Chung

A Dissertation

Submitted to

The Graduate School of the University of Ulsan

In Partial Fulfillment of the Requirement

for the Degree of

Doctor of Philosophy

by

Chatchai Rodwihok

School of Chemical Engineering

Ulsan, South Korea

June 2020

산화아연 나노입자의 표면 개선을 통한 광촉매 특성 향상

**Surface modification of zinc oxide nanoparticles for  
improved photocatalytic properties**

Chatchai Rodwihok

School of Chemical Engineering, Major in Chemical Engineering  
The Graduate School

Supervised by Professor Jin Suk Chung

Approved as a qualified thesis of Chatchai Rodwihok  
for the degree of Ph.D. by the Evaluation Committee

June, 2020

Chairman: Prof. Seung Hyun Hur

Prof. Jin Suk Chung

Prof. Won Mook Choi

Prof. Eun Woo Shin

Prof. Jung Kyoo Lee

**The Graduate School  
University of Ulsan**



# Contents

<b>Acknowledgement</b>	<b>iv</b>
<b>List of Tables</b>	<b>v</b>
<b>List of Figures</b>	<b>vii</b>
<b>Abstract in English</b>	<b>xi</b>
<b>Abstract in Korean (국문 요약)</b>	<b>xiii</b>
<b>1 Introduction</b>	<b>1</b>
<b>2 Literature reviews</b>	<b>5</b>
2.1 Zinc oxide (ZnO) . . . . .	5
2.2 ZnO as a photocatalyst . . . . .	6
2.3 Modification strategies for photocatalytic performance improvement . . . . .	9
2.3.1 Metal/nonmetal doping . . . . .	10
2.3.2 ZnO coupling with carbonaceous groups . . . . .	15
2.3.3 Specific charge and polar molecule functionalization . . . . .	18
2.4 Research objective . . . . .	19
<b>3 The Effect of GO Additive in Zinc Oxide/ Reduced Graphene Oxide Nanocomposites with Enhanced Photosensitivity and Photocatalytic Activity</b>	<b>21</b>
3.1 Introduction . . . . .	21
3.2 Experimental details . . . . .	23
3.2.1 Materials . . . . .	23

3.2.2	Preparation of ZnO/rGO nanocomposites . . . . .	23
3.2.3	Characterization of ZnO/rGO nanocomposites . . . . .	26
3.2.4	UV sensing measurement . . . . .	26
3.2.5	Evaluation of photocatalytic degradation . . . . .	27
3.3	Results and discussions . . . . .	28
3.3.1	Structural component, surface morphology, and optical properties . . . . .	28
3.3.2	UV Sensing Measurement . . . . .	40
3.3.3	Photocatalytic Activity Studies . . . . .	45
3.4	Conclusions . . . . .	50
3.5	Supporting informations . . . . .	51

**4 Cerium-Oxide-Nanoparticle-Decorated Zinc Oxide with Enhanced Photocatalytic Degradation of Methyl Orange 55**

4.1	Introduction . . . . .	55
4.2	Experimental Details . . . . .	56
4.2.1	Preparation of Ce/ZnO Nanocomposites . . . . .	57
4.2.2	Material Characterization . . . . .	57
4.2.3	Evaluation of Photocatalytic Activity . . . . .	58
4.3	Results and Discussion . . . . .	58
4.3.1	Surface morphology, surface composition and optical properties . . . . .	58
4.3.2	Photocatalytic Activity Studies . . . . .	68
4.4	Conclusions . . . . .	74
4.5	Supporting informations . . . . .	76

<b>5</b>	<b>Surface Charge Modification of ZnO Nanoparticles Using Aniline with Improved Photodegradation Performance</b>	<b>80</b>
5.1	Introduction . . . . .	80
5.2	Experimental Details . . . . .	81
5.2.1	Preparation of ZnO Nanoparticles . . . . .	81
5.2.2	Functionalization of aniline on ZnO nanoparticles . . . . .	82
5.2.3	Material Characterization . . . . .	82
5.2.4	Evaluation of Photocatalytic Activity . . . . .	82
5.3	Results and Discussions . . . . .	83
5.3.1	Surface morphology and crystalline structure studies . . . . .	83
5.3.2	Surface composition analysis . . . . .	86
5.3.3	Optical property studies . . . . .	88
5.3.4	Photocatalytic activity of aniline functionalized ZnO . . . . .	89
5.4	Conclusions . . . . .	91
5.5	Supporting informations . . . . .	93
<b>6</b>	<b>Conclusions</b>	<b>95</b>
	<b>References</b>	<b>97</b>
	<b>Biography</b>	<b>124</b>

## **Acknowledgement**

This work has been done with the help of many people. I wish like to thank all of them. Firstly, I would like to express my appreciation to my advisor, Prof. Jin Suk Chung for opportunity to conduct my PhD and for his advice and supports. Without his help and encouragement, his thesis might never be completed.

I appreciate to Prof. Eun Woo Shin, Prof. Seung Hyun Hur and Prof. Won Mook Choi, for giving me a lot of comments and suggestions to improve my current work and future research.

I would like to thank Asst. Prof. Duangmanee Wongratanaphisan for her endless support including research advice and moral support. Without her, this thesis would never have come to completion.

I am thankful to our lab members including Yuanyuan Li, Yiming Meng, and Dang Thanh Truong for mental support and giving me a lot of suggestions to improve my research. I am also grateful to all of my colleagues for experimental and technical support.

Most of all, I would like to give a special thank to my family and friends who never give up on me and always give me a spirit, love, and moral support. Without them, this thesis never have been completed. Finally, I would like to thank for the most valuable experience to study and live in South Korea via supporting from Global Korea Scholarship.

Chatchai Rodwihok

## List of Tables

Table 1	General properties of ZnO. . . . .	6
Table 2	Overview of various dopants in the ZnO nanostructures with their synthesis techniques, operated photocatalytic conditions and photocatalytic performances (1). . . . .	13
Table 3	Overview of various dopants in the ZnO nanostructures with their synthesis techniques, operated photocatalytic conditions and photocatalytic performances (2). . . . .	14
Table 4	Overview of various carbonaceous group in the ZnO nanostructures with their synthesis techniques, operated photocatalytic conditions and photocatalytic performances. . . . .	17
Table 5	Average diameter, length, crystal size, lattice parameter of GO and as-synthesized samples. . . . .	30
Table 6	Raman spectra peak of GO and as-synthesized samples. . . . .	38
Table 7	Atomic percentage of fitted high-resolution spectra of the O 1s of ZnO/rGO nanocomposites and pristine ZnO. . . . .	39
Table 8	Photosensitivity (increase/decrease percentage) of UV sensing and photocatalytic properties based on ZnO/rGO nanocomposites. . . . .	49
Table 9	Comparisons of photosensitivity and time-dependent photocurrent response between the present work and other reported UV detectors. . . . .	53
Table 10	Comparisons of photocatalytic activity between the present work and other reported researchs. . . . .	54

Table 11 Lattice parameters, crystalline sizes, average particle sizes, and optical energy band gaps. . . . .	63
Table 12 Summary of the first- and second-order kinetic adsorption rate constants and correlation coefficients of photocatalytic degradation of methyl orange based on the pristine ZnO and Ce/ZnO catalysts. . .	74
Table 13 Calculated crystal size from several reflection planes of pristine ZnO and Ce/ZnO samples. . . . .	78
Table 14 XPS peak position and %area of ZnO and 7%Ce/ZnO nanocomposites. . . . .	78
Table 15 The comparison of photocatalytic MO degradation activity based on Ce/ZnO catalysts. . . . .	79
Table 16 Summaries of crystal information, and surface charge. . . . .	84
Table 17 Optical energy band gap and photocatalytic performance. . . . .	91

## List of Figures

Fig. 1	Heterogeneous photocatalytic oxidation step [31]. . . . .	7
Fig. 2	Degradation of organic pollutant by ZnO under sunlight [31]. . . . .	9
Fig. 3	Synthesis of reduced graphene oxide (rGO): (A) oxidation of graphite to graphene oxide, (B) reduction of graphene oxide to reduced graphene oxide [66]. . . . .	15
Fig. 4	(a) The preparation process of ZnO/rGO nanocomposites, (b) UV sensing measurement, and (c) photocatalytic experiment. . . . .	25
Fig. 5	XRD pattern of GO and as-synthesized ZnO/rGO. . . . .	29
Fig. 6	Field-emission scanning electron microscopy (FE-SEM) images of the (a) GO sheet, (b) ZnO, (c) ZnO/rGO (10%), (d) ZnO/rGO 20%, and (e) ZnO/rGO ZnO/rGO (30%). The inset shows the high magnification of FE-SEM image for each condition. . . . .	29
Fig. 7	Surface characterization of ZnO/rGO. (a) FT-IR spectra and Raman spectra, (b) ZnO component, and (c) GO component. . . . .	32
Fig. 8	UV-visible spectroscopy of as-synthesized ZnO/rGO: (a) absorption spectra and (b) energy band gap. . . . .	34
Fig. 9	(a) The X-ray photoelectron spectroscopy (XPS) survey spectra obtained for GO. The deconvoluted (b) C 1s and (c) O 1s of GO, pristine ZnO, and as-synthesized ZnO/rGO. . . . .	37
Fig. 10	(a) Current-time (I-t) of ZnO/rGO, (b) I-V characteristic of as-synthesized ZnO/rGO without bending strain, (c) Current-time (I-t) of ZnO/rGO (20%) with bending radius and. (d) comparison of photosensitivity. . . . .	42

Fig. 11 (UV sensing mechanism of as-synthesized ZnO/rGO (a) without, and (b) with bending strain. . . . .	44
Fig. 12 (a) Photodegradation of methylene blue (MB) in the presence of various photocatalysts under visible light illustration, (b) apparent first-order kinetics of photocatalytic degradation of MB, and (c) the effect of GO concentration on photocatalytic reaction rate constant and defect evaluation values. . . . .	46
Fig. 13 Schematic diagram of photo-charge generation and charge transfer for MB degradation using as-synthesized ZnO/rGO. . . . .	48
Fig. 14 The thickness of prepared films by spray coating. . . . .	51
Fig. 15 Current of as-synthesized ZnO/rGO with bending radius; (a) ZnO, (b) ZnO/rGO (10%), (c) ZnO/rGO (20%), and (d) ZnO/rGO (30%). . . . .	51
Fig. 16 Time-dependent absorption spectra of Methyl blue (MB) solution under visible light using (a) ZnO, (b) ZnO/rGO (10%), (c) ZnO/rGO (20%), and (d) ZnO/rGO (30%) as a photocatalyst. . . . .	52
Fig. 17 The photoluminescence spectra of pristine ZnO and as-synthesized ZnO/rGO. . . . .	52
Fig. 18 X-ray diffraction patterns of pristine ZnO, CeO <sub>2</sub> [156], and as-synthesized Ce/ZnO samples. . . . .	60
Fig. 19 Field-emission scanning electron microscopy (FE-SEM) images of (a) pristine ZnO, (b) 3% Ce/ZnO, (c) 5% Ce/ZnO, and (d) 7% Ce/ZnO samples. . . . .	61
Fig. 20 HR-TEM images and SAED patterns of (a,b) pristine ZnO and (c,d) 7% Ce/ZnO nanocomposites; (e) energy dispersive spectroscopy (EDS) mapping of 7% Ce/ZnO samples. . . . .	62



Fig. 21 X-ray photoelectron spectroscopy (XPS) spectra of pristine ZnO and 7% Ce/ZnO samples: (a) Survey spectrum and deconvoluted XPS spectrum of (b) Zn 2p, (c) O 1s, and (d) Ce 3d. . . . .	64
Fig. 22 UV–visible spectroscopy of the pristine ZnO and Ce/ZnO samples: (a) Absorption spectra and (b) optical band-gap energy. . . . .	65
Fig. 23 The photoluminescence spectra of the pristine ZnO and Ce/ZnO samples. . . . .	67
Fig. 24 Change in absorption spectra of the (a) pristine ZnO, (b) 3% Ce/ZnO, (c) 5% Ce/ZnO, and (d) 7% Ce/ZnO catalysts during photodegradation of methyl orange. . . . .	70
Fig. 25 (a) First- and (b) second-order kinetic adsorption curves of the pristine ZnO and Ce/ZnO catalysts during photodegradation of methyl orange. . . . .	71
Fig. 26 Electron trapping and charge transfer for methyl orange (MO) degradation using the Ce/ZnO catalysts. . . . .	73
Fig. 27 FE-SEM image and size distribution of pristine ZnO. . . . .	77
Fig. 28 The emission spectrum of fluorescent lamp (compact fluorescent lamp) and absorption spectrum of MO. . . . .	77
Fig. 29 FE-SEM and HR-TEM images of ZnO and functionalized ZnO samples. . . . .	84
Fig. 30 XRD patterns of ZnO and functionalized ZnO samples. . . . .	85
Fig. 31 FT-IR of ZnO and functionalized ZnO samples; (a) 400-4000 $\text{cm}^{-1}$ , (b) C-N stretching region: 1350-1400 $\text{cm}^{-1}$ , and (c) N-H bend vibrational region: 1500-2000 $\text{cm}^{-1}$ . . . . .	87
Fig. 32 XPS of ZnO and ZnO/An3 samples; (a) XPS Survey spectrum, (b) deconvoluted XPS N 1s and (c) XPS Zn 2p. . . . .	88

Fig. 33 UV-vis spectra of ZnO and functionalized ZnO samples; (inset) optical energy band gap. . . . .	89
Fig. 34 (a) Photodegradation percentage, and (b) kinetic adsorption curves during MO photodegradation of ZnO and functionalized ZnO samples. . . . .	91
Fig. 35 Change in absorption spectra of the (a) pristine ZnO, (b) ZnO/An1, (c) ZnO/An2, and (d) ZnO/An3 catalysts during photodegradation of MO. . . . .	94

## Abstract in English

In this dissertation, I have focused on ZnO surface modification to improve the photocatalytic degradation performance. The studies have been divided to three sections for different strategies to improve photocatalytic properties of ZnO including to nonmetal and metal doping as well as specific charge and polar molecule functionalization.

In first section, the research studies focused on nonmetal doping. Zinc oxide/reduced graphene oxide nanocomposites (ZnO/rGO) are synthesized via a simple one-pot solvothermal technique. The nanoparticle–nanorod tunability was achieved with the increase in GO additive, which was necessary to control the defect formation. The optimal defect in ZnO/rGO not only increased ZnO/rGO surface and carrier concentration, but also provided the alternative carrier pathway assisted with rGO sheet for electron–hole separation and prolonging carrier recombination. These properties are ideal for photodetection and photocatalytic applications. For photosensing properties, ZnO/rGO shows the improvement of photosensitivity compared with pristine ZnO from 1.51 (ZnO) to 3.94 (ZnO/rGO (20%)). Additionally, applying bending strain on ZnO/rGO enhances its photosensitivity even further, as high as 124% at  $r= 12.5$  mm, due to improved surface area and induced negative piezoelectric charge from piezoelectric effect. Moreover, the photocatalytic activity with methylene blue (MB) was studied. It was observed that the rate of MB degradation was higher in presence of ZnO/rGO than pristine ZnO. Therefore, ZnO/rGO became a promising material for different applications.

In second section, the research studies focused on metal doping. Cerium-oxide-nanoparticle-decorated zinc oxide was successfully prepared using a simple one-pot hydrothermal technique with different weight% Ce doping. It was found that an increase in Ce doping has an effect on the optical energy band-gap tunability. Ce dopant provides electron trapping on Ce/ZnO nanocomposites and also acts as a surface defect generator during hydrothermal processing. Additionally, a bi-metal oxide heterojunction forms, which acts as a charge separator to obstruct charge recombination and to increase the photodegradation performance. It was found that the methyl orange (MO) degradation performance improved with an increase in Ce doping. The decomposition of MO went from 69.42% (pristine ZnO) to 94.06% (7% Ce/ZnO) after 60 min under fluorescent lamp illumination.

In last section, the research studies focused on Specific charge and polar molecule functionalization. Functionalization of aniline molecules on zinc oxide (ZnO) nanoparticles is reported using a simple impregnation technique. As-prepared samples were systematically characterized based on morphology, surface and optical properties, and photocatalytic performance towards methyl orange (MO). Aniline functionalization increases the surface charge of the modified ZnO. Compared to pristine ZnO, the aniline-functionalized ZnO shows faster photodegradation of MO, degrading 98.29% of MO in 60 min. These results indicate that the improvement of photocatalytic degradation is ascribed to opposite charge-induced surface adsorption. Hence, aniline, as a positively charged molecule, is expected to increase the surface adsorption of MO (as an anionic dye) onto the ZnO nanoparticles, thereby increasing their photodegradation ability.

## Abstract in Korean (국문 요약)

본 학위논문의 연구주제는 광촉매 분해 성능을 향상시키기 위한 ZnO 표면 개질에 관한 것이다. 본 연구에서는 비금속 및 금속 도핑뿐만 아니라 특정 전하 및 극성 분자를 이용한 관능기화 등, ZnO의 광촉매 특성을 향상시키기 위한 3가지의 다른 전략을 나누어 정리하였다.

첫 번째 연구는 비금속 도핑에 초점을 맞췄다. Zinc oxide/Reduced graphene (ZnO/rGO)는 간단한 용매열합성법을 이용하여 합성하였다. 나노입자-나노로드 형상의 조절은 defect 형성을 제어하기 위해 필요한 Graphene oxide (GO) 첨가량을 통해 가능함을 관찰하였다. ZnO/rGO에서의 defect가 최적화되는 경우, ZnO/rGO 표면과 캐리어(carrier) 농도를 증가시켰을 뿐만 아니라 전자와 홀의 분리 및 전자와 홀의 재결합을 방지하고 캐리어 수명 향상을 위하여 rGO 시트를 보조하는 다른 캐리어 경로를 제공함을 관찰하였다. 광감지 특성의 경우 ZnO/rGO는 pristine ZnO 대비 광감도가 1.51 (ZnO)에서 3.94 (ZnO/rGO (20%))로 향상됐다. 또한 ZnO/rGO에 휘어지도록 힘을 가하면 표면적이 증가되고 압전 효과로 인해 음극 압전 전하가 유도되면서  $r = 12.5\text{mm}$ 에서 124%까지 광감도를 더욱 향상된다. Methylene blue(MB)에 대한 광촉매 활성도 관찰하였는데, pristine ZnO에 비해 ZnO/rGO는 MB 농도를 더욱 크게 감소시키는 것으로 관찰되었다. 따라서 ZnO/rGO는 다양하게 활용될 수 있는 유망한 재료로 보여진다.

두 번째, 연구는 금속 도핑에 초점을 맞췄다. Cerium oxide (Ce) 나노입자를 올린 산화아연은 서로 다른 무게 퍼센트의 세슘을 간단한 용매열합성법을 사용하여 합성하였다. Ce 도핑양의 증가는 광 에너지 band gap 조절(tunability)에 영향을 미치는 것으로 나타났다. 도핑한 세슘은 Ce/ZnO 나노 복합물에 전자 트래핑을 제공하며 수열처리 시 표면 defect을 발생시키는 역할도 하였다. 또한,

두 종류의 금속산화물을 heterojunction을 형성했을 때, 캐리어 재결합을 방해하고 광분해 성능을 높이기 위한 전하 분리기의 역할을 수행하였다. 세습 도핑량이 증가할수록 Methyl orange (MO) 광분해 성능이 향상된 것으로 나타났다. 형광 등 램프 하에서 60분 후에 MO의 분해는 69.42% (pristine ZnO)에서 94.06% (7% Ce/ZnO)로 증가했다.

마지막으로 특정 전하와 극성을 지닌 분자를 활용한 기능화 (functionalization)에 대한 연구를 수행하였다. ZnO 나노입자에 아닐린 분자를 이용한 기능화는 간단히 impregnation 기법을 사용하였다. 제조한 생성물에 대해 표면과 형태 등 외적인 특성과 광학적 특성, Methyl orange (MO)에 대한 광촉매 성능을 체계적으로 연구하였으며, 아닐린 기능화는 수정된 ZnO의 표면 전하를 증가시키는 것으로 나타났다. Pristine ZnO에 비해 아닐린으로 기능화된 ZnO는 MO의 광분해 속도가 빨라져 MO의 98.29%가 60분 만에 저하되는 것으로 관찰되었다. 이러한 결과는 광촉매 분해 능력의 향상이 상반되는 전하가 유도한 표면 흡착에 의해 결정된다는 것을 나타낸다. 따라서 아닐린은 양전하 분자로서 ZnO 나노입자에 대한 음이온염료 (Anionic dye)로서의 MO의 표면 흡착력을 증가시켜 광분해 능력을 증가시킨 것으로 판단된다.

# 1 Introduction

Water is presumably the most important natural resource second only to air. Food may attain the third position but for production of food, water is indispensable. Water is required for majority of the biochemical transformations that take place inside the bodies of living being from bacteria to the most advanced organisms. In addition to that, most of the life processes happen in the world are being occupied by water. Industrial development and increasing population growth have contributed leading to high energy supply demand and an increase in environmental pollution such as air and water pollution. Every year, industrial plants dump a several million tons of heavy metals and their related by-products produced into natural water resources without proper processing and treatment resulting to crisis water pollution.

There are numerous sources of water pollution, but the ones that can be thought to be representative and major players in this process are industrial wastes, unregulated domestic wastes, marine dumping of the wastes produced by human activity, use of pesticides and harmful chemicals in agriculture, untreated wastes, and so on. This pollute our surrounding terrestrial lands and water bodies.

The wide spectrum of synthetic organic dye pollutants is annually produced worldwide and is released to the wastewater stream. Therefore, the removal of organic pollutants is of particular importance due to their harmful effect on the environment. Wastewater treatment and reuse is an important issue and scientists are looking for inexpensive and suitable technologies. Various physical, chemical and biological treatments have been widely used to convert and remove organic pollutants such as screening filtration, centrifugal separation, distillation,

precipitation, reverse osmosis, electrolysis, micro-ultra filtration, and so on.

Advanced oxidation processes (AOPs) have gained growing attention as an alternative to traditional treatment processes for organic pollutant removal. Advanced oxidation processes are defined as processes which rely on in situ generation of highly oxidizing radicals involving mainly hydroxyl radicals ( $\text{OH}^\bullet$ ) for the degradation of toxic organic pollutants into non-hazardous compounds. Especially, AOPs techniques by using semiconductor-mediated heterogeneous photocatalysis is a promising technique, which is valuable for environmental and energy applications. Owing to its advantages such as low cost and non-toxic which only use sunlight to generate oxidizing radicals. In addition, this technique can effectively degrade/ decompose of organic pollutants. Therefore, semiconductor-mediated heterogeneous photocatalyst has become an attractive topic in this decade.

Some notable semiconductors applied as photocatalysts are included  $\text{TiO}_2$ ,  $\text{ZnO}$ ,  $\text{CdS}$ ,  $\text{WO}_3$ ,  $\text{SnO}_2$ ,  $\text{ZnS}$ ,  $\text{CdTe}$ ,  $\alpha\text{-Fe}_2\text{O}_3$ ,  $\text{AgNbO}_3$  and  $\text{SrTiO}_3$ . Among the above materials,  $\text{ZnO}$  is believed to have higher efficiency in the photocatalytic performance than other materials, in many cases due to its higher quantum efficiency. Zinc oxide ( $\text{ZnO}$ ) is a promising n-type semiconductor material that is used in a wide range of applications, such as gas detection [1]–[4], dye-sensitized solar cells [5]–[7], antibacterial surface coatings [8], light-emitting diodes (LEDs) [9], [10], nanopower generators [11], ultraviolet (UV) detection [12]–[15], and photocatalytic applications [16]–[18].  $\text{ZnO}$  nanostructures have a direct wide band gap (3.37 eV) [19], chemical stability [20], optical [21], piezoelectric [22]–[24], and electrical [25] properties. Additionally,  $\text{ZnO}$  possesses piezoelectric properties and self-carrier generation



when tensile strain force is applied or substrates are bent [26]. ZnO based on UV detection is governed by photogenerated electrons that trap oxygen molecules at the surface of ZnO and change sensor resistance. In other way, ZnO as a photocatalyst, the photogenerated electron-hole pairs upon excitation may react with oxygen and water molecules resulting in free radicals that can degrade organic and inorganic compounds in aqueous medium. However, the performance of ZnO-based UV detection and photocatalytic activities faces some drawbacks in surface morphology, charge transportation, and recombination. Beside the above-mentioned drawbacks, when used as a photocatalyst, ZnO has very limited capability for visible light adsorption and can generate electron-hole pairs only in UV light, which contributes only 2–3% to total sunlight. Modulation of ZnO surface modification is one of the main strategies to improve the photocatalytic activity of dyes degradation performance. Herein, I have focused on ZnO surface modification technique to improve the photocatalytic degradation performance.

The chapter 2 describe the introduction of photocatalytic degradation of organic pollutants techniques and ZnO as main materials in this research. The detailed literature review of photocatalyst based metal-oxide nanostructures, ZnO photocatalyst, limitation in photocatalytic application of ZnO, and how to improve ZnO photocatalytic performance was also provided in this dissertation.

The chapter 3 of this dissertation described the effect of GO additive in ZnO/rGO nanocomposites with enhanced photosensitivity and photocatalytic activity. This report represents the surface modification of ZnO by using nonmetal element doping approach.

The chapter 4 of this dissertation reports cerium-oxide-nanoparticles decorated zinc oxide with enhanced photocatalytic degradation of methyl orange. This research represents the surface modification of ZnO by using metal/metal-oxide element doping approach.

The chapter 5 of this dissertation details on an improvement of photodegradation performance of ZnO nanoparticles by surface charge modification using aniline. This research represents the surface modification of ZnO by using polar molecule functionalization approach.

## 2 Literature reviews

### 2.1 Zinc oxide (ZnO)

ZnO is a wide band gap (3.37 eV) metal oxide semiconductor. It is amorphous in color of white or light yellow. But it is generally known a white powder. Due o its excellent optoelectronic and piezoelectric properties, biocompatibilities, environmentally friendly nature, and thermal stability, ZnO nanostructures are the most promising candidate for electronic and optoelectronic applications including light emitting diodes (LEDs), actuators, sensors, field-emission devices, solar cell, spintronic piezoelectric devices as well as photocatalyst.

ZnO consists of three different crystal structures, i.e hexagonal wurtzite, cubic zin-blende, and the infrequently observed cubic rock-salt. However, at general atmosphere condition, the thermodynamically stable in hexagonal wurtzite phase due to the effect and the bonding class is precisely at the border between covalent and ionic. The ZnO hexagonal wurtzite crystal structure belongs to the  $P6_3mc$  class in Hamitonian-Mauguin notation. The ZnO primitive unit cell composes of zinc ion surrounding with four oxygen ions in tetrahedral coordination and vice versa. The noncentrosymmetric crystallographic polarity, and is also a key factor in crystal growth and defect generation. The wurtzite structure has a hexagonal unit cell with two parameters,  $a$  (ranges from 3.2475 to 3.2501 angstrom) and  $c$  ranges from 5.2042 to 5.2075 angstrom, in the ration of  $c/a = 1.633$ . ZnO is a relatively soft material with approximate hardness of 4.5, having high heat conductivity and heat capacity, poorly thermal expansion, and high melting temperature. It is beneficial for ceramics, Among the tetrahedrally

bonded semiconductors, it has been stated that ZnO has high piezoelectric tensor. This property can be applied for many piezoelectrical technologies, which require a large electromechanical coupling. The general properties of ZnO are shown in Table 1.

**Table 1:** General properties of ZnO.

<b>Properties</b>	<b>Values</b>
Molecular weight	81.37
Average atomic weight	40.96
Average atomic number	19
Enthalpy of formation (298K)(kJ/mol)	-350.5
Coefficient of thermal expansion: Along c-axis (1/K)	$2.9 \times 10^{-6}$
Coefficient of thermal expansion: Across c-axis (1/K)	$4.8 \times 10^{-6}$
Density (g/m <sup>3</sup> )	5.6803
Melting point (K)	2,248

## 2.2 ZnO as a photocatalyst

ZnO is a type of semiconductor having a broad direct band gap width (3.37 eV), large excitation binding energy (60 meV) and deep violet/borderline ultraviolet (UV) absorption at room temperature [27]. It is an excellent semiconductor oxide that possesses favorable excellent electrical, mechanical and optical properties [28], similar to TiO<sub>2</sub>. In addition, ZnO not only has antifouling and antibacterial properties, but also good photocatalytic activity [29]. Furthermore, as reported by Liang et al. [30], the production cost of ZnO is up to 75% lower than that of TiO<sub>2</sub> and Al<sub>2</sub>O<sub>3</sub> nanoparticles. Due to the advantages of ZnO over TiO<sub>2</sub>, ZnO has been suggested to be used in heterogeneous photocatalysis. According to Herrmann et al. [31], the heterogeneous photocatalytic oxidation steps can be explained as shown in Fig. 1

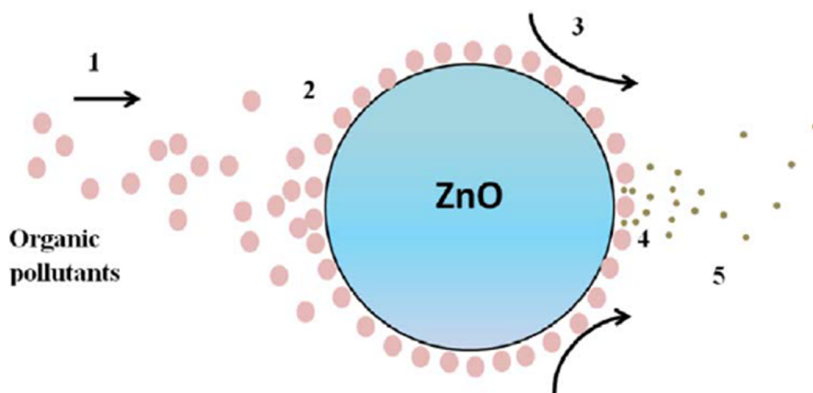
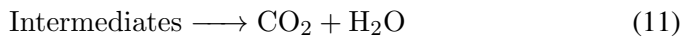
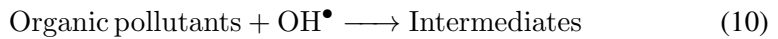
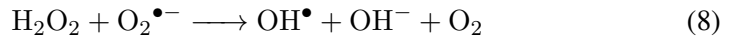
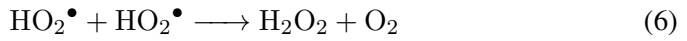
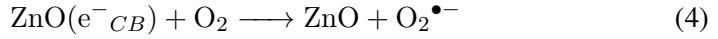
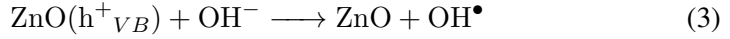
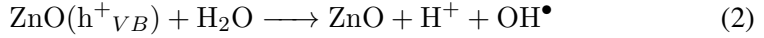
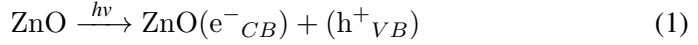


**Fig. 1:** Heterogeneous photocatalytic oxidation step [31].

1. Organic pollutants diffuse from the liquid phase to the surface of ZnO.
2. Adsorption of the organic pollutants on the surface of ZnO.
3. Oxidation and reduction reactions in the adsorbed phase.
4. Desorption of the products.
5. Removal of the products from the interface region.

When ZnO is photo-induced by solar light with photonic energy ( $h\nu$ ) equal to or greater than the excitation energy ( $E_g$ ),  $e^-$  from the filled valence band (VB) are promoted to an empty conduction band (CB). This photo-induced process produces electron-hole ( $e^-/h^+$ ) pairs as shown in Eq. (1). The electron-hole pairs can migrate to the ZnO surface and be involved in redox reactions as shown in Eqs. (2)–(4), wherein the  $h^+$  reacts with water and hydroxide ions to produce hydroxyl radicals while  $e^-$  reacts with oxygen to produce superoxide radical anions then hydrogen peroxide (Eq. (5)). Hydrogen

peroxide will then react with superoxide radicals to form hydroxyl radicals (Eqs. (7)–(9)). Then, the resulting hydroxyl radicals, which are powerful oxidizing agents, will attack the pollutants adsorbed on the surface of ZnO to rapidly produce intermediate compounds. Intermediates will eventually be converted to green compounds such as CO<sub>2</sub>, H<sub>2</sub>O and mineral acids as shown in Eq. (11). Fig. 2 illustrates the redox reaction occurring during photocatalysis. Hence, the mechanism of photodegradation of organic compounds in the presence of solar radiation via redox reaction can be summarized as follows [32], [33]:



As mentioned earlier, ZnO has been shown that to exhibit higher absorption efficiency across a larger fraction of solar spectrum compared to TiO<sub>2</sub>. The photoactivity of a catalyst is governed by its ability to create photogenerated electron-hole pairs. The major constraint of ZnO as a photocatalyst, however, is the rapid recombination rate of photogenerated electron-hole pairs, which perturbs the photodegradation reaction. Additionally, it has also been noted that the solar energy conversion performance of ZnO is affected by its optical absorption ability, which has been associated with its large band gap energy. Therefore, intense efforts have been made to improve the optical properties of ZnO by minimizing the band gap energy and inhibiting the recombination of photogenerated electron-hole pairs.

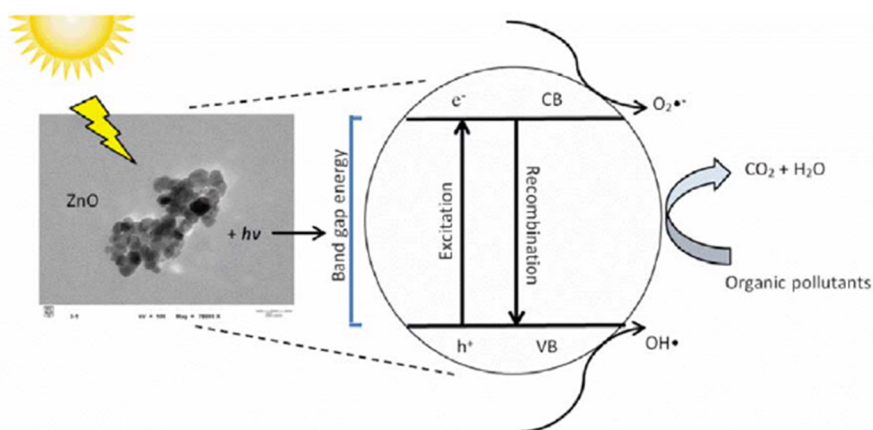


**Fig. 2:** Degradation of organic pollutant by ZnO under sunlight [31].

### 2.3 Modification strategies for photocatalytic performance improvement

In principle, photocatalytic activity will be enhanced if the absorption of light is higher or if the recombination losses for photogenerated charge carriers are

lower. Different strategies for enhancing the photocatalytic activity of ZnO under visible/solar illumination have been reported. An attractive strategy for enhancing the activity under visible/solar illumination is surface modification including to defect engineering (oxygen sub-stoichiometry), doping or functionalization by using different elements (metals and non-metals) and functional group, spatial structuring, and morphology optimization for enhancing the proportion of active facets.

### **2.3.1 Metal/nonmetal doping**

ZnO has a tetrahedral bonding configuration which possesses large ionicity at the borderline between that of covalent and ionic semiconductors resulting to show a wide band gap energy characteristic. ZnO is normally an intrinsic n-type metal oxide semiconductor consisting of a native disorder such as an oxygen vacancy, zinc interstitials, and zinc vacancies. The presence of intrinsic defect in ZnO directly influence to its electrical and optical properties. Photocatalytic performance is mainly depended on energy band gap and hydroxyl radicals. The main obstacle for ZnO semiconductors as photocatalysts is their fast charge recombination. Doping technique has been widely used to modify the ZnO physical and chemical properties. By this technique, an incorporating impurity such as metals or non-metals were construct in/on ZnO crystal which can tune valence band energy of ZnO upward and narrow the bandgap energy to the UV-visible region [34].

Many studies have reported that non-metal additive such as nitrogen, carbon and fluorine can effectively tune the bandgap of ZnO by substituting oxygen



vacancy position owing their extremely small sizes and introducing greater oxygen vacancy defects on ZnO surface. Carbon is a prominent candidate for a non-metal dopant for in semiconductors owing its high mechanical strength, good chemical resistance and special electronic properties [35]. In addition, doping also can contribute to a greater production of OH• radicals, thus, lead to a higher degradation efficiency of organic pollutants [36]. This was explained by the facts that the dopants can act as electron scavengers and prevent the recombination of electron-hole pairs, thus, free the positive hole (H<sup>+</sup>) of photocatalyst (which is significant for the formation of OH• radicals)

Metal additives like transition metals, rare earth metals, noble metals and other metals have shown advantages in tailoring the ZnO morphology. Metal doped ZnO can improve the photoactivity of catalysts by enhancing the trapping site of the photo-induced charge carriers results to hinder the charge recombination rate of photogenerated electron-hole pairs [37]. To narrow the energy band gap of ZnO photocatalysts, metal additives such as Ce, Nd, Cu and Al have been studied in removal of dye degradation. Yun et al. [38] have shown that higher loads of organic compounds could be adsorbed on Al-doped ZnO compared to pure ZnO based on the high light harvesting efficiency. Zhu et al. [39] has reported that the incorporation of metal ions such as Fe<sup>3+</sup>, can contribute to more oxygen defects on ZnO along with an increase in the charge density of ZnO, which subsequently can show photocatalytic degradation performance of modified ZnO photocatalyst. Wang et al. [40] has endeavored to demonstrate that Ag-doped ZnO has a greater specific surface area of nanoparticles and greater lattice deficiency. Min et al. [41] synthesized ZnO nanoparticles with copper doping by using a sol-gel technique for photocatalytic

applications, and these showed higher methyl blue degradation (88%, 6 h) compared with un-doped ZnO Metal doped ZnO, prepared using Mn and Co through co-precipitation method, was previously used in methyl orange degradation via photocatalytic experiments [42]. Degradation and adsorption of methyl orange onto the heterogenous catalysts were shown to be greatly affected by the solution pH. According to that work, 12 at% was the optimal dopant concentration to be used in which the best degradation efficiency was recorded by Mn-doped ZnO catalyst at pH 4 or acidic condition. Summary of modified ZnO synthesis by using various dopants and fabrication techniques was shown in Table 2 and 3.

**Table 2:** Overview of various dopants in the ZnO nanostructures with their synthesis techniques, operated photocatalytic conditions and photocatalytic performances (1).

Dopant	Synthesis technique	Pollutant (type, concentration)	Light source	Photocatalytic performance	Ref
S	Hydrothermal (90°C, 3 h)	MB, 0.01 nM	100W halogen-tungsten lamp	93.9% in 240 min	[43]
	Co-precipitation process	BR2, $1.43 \times 10^{-5}$ mol L <sup>-1</sup>	300W ozone-free xenon-arc lamp	94% in 180 min	[44]
		4-CC, $8 \times 10^{-5}$ mol L <sup>-1</sup>		70% in 180 min	
N	Sol-gel (90°C, 2 h)	Congo red, 5 ppm	30W UV-C (253.7 nm)	99% in 30 min	[45]
	Sol-gel (RT, 24 h)	Mixture of 2, 4-D (20 ppm) and picloram (5 ppm)	25W Halogen-Tungsten lamp	100% in 210 min	[46]
	Microemulsion method	MG, 10 ppm	65W Compact fluorescent lamp	100% in 90 min	[47]
	Thermal oxidation (600°C, 4 h)	BPA, - ppm	350W Xenon lamp	94% in 4 h	[48]
Co	Spray pyrolysis	Toluene, - ppm	Solar simulator	68% in 250 min	[49]
	Wet chemical method (95°C, 3 h)	MB, 10 $\mu$ M	Solar simulator	100%, 8 min	[50]
Ni	Co-precipitation method	MB, 5 ppm	300 W mercury lamp and 500W Xenon lamp	83% in 150 min	[51]
Al	Hydrothermal (180°C, 12 h)	MB, - ppm	300W Xenon lamp	70% in 75 min	[52]
Al/Fe	Hydrothermal (180°C, 12 h)	MB, - ppm	300W Xenon lamp	90% in 75 min	[52]
Ag	Film deposition	MB, 10 ppm	UV-C lamp	100% in 4 h	[53]
Cu	Sol-gel	MO, 20 ppm	25W UV lamp	88% in 4 h	[41]

**Table 3:** Overview of various dopants in the ZnO nanostructures with their synthesis techniques, operated photocatalytic conditions and photocatalytic performances (2).

Dopant	Synthesis technique	Pollutant (type, concentration)	Light source	Photocatalytic performance	Ref
Er/Yb	Combustion method	MO, 15 ppm	200W Mercury lamp (420 nm)	95% in 90 min	[54]
Eu	Hydrolysis	MB, 0.0267 mM	20W Halogen lamp	99.3% in 80 min	[55]
	Precipitation method	MB, 10 ppm	40W UV-C lamp (254 nm)	96.5% in 180 min	[56]
Nd	Sol-gel	MB, - ppm	125W Mercury lamp	100% in 25 min	[57]
	Sonochemically assisted chemical co-precipitation method	R6G, $10^{-5}$ M	125W (Philips) UV lamp	97.39% in 180 min	[58]
La	Gel combustion method	MO, 10 ppm	20W Compact Lamp (Philips)	85.86% in 150 min	[59]
	Microwave assisted sol-gel	MB, 20 ppm	Heber multi-lamp photo reactor with 8 lamps	92% in 60 min	[60]
	Solvothermal (150°C, 20 h)	RhB, $10^{-5}$ M	15W UV lamp (365 nm)	100% in 200 min	[61]
Ce	Wet chemical method	RhB, 25 ppm	15W Xenon lamp	85.1% in 125 min	[62]
	Thermal evaporation (350°C, 3 h)	MO, - ppm MB, - ppm	250W Projection lamp	95.9% in 150 min 97.4% in 150 min	[63]
	Mechanical milling	MB, $3 \times 10^{-5}$ mol L <sup>-1</sup>	400W Sodium lamp	78.1% in 180 min	[64]

### 2.3.2 ZnO coupling with carbonaceous groups

Heterojunction photocatalysts are also an effective aspect to improve the photocatalytic degradation performance of ZnO. Chang et al. [65] reported that the heterostructure of photocatalysts, combined with the merits of different compounds including light absorption, charge separation, and charge transfer between different kinds of semiconductors can cause rapid photogenerated charge separation. Carbon nanostructures play pivotal roles in the development of nanocomposites. Recently, it has been reported that the heterojunction of ZnO with carbon nanotubes can enhance the performance of nanocomposites by acting as electron scavenging agents.

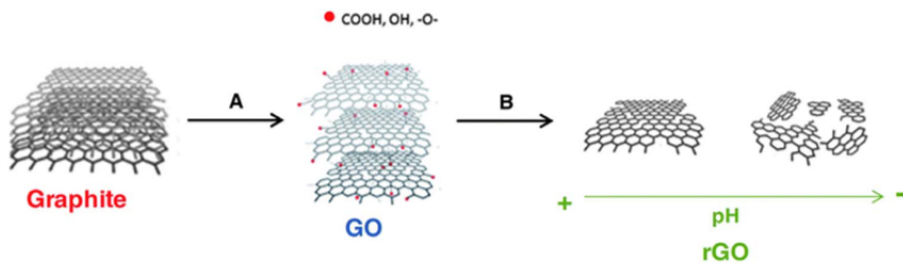


**Fig. 3:** Synthesis of reduced graphene oxide (rGO): (A) oxidation of graphite to graphene oxide, (B) reduction of graphene oxide to reduced graphene oxide [66].

Graphene has been of considerable interest in many applications such as photocatalysis and gas sensing due to its excellent conductivity, high surface area and electron mobility [67]. Graphene is a  $sp^2$  carbon-based nanomaterial in a single atom thick sheet which is arranged in a hexagonal honeycomb lattice distribution. Single-layer graphene exhibits rather high specific surface area, Young's modulus, thermal conductivity and mobility charge carriers [68]–[71]. These optimal properties are mainly attributed to the presence of functional

groups such as hydroxyl, epoxide, carboxylic and carbonyl groups. As can be seen in Fig. 3, the interplanar spacing between graphite is increased through oxidation processes using Hummer's method. Oxidation into graphene oxide (GO) perturbs the electrical conductivity, creating an excellent electrical insulator [72].

GO can be reduced into reduced graphene oxide (rGO) by manipulating the pH of GO in solution and followed by a thermal treatment. Recent works have revealed that the heterostructure of ZnO/GO has greater carrier transport efficiency due to the graphene encapsulation, specific surface area and electrical transport properties [70], [73]. A sol-gel method has been used by Fu et al. [74] to prepare ZnO decorated graphene and they found that the adsorption of dyes during the photocatalytic process was increased along with higher loading of graphene implying that graphene can also be used as adsorbent in water treatment. Enhancement in adsorption of organic pollutants probably is due to  $\pi$ - $\pi$  conjugation between organic pollutants and the  $sp^2$  regions of rGO according to a report work [75]. Further studies on graphene adsorption behavior under different conditions are needed to achieve an optimum removal efficiency. ZnO coupled with rGO should improve the photocatalytic degradation of organic pollutants. However, rGO loading exceeding the optimum dosage will lead to a lower degradation efficiency, which could be explained by high photo-absorbing and scattering [76]. Cysteine capped ZnO/graphene oxide composite was prepared using co-precipitation method, showing the degradation efficiency at about 98.13% within 45 min. Summary of modified ZnO synthesis by using various carbonaceous groups and fabrication techniques was shown in Table 4.

**Table 4:** Overview of various carbonaceous group in the ZnO nanostructures with their synthesis techniques, operated photocatalytic conditions and photocatalytic performances.

<b>Dopant</b>	<b>Synthesis technique</b>	<b>Pollutant (type, concentration)</b>	<b>Light source</b>	<b>Photocatalytic performance</b>	<b>Photocatalytic reaction rate</b>	<b>Ref</b>
CNT-rGO	Microwave reaction (100°C, 30 min)	MB, 5 ppm	500W Hg lamp (365 nm)	96% in 260 min	0.011 min <sup>-1</sup>	[16]
Gelatin-rGO	Hydrothermal (180°C, 5 h)	MB, 10 <sup>-5</sup> mol L <sup>-1</sup>	300W Mercury lamp	99% in 60 min	0.077 min <sup>-1</sup>	[77]
PANI-rGO	Chemical oxidation polymerization	MO, 10 ppm Phenol, 10 ppm	500W Mercury lamp	99% in 60 min 98.6% in 180 min	-	[78]
g-C <sub>3</sub> N <sub>4</sub>	Thermal oxidation	MB, 10 ppm	100W Visible lamp	99% in 180 min	0.034 min <sup>-1</sup>	[17]
rGO	Sol-gel (90°C, 5 h)	MO, 10 ppm	100W Mercury lamp	83% in 120 min	-	[18]
	Microwave reaction	MB, 5 ppm	Natural sunlight	94.8% in 120 min	-	[79]
	Hydrothermal (180°C, 16 h)	SO, 10 <sup>-5</sup>	100W UV lamp	99% in 25 min	-	[80]

### 2.3.3 Specific charge and polar molecule functionalization

Owing to the existence of Zn–O–Zn bonds in ZnO nanoparticles, agglomeration occurs readily, thus strongly limiting ZnO nanoparticle applications [81]. Surface modification may be the best approach for ensuring better dispersion by preventing the agglomeration of ZnO. In addition, surface modification has also been used to tune the ultraviolet and visible light photoluminescence, as the chemical and physical properties of ZnO nanoparticles can be modified via chemical surface modification through chemical treatment [82], coating [81], grafting polymerization [83], ligand exchange [84] and self-assembly techniques [85]. Chemical treatment is an approach that utilizes coupling agents (e.g. trimethoxyvinyl silane and oleic acid) to modify the surface of nanoparticles. Modified ZnO fabricated by Hong et al. [86] through grafting polymerization has shown better dispersion in organic matrix compared to bare ZnO nanoparticles.

Ligand molecules (i.e. polymeric ligands and monomeric ligands) are also common capping agents used in the coating method to prevent the aggregation and control the growth of nanoparticles. The ligand layer acts as an insulating barrier and blocks the charge transport between neighboring nanoparticles before recombination can occur [87]. Recently, stabilization of ZnO nanoparticles through coating method using polymeric ligands has proved to be better than monomeric ligands. This is due to the presence of steric and electrostatic forces that were used to stabilize the ZnO in the polymeric ligands but in the latter, only electrostatic repulsive forces can contribute to the ZnO stabilization [88]. Coating method manages to improve the dispersion of nanoparticles in the matrix, however, this method may impede the photocatalysis at the same time [81]. In



order to simultaneously stabilize and enhance the performance of nanoparticles, ligand exchange – (a method where the attached ligand molecules on the surface of photocatalyst can be exchanged with other ligand molecules) could be a more preferable approach. In this context, Kango et al. [89] has reported that ligand molecules should be exchanged with more suitable ligands in order to enhance the transfer of electrons by lowering the separation effects

In contrast, flower-like ZnO structures were successfully synthesized by controlling the molar ratio of  $\text{Zn}^{2+}$  and  $\text{OH}^-$  ions. Previous research has revealed that excess OH may lead to the formation of the  $[\text{Zn}(\text{OH})_4]^{2-}$  complex. Subsequent dehydration of the  $[\text{Zn}(\text{OH})_4]^{2-}$  complex favored formation of nanosheet array from particles. Flowerlike ZnO structures then form due to the tendency of nanosheets to minimize their surface energy [90]. Poly(vinyl pyrrolidone) was previously used as an intermediate to anchor ZnO on solvent exfoliated graphene [91]. Poly(vinyl pyrrolidone) was reported to decrease the surface free energy through its attachment on the ZnO surface thus lead to slow growth of the facets and provided good dispersion of the nanoparticles. Photocatalytic activity of produced photocatalyst in the degradation of Reactive Black 5 was 97% at a rate constant of  $0.0199 \text{ min}^{-1}$ .

## **2.4 Research objective**

The overall goal of the research is to improve the photocatalytic dye degradation performance of surface modified zinc oxide (ZnO) by using different strategies. The research is focused on the surface modification of ZnO and consisted of three parts following by

- Surface modification using nonmetal doping
- Surface modification using metal doping
- Surface modification using specific charge and polar molecule functionalization.

Each types of surface modification strategies exhibit some advantages to improve the photocatalytic dye degradation performance of ZnO such as surface adsorption and charge separation improvement.

### **3 The Effect of GO Additive in Zinc Oxide/ Reduced Graphene Oxide Nanocomposites with Enhanced Photosensitivity and Photocatalytic Activity**

#### **3.1 Introduction**

In this chapter, we present the surface modification of ZnO by using nonmetal doping. Pati et al. found that the point defect concentration and optical/gas sensitivity of ZnO is due to the vacant lattices acting as active sites for oxygen trapping [92]. Zhang et al. reported that the existence of disorder and surface defects in ZnO crystals could improve the separation of photogenerated electron–hole pairs, preventing recombination and enhancing photocatalytic activity [93]. With the increase in lattice defects, the trapping of oxygen on the surface will increase, resulting in an improvement in UV sensing properties and prolonging the photocatalytic activity. In the case of ZnO nanoparticles, the potential barrier at the interface between the ZnO–ZnO grain boundaries results in slow charge transfer across grain boundaries and fast recombination. Some researchers reported that enhanced charge separation can provide a progression in interfacial charge transfer for dyes adsorption and photocatalytic degradation improvement [94], [95]. To improve UV photosensitivity and photocatalytic activity, this carrier concentration, carrier pathway, and charge recombination should be modified [96].

In recent years, several efforts have been made to improve carrier concentration, to provide alternative carrier pathway and reduce charge recombination by tuning ZnO morphology, surface defect improvement

[96]–[100], and combining ZnO with other functional materials, such as carbon-based graphene oxide (GO) [13] and reduced graphene oxide (rGO) [101], [102]. GO, rGO, and graphene consist of  $sp^2$  hybridized carbon atoms arranged in two-dimensional honeycomb lattices. For UV detector applications, the interaction of ZnO and rGO could enhance UV sensing properties, in terms of inhibiting the recombination of electron–hole pairs and an increase in the photocurrent [103]. In addition to a capacity for photogenerated electron transportation from band gap excitation of semiconductors upon UV illumination and flexible mechanical properties that would support a self-carrier generator when bending strain is applied [104], applying tensile strain to ZnO/rGO hybrid nanostructures may improve photosensitivity in terms of increasing carrier density and carrier transfer. With regard to metal oxide based on photocatalytic activities, Zhang et. al. reported that graphene additive can improve photocatalytic activity by prolonging photogenerated electrons-hole pairs in  $TiO_2$ , which efficiently suppresses the recombination of the photogenerated electron–hole pairs in  $TiO_2$  [105]. Pronay et al. reported that rGO laminated  $TiO_2$ -B NW nanocomposites shows an excellent visible light dye degradation with superior degradation rate. This is due to defect creation and the narrowing of energy band gap, together with increasing adsorption by  $\pi$ -interaction between GO and dye molecules [106].

Herein, we have demonstrated a simple one-pot solvothermal technique to prepare ZnO/rGO nanocomposites with varying the GO content. Specifically, the amount of GO content was varied to control the dimensionality of ZnO nanostructures and surface defects, which play important roles in photosensitivity and photocatalytic activity. The effects of tuned morphology on

structural components, surface morphology, surface defects, and optical properties were also studied. As-synthesized ZnO/rGO was employed to evaluate UV photosensitivity assisted with applied bending strain and visible light photocatalytic activity of methylene blue (MB) degradation.

## **3.2 Experimental details**

### **3.2.1 Materials**

Analytical-grade zinc acetate dihydrate ( $\text{Zn}(\text{CH}_3\text{COO})_2 \cdot \text{H}_2\text{O}$ , Samchun Pure Chemicals, Pyeongtaek, Korea), sodium hydroxide (NaOH, Samchun Pure Chemicals, Pyeongtaek, Korea), and commercial graphene oxide (GO, GO-V20-100, Standard Graphene, Ulsan, Korea) were procured and used without further purification. Deionized water (DI) was used to prepare solutions and wash all samples.

### **3.2.2 Preparation of ZnO/rGO nanocomposites**

ZnO/rGO was prepared by a solvothermal technique as shown in Fig. 4(a). First, 0.04 M of zinc acetate dihydrate was dissolved in 80 mL of DI under continuous stirring at room temperature for 30 min. to study the effects of GO additive, a precalculated amount of dispersed GO in DI (5 mg/mL) was prepared separately under ultrasonication, corresponding to 10, 20, and 30 wt% of GO. Then, the prepared GO solution was dropped into a zinc acetate dihydrate solution under continuous stirring for 30 min. After that, 1 g of NaOH in 50 mL of DI was added dropwise to the mixed solution until a pH of 10 was reached. Finally, the mixed

solution was transferred to a Teflon-lined stainless steel autoclave under 150 °C for 6 h. The product was collected by filtration and washed by DI several times and dried at 70 °C for 6 h.

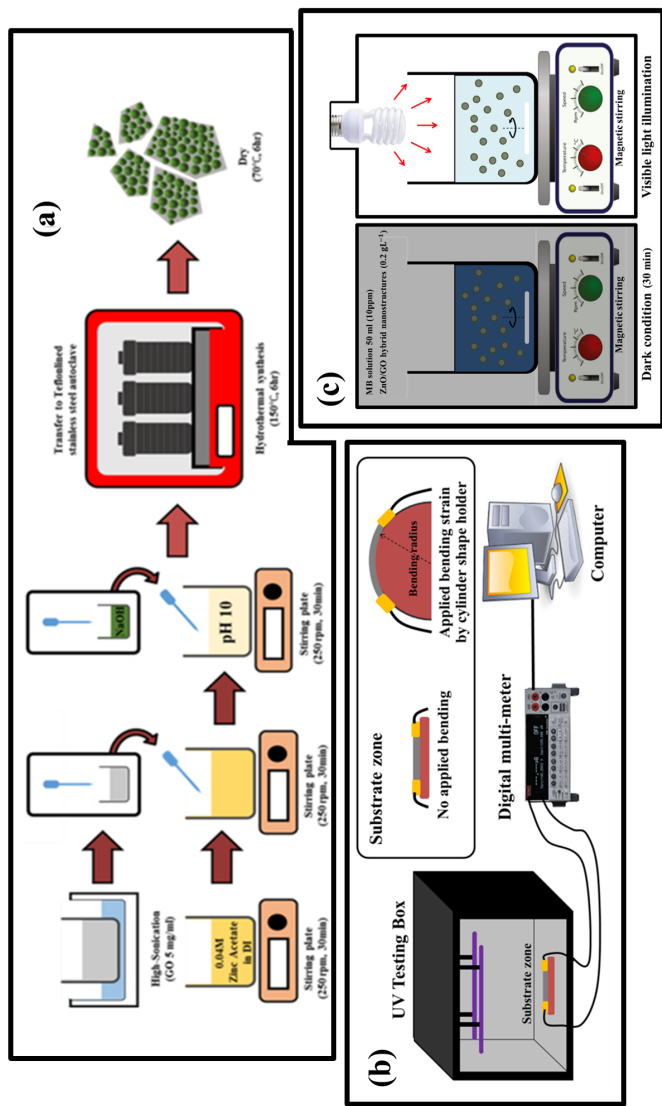


**Fig. 4:** (a) The preparation process of ZnO/rGO nanocomposites, (b) UV sensing measurement, and (c) photocatalytic experiment.

### **3.2.3 Characterization of ZnO/rGO nanocomposites**

Field-emission scanning electron microscopy (FE-SEM, JSM-600F, JEOL-JSM-7600F, Tokyo, Japan) and X-ray diffraction (XRD, Rigaku D/MAZX 2500V/PC model, Tokyo, Japan) were used to characterize the surface morphology and crystalline structure of ZnO/rGO. Fourier transform infrared spectroscopy (FT-IR, Thermo Electron Co., Waltham, MA, USA) and Raman spectroscopy (RS, Thermo Fisher Scientific, Waltham, MA, USA) were utilized at room temperature to investigate the functional groups and surface components of ZnO/rGO. Optical studies were considered the absorption spectra from 200 to 800 nm using an ultraviolet-visible spectrometer (UV-Vis, Spectramax Plus 384, Molecular Devices Co., San Jose, CA, USA). The surface properties and oxidation state of samples were investigated by X-ray photoelectron spectroscopy (XPS, K-alpha; Thermo Fisher Scientific Co., Waltham, MA, USA).

### **3.2.4 UV sensing measurement**

To study UV sensing properties based on ZnO/rGO, an electrode was prepared on a transparent film (thickness: 100 m). First, a transparent film substrate was cleaned in ethanol and DI and dried with a nitrogen gun. A UV sensor device based on ZnO/rGO was simply fabricated as a resistor in the electronic circuit. To make the sensing film, the as-synthesized ZnO/rGO powder was dissolved in DI (0.5 mg/mL) under ultrasonication. The mixed solution was then sprayed on the transparent film substrate and dried for 30 min at 60 °C. The spray-coating step was repeated three times to ensure full coverage and film uniformity. The



thickness of prepared film was shown in Fig. 14. Finally, a silver paste was applied to both sides of the sensor device and kept in an oven for 6 h at 60 °C. UV sensing properties based on ZnO/rGO were examined with a Blacklight blue lamp (EL20W BLB; 352 nm and 368 nm) with fixed intensity of 0.62 mW/cm<sup>2</sup> at room temperature. As shown in Fig. 4(b), the as-prepared UV sensor sample was tested in UV testing box, with and without bending strain. To study bending strain effects, the prepared samples were placed on cylinders holders with radii of 12.5, 10, and 7.5 mm and tested in on/off UV illumination states. The UV sensing system was controlled by KickStart software (Tektronix Company, Beaverton, OR, USA) and Keithley 2400 Source Meter.

### **3.2.5 Evaluation of photocatalytic degradation**

The photocatalytic activities of the samples were evaluated by degradation of MB as illustrated in Fig. 4(c). Prior to assessing the photocatalytic degradation activities, 10 mg of as-synthesized ZnO/rGO powder was added to an aqueous solution of MB (50 mL, 10 mg/L). The suspension was stirred for 30 min in the dark at 250 rpm to reach adsorption/desorption equilibrium. The prepared solutions were then illuminated by a 20W compact fluorescent lamp (EL20W; OSRAM dulux superstar). At specified time intervals, 2 mL of illuminated solutions was collected to record the absorption spectrum by UV–visible spectrometer. PL spectrum was performed to verify the recombination state of electron–hole pairs in samples (PL spectrometer with 473 nm diode laser; G9800A; Agilent Technologies, Santa Clara, CA, USA).

### 3.3 Results and discussions

#### 3.3.1 Structural component, surface morphology, and optical properties

All structural components of the as-synthesized samples were confirmed by XRD as shown in Fig. 5. The XRD patterns of GO and ZnO/rGO were recorded in the  $2\theta$  range of 5 to  $80^\circ$ . The XRD patterns of GO show peaks at  $2\theta$  values of  $11.2^\circ$  corresponding to (002) [107]. The as-synthesized hybrid samples of ZnO, ZnO/rGO (10%), ZnO/rGO (20%), and ZnO/rGO (30%) exhibit prominent peaks at  $2\theta$  values of  $31.8^\circ$ ,  $34.4^\circ$ , and  $36.2^\circ$ , corresponding to a ZnO wurtzite phase (JCPDS card of 89-13971) and indexed as (100), (002), and (101) reflection planes, respectively. From the XRD analysis, the lattice constants of ZnO with different GO contents can be calculated by a hexagonal space lattice equation:

$$\frac{1}{d^2} = \left(\frac{4}{3}\right)\left(\frac{h^2 + hk + k^2}{a^2}\right) + \frac{l^2}{c^2} \quad (12)$$

where  $d$  is the interplanar distance and  $h$ ,  $k$ , and  $l$  are miller indices.  $a$  and  $c$  refer to the lattice constant of the hexagonal structure. The size of a ZnO crystal can be calculated using Scherer's equation [108]:

$$t = \left(\frac{K\lambda}{\beta \cos \theta}\right) \quad (13)$$

where  $t$  is crystal size,  $K$  is a dimensionless shape factor,  $\lambda$  is the X-ray wavelength,  $\beta$  is the broadening at half of the maximum intensity, and  $\theta$  is Bragg's angle. Lattice constant and crystal size were calculated and summarized in Table 5.

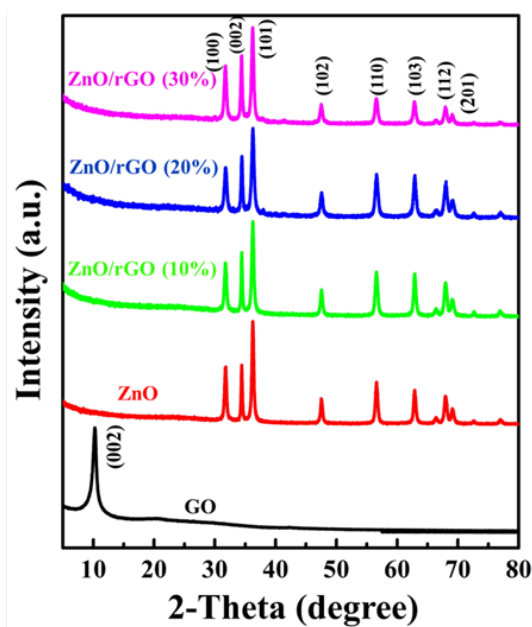


**Fig. 5:** XRD pattern of GO and as-synthesized ZnO/rGO.

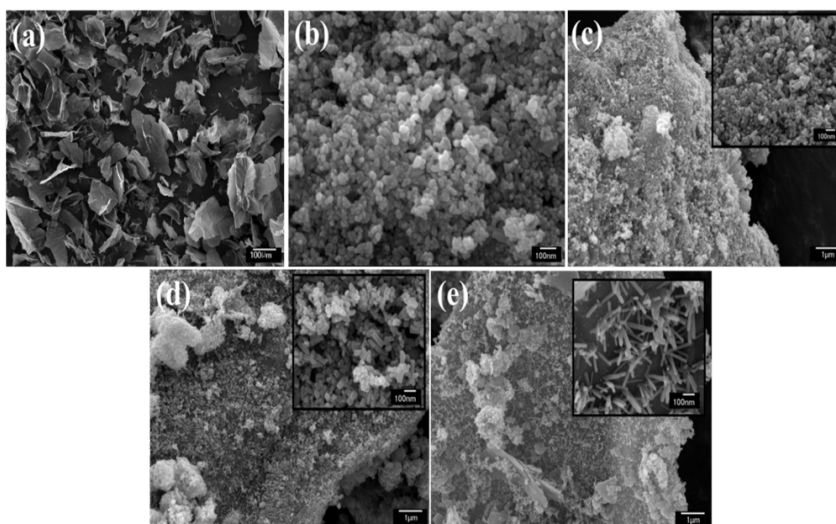


**Fig. 6:** Field-emission scanning electron microscopy (FE-SEM) images of the (a) GO sheet, (b) ZnO, (c) ZnO/rGO (10%), (d) ZnO/rGO 20%, and (e) ZnO/rGO ZnO/rGO (30%). The inset shows the high magnification of FE-SEM image for each condition.

**Table 5:** Average diameter, length, crystal size, lattice parameter of GO and as-synthesized samples.

Samples	SEM			XRD		
	Diameter (nm)	Length (nm)	Shape	Crystal size (nm)	Lattice parameter (Å)	
					a	c
ZnO	31.7	-	Nanoparticles	33.77	3.299	5.209
ZnO/rGO (10%)	25.8	44.1	Nanoparticles/ Nanorods	30.66	3.299	5.207
ZnO/rGO (20%)	23.8	63.8	Nanoparticles/ Nanorods	24.92	3.299	5.203
ZnO/rGO (30%)	24.6	106.8	Nanorods	25.62	3.300	5.209

As GO content increased, the diffraction peak corresponded to the (002) reflection plan of ZnO intensified. This intense (002) peak plays a significant role in tunabilities of ZnO morphology in ZnO/rGO. However, the absence of a GO peak in ZnO/GO implied to a complete exfoliation and dispersion of GO into the ZnO [109], [110].

The surface morphology of ZnO/rGO was observed by FE-SEM, as shown in Fig. 6(a)-6(e). The figure demonstrates the morphology of GO and ZnO/rGO containing 0%, 10%, 20%, and 30% GO. The morphology of GO consisted of two-dimensional sheets with an average length of 89.3 m. The average diameter of ZnO in ZnO/rGO containing the different amounts of GO is summarized in Table 5. Interestingly, the increase in GO additive did not change the diameter of ZnO, but tuned the morphology of ZnO in different as-synthesized ZnO/rGO. ZnO in the absence of GO took on a spherical shape with a diameter of 31.7 nm. However, ZnO in ZnO/rGO samples with 10 and 20% GO formed a rod shape along with spherical nanoparticles. At 30% GO, nanorods with a diameter of 24.6 nm and a length of approximately 106.8 nm could be seen. An increase in GO content is, therefore, a synergistic effect that controls dimensional ZnO formation through a tuning of the dimensional ZnO nanostructures from nanoparticles to nanorods, which corresponds to XRD results.

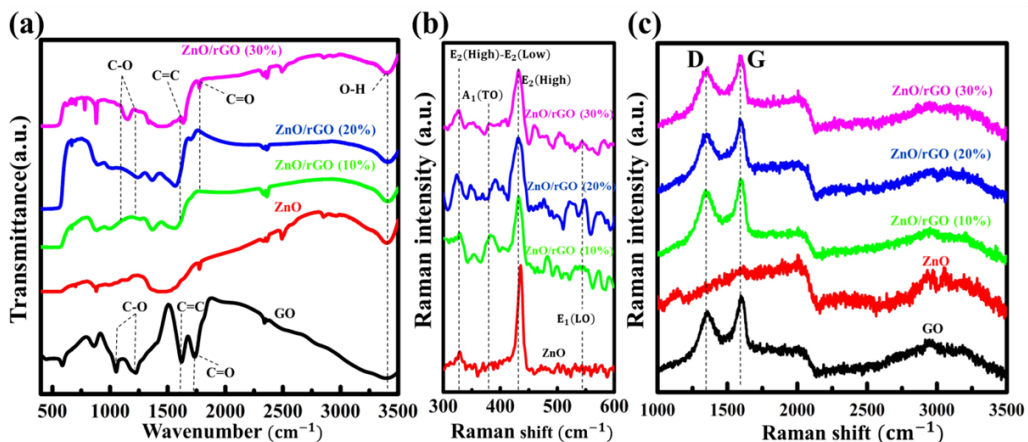


**Fig. 7:** Surface characterization of ZnO/rGO. (a) FT-IR spectra and Raman spectra, (b) ZnO component, and (c) GO component.

Fig. 7(a) shows the FT-IR spectra of GO and as-synthesized samples. GO shows the presence of different peaks at  $3450\text{ cm}^{-1}$ ,  $1700\text{ cm}^{-1}$ ,  $1620\text{ cm}^{-1}$ ,  $1226\text{ cm}^{-1}$ , and  $1052\text{ cm}^{-1}$ , corresponding to O–H stretching vibration of the surface-absorbed water molecules, carbonyl group (C=O), C=C aromatic configurable vibration, carboxyl C–O, and alkoxy C–O stretching, respectively [111]. The intensity of the peaks corresponding with oxygen functionalities in ZnO/rGO was reduced and some peaks ( $1226\text{ cm}^{-1}$  and  $1052\text{ cm}^{-1}$ ) disappeared. This suggests that the majority of the oxygen functional groups in GO was reduced.

Raman spectra of GO and as-synthesized ZnO/rGO are shown in Fig. 7(b)–7(c). The observed spectrum of GO exhibiting typical D and G bands is shown in Fig. 7(c). The D band at  $1359\text{ cm}^{-1}$  is attributed a structural defect in the hexagonal graphitic layers, whereas the G band at  $1597\text{ cm}^{-1}$  can be assigned to  $sp^2$  carbon-type structure [112]. As-synthesized ZnO/rGO exhibited

an increased intensity ratio between the D and G peaks<sup>r\*\*</sup> ( $I_D/I_G$ ,) compared with GO. In addition, the D and G band values shifted to lower frequencies as summarized in Table 6. Along with FT-IR observation, this suggests a reduction of oxygen functional groups in GO and restoration of new graphitic domains from the amorphous region of GO [113], [114]. Moreover, the Raman spectrum of pure ZnO exhibited optical phonon vibrational peaks corresponded to  $E_2(\text{high})$ - $E_2(\text{low})$ ,  $A_1(\text{TO})$ ,  $E_2(\text{high})$ , and  $E_1(\text{LO})$  vibrational modes (Fig. 7(b)). The most intense peak,  $E_2(\text{high})$ , is associated with intrinsic stress of ZnO wurtzite at  $435.84 \text{ cm}^{-1}$ . The  $E_1(\text{LO})$  peak at  $566.79 \text{ cm}^{-1}$  is attributed to surface defect formation such as dislocation and oxygen-zinc vacancy states [19]. As shown in Table 6, the intensity ratio of the  $E_1(\text{LO})$  peak to the  $E_2(\text{high})$  peak<sup>r\*\*</sup> increased in the as-synthesized ZnO/rGO at different GO additive and reached a maximum at 0.686 in ZnO/rGO (20%) sample. This indicates that the most defect/disorders occurs in the ZnO/rGO (20%) sample, compared with the other as-synthesized ZnO/rGO samples and GO compared with other as-synthesized ZnO/rGO with different amounts of GO content. The optimization of adequate amounts of GO is, therefore, necessary to control defect formation in ZnO/rGO.

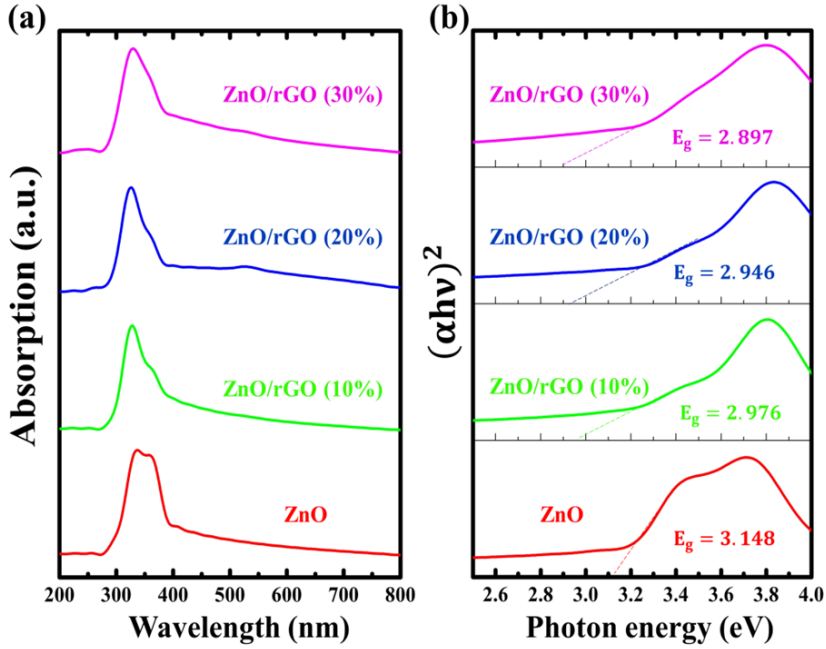


**Fig. 8:** UV–visible spectroscopy of as-synthesized ZnO/rGO: (a) absorption spectra and (b) energy band gap.

The optical properties of ZnO/rGO were studied by UV–visible spectroscopy. Fig. 8(a) shows the absorption spectra of ZnO/rGO synthesized with different amounts of GO. The optical absorption coefficient ( $\alpha$ ) can be calculated using Eq. (14) [115]:

$$(\alpha h\nu)^2 = D(h\nu - E_g) \quad (14)$$

where  $D$  is constant,  $h\nu$  is the incident photon energy and  $E_g$  is the optical band gap. According to Eq. (14), the band gap of materials has been calculated by conventional extrapolation of the plot of  $(\alpha h\nu)^2$  and  $h\nu$  at  $\alpha = 0$ , as shown in Fig. 8(b). The optical band gap value of as-synthesized ZnO/rGO is summarized in Table 6. The optical band gap decreased with an increase in the amount of GO content. For comparison purposes, the band gap energy of pristine ZnO shows



higher value (3.143) compared with as-synthesized ZnO/rGO samples (2.897–2.976). The decrease in the band gap of ZnO/rGO can be explained by the increase in the surface charge between ZnO and rGO, which results in the optical band gap shifting to a higher wavelength. This is similar to a result obtained by R. Paul et al. [13]. In addition, the presence of defects in the as-synthesized ZnO/rGO samples can be determined using Urbach absorption tail energy [116], [117] by

$$(E_u)^{-1} = \frac{\ln \alpha}{h\nu} \quad (15)$$

where  $E_u$  is the Urbach absorption tail energy, which is assumed to be the width of the exponential edge. The Urbach absorption tail energy shows a smearing of absorption edge, supplying information on the presence of impurities or defects in the as-synthesized ZnO/rGO. A close examination of the results reveals that an increase in GO additive increases the value of  $E_u$  to certain GO content, after which the  $E_u$  value decreases. The maximum value of  $E_u$  was obtained at a GO content of 20%, indicating to the highest presence of defects/disorder in ZnO/rGO synthesized at 20% GO. These results confirm the existence of defect in ZnO/rGO assisted with Raman data, which also showed the highest values of the  $E_1(\text{LO})$  peak to the  $E_2(\text{high})$  peak ratio at ZnO/rGO synthesized at 20% GO.

ZnO/rGO samples were subjected to a X-ray photoelectron spectrometer to quantify their oxidation state, oxygen vacancy, and surface chemical composition, as shown in Fig. 9(a)–9(c). Fig. 9(a) shows the XPS survey spectra of all-synthesized ZnO/rGO, pristine ZnO, and GO with the presence of C, O, and Zn elements. The deconvoluted C1s peaks were fitted to three Gaussian peaks, consisting of  $sp^2/sp^3$  carbon (C-C/ C=C, 284.35–284.95 eV), C–OH/ C–O/ C–Zn (286.98–286.42 eV), and C=O/ COOH (287.5–289) [111], [112],

[118], as shown in Fig. 9(b). It can be clearly seen that the peak intensity of oxygen bonded carbon was decreased after the hydrothermal process. This suggests that the reduction of oxygen functional groups in GO. Fig. 9(c) shows the deconvoluted O1s of ZnO/rGO compared with pristine ZnO. The O1s peak was deconvoluted into three Gaussian peaks, corresponding to  $O_L$ ,  $O_V$ , and  $O_C$  [79], [119], [120]. The  $O_L$  peak at 530.80–531.00 eV is been attributed to lattice oxygen ion ( $O_2^-$ ) in the ZnO wurtzite structure. The  $O_V$  peak at 531.53–531.95 eV has been assigned to  $O_X^-$  ion oxygen deficient region (oxygen vacancy) and the  $O_C$  peak at 532.47–533.20 eV corresponds to the chemisorbed oxygen on the surface. The % area and peak position of O 1s peak was summarized in Table 7. As mentioned above, the  $O_V$  peak is related to the oxygen vacancy which the intensity of  $O_V$  peak can be connected to the concentration of the oxygen vacancy in ZnO/rGO. In Fig. 9(c), the intensity of  $O_V$  peak increased with an increase in GO additive. The ratio of  $O_V/O_L$  was used to compare the presence of oxygen vacancy and oxygen lattice in materials [121]. As seen in Table 7, the  $O_V/O_L$  ratio shows the highest value in the ZnO/rGO (20%) sample, suggesting that oxygen vacancy is intensively constructed in ZnO/rGO (20%) more than other conditions and pristine ZnO. Along with Raman and UV–Vis results; this is in good agreement to confirm that the GO additive has an effect on oxygen vacancy formation in ZnO/rGO.

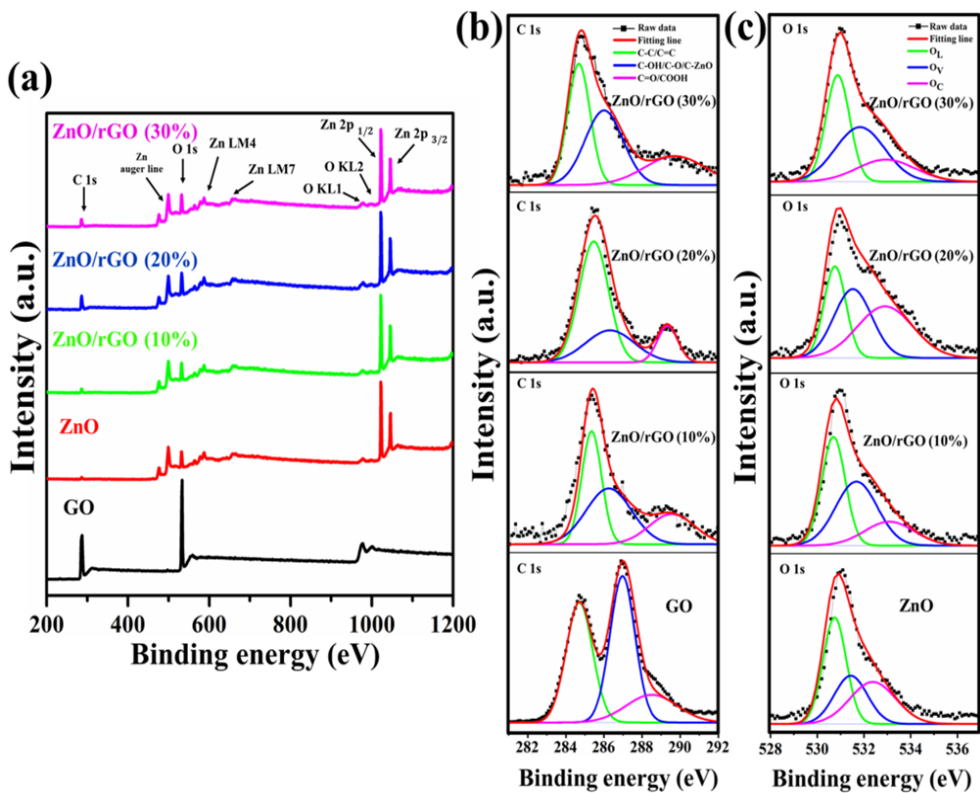


**Fig. 9:** (a) The X-ray photoelectron spectroscopy (XPS) survey spectra obtained for GO. The deconvoluted (b) C 1s and (c) O 1s of GO, pristine ZnO, and as-synthesized ZnO/rGO.

**Table 6:** Raman spectra peak of GO and as-synthesized samples.

Samples	Raman data				UV-Vis data		
	ZnO vibrational mode ( $\text{cm}^{-1}$ )		GO vibrational mode ( $\text{cm}^{-1}$ )		$E_g$	$E_u$	
	$E_2(\text{high})$	$E_1(\text{LO})$	$r^*$	D peak	G peak	$r^{**}$	
GO	-	-	-	1358.61	1596.77	0.815	-
ZnO	435.84	566.97	0.219	-	-	-	3.148 0.241
ZnO/rGO (10%)	433.97	570.83	0.613	1343.18	1594.70	0.870	2.976 0.549
ZnO/rGO (20%)	431.98	566.01	0.686	1351.86	1588.10	0.867	2.946 0.658
ZnO/rGO (30%)	434.87	578.54	0.664	1357.66	1588.10	0.862	2.897 0.646

**Table 7:** Atomic percentage of fitted high-resolution spectra of the O 1s of ZnO/rGO nanocomposites and pristine ZnO.

Sample	XPS – O 1s								
	$O_L$				$O_V$				$O_V/O_L$ ratio
	Peak position	% Area	Peak position	% Area	Peak position	% Area	Peak position	% Area	
ZnO	530.83	41.30	531.53	26.67	532.47	32.03	532.47	0.646	
ZnO/rGO (10%)	530.82	40.08	531.80	41.50	533.20	18.42	533.20	1.035	
ZnO/rGO (20%)	530.89	26.79	531.64	34.78	533.02	38.43	533.02	1.298	
ZnO/rGO (30%)	531.00	38.84	531.95	41.50	533.05	19.66	533.05	1.068	

### 3.3.2 UV Sensing Measurement

UV sensor devices based on as-synthesized ZnO/rGO at different amounts of GO content were fabricated and tested at room temperature. The UV sensing measurement was investigated by using a UV illumination source with a wavelength of 365 nm and 2 V of bias voltage. The current characteristic was measured in “on” and “off” states for the photocurrent and dark current, respectively, over several cycles. To minimize the effect of natural light, all measurements were conducted in a dark box and the illumination time was fixed at 30 s. Photosensitivity was defined by the ratio of photocurrent and dark current ( $S = I_{UV}/I_D$ ) as a function of time. Photosensitivity was calculated and compared for each condition, as summarized in Table 8. The time interval which the current increased to 90% of the maximum value (response time) was also determined. The UV sensor device performance was studied with and without applying bending strain.

Current–time (I–t) and current–voltage (I–V) characteristics based on ZnO/rGO without a bending effect are shown in Fig. 10(a) – 10(b). As seen in Fig. 10(b), the I–V curve shows the characteristics of ohmic contact between ZnO/rGO and a silver electrode. Pristine ZnO shows photosensitivity lower than as-synthesized ZnO/rGO as exhibited in Table 8. This indicates that GO additive can improve photosensitivity. Fig. 10(a) shows how the photocurrent increased with an increase in GO content to 20% and then decreased as GO content rose to 30%. This is due to the declined ZnO and cut-off light of the active area of ZnO, leading to a decrease in photocurrent [122]. An increase in GO additive is therefore a synergistic parameter to enhance the photosensitivity, in respect of

increasing carrier concentration from surface disorder and electron adsorption on the surface.

The UV sensing characteristics were demonstrated by changing several bending radii, as shown in Fig. 10(c) – 10(d). For the UV sensing device based on pristine ZnO, photosensitivity increased when applying a 12.5 mm bending radius from 1.51 to 1.82. A decrease in bending radius resulted in a decrease photosensitivity. Similar to the as-synthesized ZnO/rGO, photosensitivity showed the same trend, which was optimized with an applied bending radius of 12.5 mm (Table 8). The comparison of photosensitivity of as-synthesized ZnO/rGO at a different applied bending radius is depicted in Fig. 10(c) – 10(d). As-synthesized ZnO/rGO (20%) showed the maximum photosensitivity (8.81), which was improved by 123.59% compared with free-applied bending (Fig. 10(c)). The as-synthesized ZnO/rGO (30%) sample showed an improvement in photosensitivity by 244.57%, with an applied 12.5 mm bending radius. However, decreasing bending radius below 10 mm led to photosensitivity reduction.

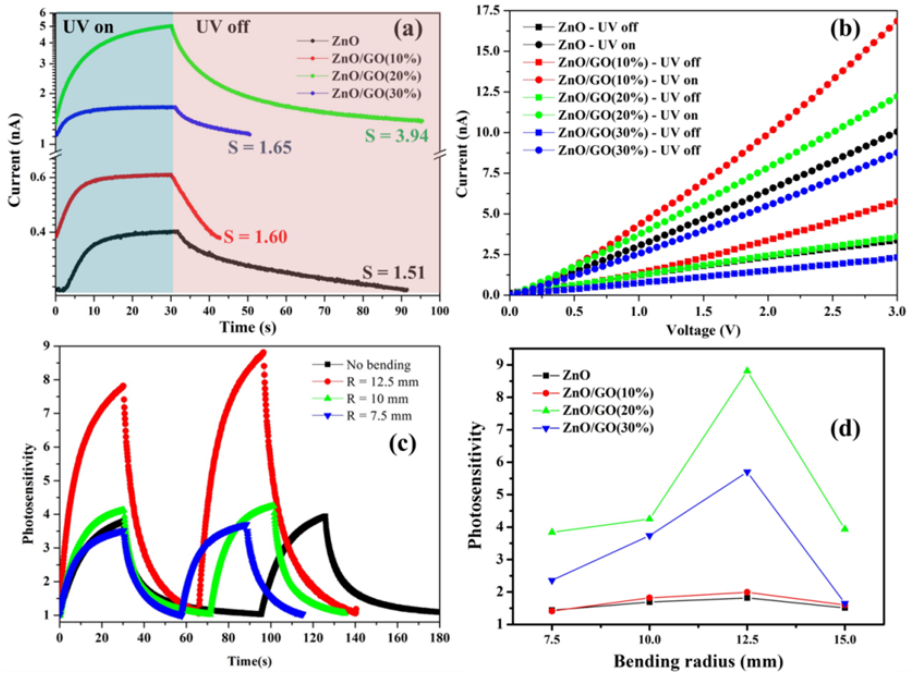


**Fig. 10:** (a) Current-time (I-t) of ZnO/rGO, (b) I-V characteristic of as-synthesized ZnO/rGO without bending strain, (c) Current-time (I-t) of ZnO/rGO (20%) with bending radius and. (d) comparison of photosensitivity.

The improvement in the photosensitivity of ZnO/rGO with and without bending strain can be explained in a schematic model, as shown in Fig. 11. Typically, the photosensitivity of a UV detector mechanism based on n-type ZnO nanostructures can be described by the chemisorption of oxygen. Without UV illumination, oxygen molecules adsorb to the surface, resulting in a decrease in surface conductivity, which can be expressed by  $O_2(g) + e^- \rightarrow O_2^-(ads)$ , as shown in Fig. 11(a) left side. Upon UV illumination, electron-hole pairs are generated by  $h\nu \rightarrow e^- + h^+$ . Adsorbed oxygen ions will be discharged by holes to produce oxygen molecules and release trapped electrons to the conduction channel, resulting in an increase of surface conductivity, which can be expressed



as  $\text{O}_2^-(ads) + h^+ \rightarrow \text{O}_2(g)$ , as shown in the right side of Fig. 11(a). The photosensitivity performance depends on the surface-to-volume ratio and surface defects (oxygen vacancies and/or zinc interstitials), which are regularly responsible for carrier concentration. The more defects exist in the sample, the more carriers will increase.

For the bending effect, as shown in Fig. 11(b), the possibility of improved photosensitivity can be described in two aspects. First, with incremental surface defects [123], [124], the applied bending on ZnO/rGO will expand the surface area and increase the surface defect between ZnO/rGO-ZnO/rGO interfaces. More oxygen could therefore travel to rGO sheet and increase oxygen adsorption, leading to improvement in photosensitivity under UV illumination, as shown in Fig. 11(b). A decrease in bending radius did not only increase oxygen adsorption on the sensing surface, but also resulted in collateral destruction (cracking) of the structural sensing surface and contact between the sensing surface and the silver electrode (in the case of application of a bending radius over the elastic limit of materials). This would result in carrier pathway deformation, carrier mobility, and photosensitivity reduction. However, an appropriate bending radius could increase oxygen adsorption and not result in cracking on the sensing surface; this would improve photosensitivity. The second aspect is the piezoelectric effect [14], [26]; this is due to the growth of ZnO, which adhered to the rGO surface, assuming that rGO can transfer all of its bending force to ZnO nanostructures. When bending strain was applied to the substrate, a piezoelectric charge was induced on the ZnO surface, leading to an increase in adsorbed oxygen on the surface and producing a larger depletion region, as shown in Fig. 11(b), left side. Under UV light, oxygen desorption

released electrons back to the conduction channel, leading to the observed increased photosensitivity as shown in Fig. 11(b) right side. The present research found that an increase in the GO additive can improve the photosensitivity of a UV sensing device based on ZnO/rGO, in terms of induced intrinsic disorder/oxygen vacancy formation in ZnO. Additionally, a UV sensing device with applied bending exhibits superior photosensitivity in respect of more surface area and surface defect creation, providing more absorbed oxygen and more induced negative piezoelectric charge from piezoelectric effect. We also compared the photosensitivity in our work with previously reported research in Table 9. This can be clearly seen that as-synthesized ZnO/rGO has good photosensitivity with faster response time compared with other reports.

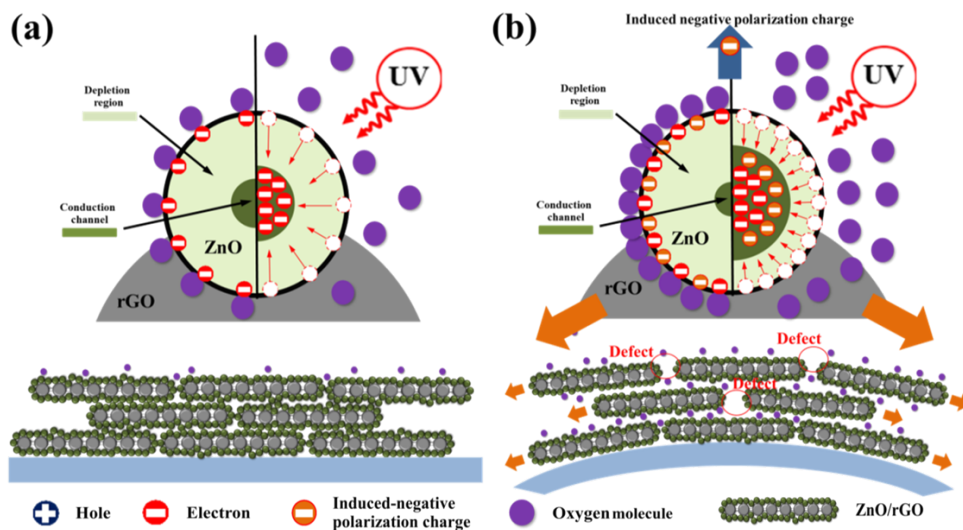


**Fig. 11:** (UV sensing mechanism of as-synthesized ZnO/rGO (a) without, and (b) with bending strain.

### 3.3.3 Photocatalytic Activity Studies

The photocatalytic activity of ZnO/rGO was measured in terms of the degradation of MB under visible light. The MB absorption band was observed at 664 nm. The change in the absorption peak of MB was used to measure variation in MB concentration with a visible light irradiation time of 0, 5, 10, 20, 40, and 60 min as shown in Fig. 16. Fig. 12(a) shows the variation in the absorption band of the MB solution with the presence of ZnO/rGO sample as a function of visible light irradiation time. The photodegradation kinetic model can be explained by a generic modal equation as a logarithm of time and MB concentration, as given by

$$\ln \frac{C_t}{C_0} = -k_c t \quad (16)$$

where  $C_0$  and  $C_t$  are the absorption of MB solution before and after visible light irradiation, respectively;  $k_c$  is photocatalytic reaction rate constant; and  $t$  is irradiation time. From Fig. 12(a), it can be seen that the concentration of MB has been reduced with increasing irradiation time, indicating the photodegradation of MB in the presence of ZnO/rGO. Additionally, the photodegradation of MB in ZnO/rGO was considerably greater than in pure ZnO. Fig. 16 shows that ZnO/rGO nanocomposites with 20% GO exhibited the highest MB photodegradation activity (93.78%) within 60 min under visible light compared with 30% GO (86.43%), 10% GO (56.62%), and without GO content (4.11%). A comparison of the as-calculated degradation rate constants is shown in Table 8. This result reveals that ZnO/rGO with 20% GO had the highest photocatalytic activity, with a rate constant of  $0.0482 \text{ min}^{-1}$ , which is almost 18 times greater than pristine ZnO ( $0.0027 \text{ min}^{-1}$ ) and other as-synthesized ZnO/rGO samples.

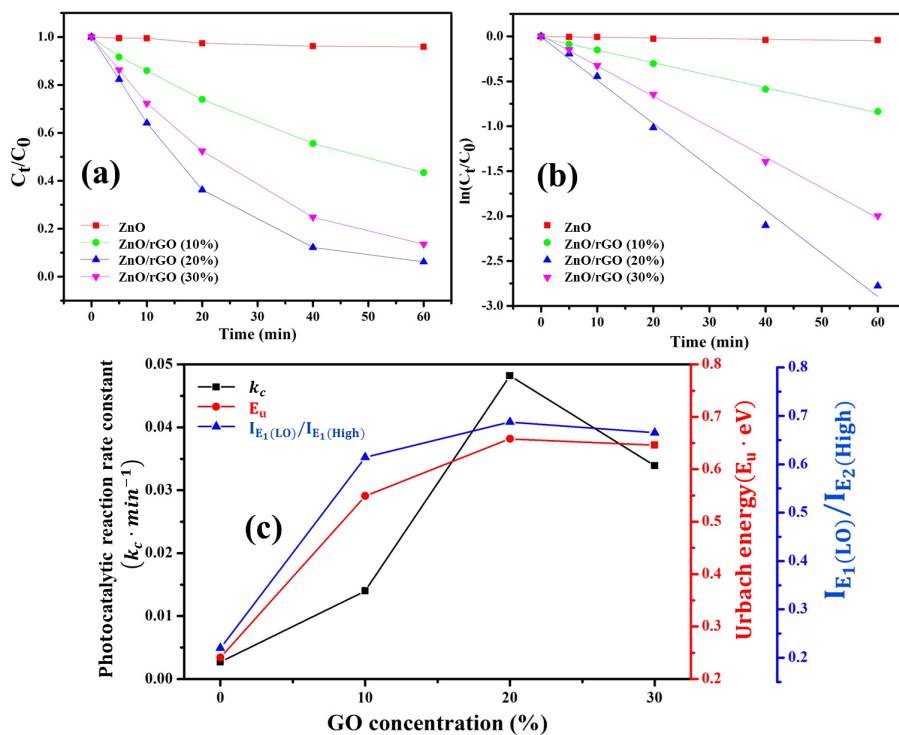


**Fig. 12:** (a) Photodegradation of methylene blue (MB) in the presence of various photocatalysts under visible light illumination, (b) apparent first-order kinetics of photocatalytic degradation of MB, and (c) the effect of GO concentration on photocatalytic reaction rate constant and defect evaluation values.

As a result, we can draw a conclusion that GO additive plays an important role in controlling photocatalytic activities by induced-defect/oxygen vacancy formation in ZnO. Furthermore, it provides an alternative carrier pathway and separates photogenerated electron-hole pairs preventing charge carrier recombination. Photodegradation of MB in this work is compared with previously reported literatures in Table 10. It can be seen that as-synthesized ZnO/rGO shows better photodegradation rate (%) of MB with shorter UV illumination time.

The photocatalytic activity mechanism by ZnO/rGO is illustrated in Fig.13.

ZnO acted as an electron–hole pair generator, and rGO acted as the carrier pathway. The as-synthesized ZnO/rGO was excited to generate electron–hole pairs of ZnO by visible light illumination. Then, the photogenerated electrons move up freely to the conduction band of ZnO and transfer to the nearest rGO surface. Additionally, in the ZnO/rGO heterojunction, the photogenerated electron in ZnO can freely move to rGO, as the work function of rGO is lower than the conduction band level of ZnO. This will provide alternative carrier pathway and enhance charge separation which have a beneficial effect for photocatalytic [77]. The photogenerated electrons and holes reacted with oxygen and hydroxyl groups to form superoxide radicals and hydroxyl radical ions. The generated radicals then degrade MB and produce oxidized organic products. The observed enhanced photocatalytic activity can be attributed to the surface properties of nanocomposites that provide a high surface area, enhancing MB absorption [78]. Photodegradation abilities generally depend on photogenerated electron–hole pairs. In the case of pristine ZnO with few disorder and surface defects, the photogenerated electrons and holes undergo quick recombination, leading to a lower concentration of photogenerated electron–hole pairs compared with ZnO/rGO with high disorder and surface defects (as evaluated by Raman spectra, Urbach energy, and XPS).

To additionally support the charge recombination information, a room-temperature PL spectrometer with excitation wavelength at 325 nm was performed to show up the charge recombination of ZnO and as-synthesized ZnO/rGO. As shown in Fig. 17, the PL spectra of all the as-prepared samples show a sharp emission peak in the UV region of 380 nm, which is related to the band-to-band radiative recombination of the photogenerated electron–hole.

Additionally, three minor, broad emission peaks in the visible region of 480 to 625 nm were also found, corresponding to defects of ZnO, such as oxygen vacancy and zinc vacancy. No detectable emission peak shift was found in any sample. However, luminescence quenching of as-synthesized ZnO/rGO was observed, in the order of ZnO/rGO (20%), (30%), (10%), and pristine ZnO, respectively. This suggests to ZnO/rGO (20%) has lower charge carrier recombination compared with other ZnO/rGO samples and pristine ZnO. Regarding the Raman, UV visible, and XPS analysis, the lower charge carrier recombination may be due to the existence of more defect/oxygen vacancy. Additionally, the GO additive provided the additional carrier pathway, which can increase charge separation efficiency and prolong photocatalytic reaction lifetime [80], [93], [125].

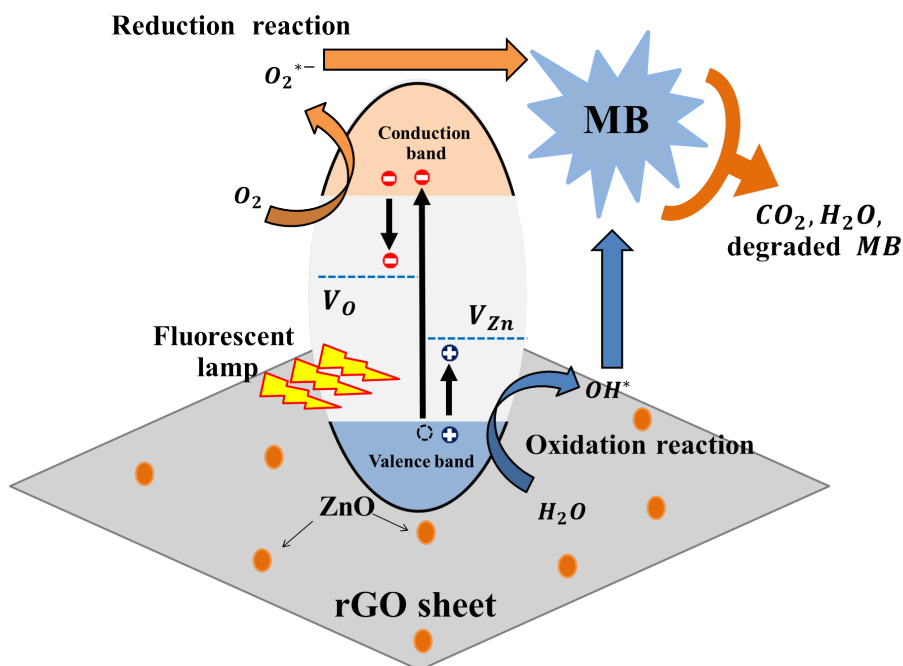


**Fig. 13:** Schematic diagram of photo-charge generation and charge transfer for MB degradation using as-synthesized ZnO/rGO.

**Table 8:** Photosensitivity (increase/decrease percentage) of UV sensing and photocatalytic properties based on ZnO/rGO nanocomposites.

Samples	Photosensitivity ( $\uparrow\downarrow$ %)			Photocatalytic activity			
	No bending	Bending radius ( $R_b$ )		MB degradation	$k_c$ ( $min^{-1}$ )	$R^2$	
		12.5 (mm)	10 (mm)				7.5 (mm)
ZnO	1.51	1.82 ( $\uparrow$ 21.47%)	1.69 ( $\uparrow$ 12.70%)	1.44 ( $\downarrow$ 3.77%)	4.11%	0.0027	0.8793
ZnO/rGO (10%)	1.60	1.99 ( $\uparrow$ 23.55%)	1.82 ( $\uparrow$ 13.20%)	1.41 ( $\downarrow$ 12.21%)	56.62%	0.0140	0.9982
ZnO/rGO (20%)	3.94	8.81 ( $\uparrow$ 123.59%)	4.25 ( $\uparrow$ 7.85%)	3.84 ( $\downarrow$ 2.45%)	93.78%	0.0482	0.9901
ZnO/rGO (30%)	1.65	5.70 ( $\uparrow$ 244.57%)	3.74 ( $\uparrow$ 126.22%)	2.36 ( $\uparrow$ 42.83%)	86.43%	0.0339	0.9985

### 3.4 Conclusions

A simple one-pot solvothermal technique to prepare ZnO/rGO nanocomposites with high photosensitivity and high photodegradation of MB has been demonstrated. This study indicates that using the optimal amount of GO additive plays a significant role in not only nanoparticle–nanorod tunability, but also in inducing the intrinsic defect formation of ZnO. The ZnO/rGO based on UV detection and photocatalyst outperformed pristine ZnO, as the GO additive generates more defects and disorder, leading to increase absorbed oxygen for carrier concentration increment. Additionally, it provides the alternative charge carrier pathway to prevent charge carrier recombination and prolong photocatalytic reaction lifetime. ZnO/rGO (20%) shows the highest photosensitivity of 3.94 with 18.16 s of response time and degrades 93.78% of MB in 1 h. This makes it a promising candidate on double application of environmental monitoring and pollutant treatment.



### 3.5 Supporting informations

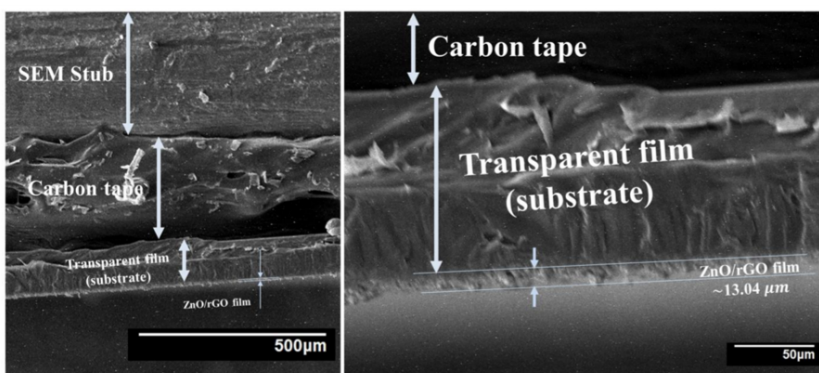


**Fig. 14:** The thickness of prepared films by spray coating.

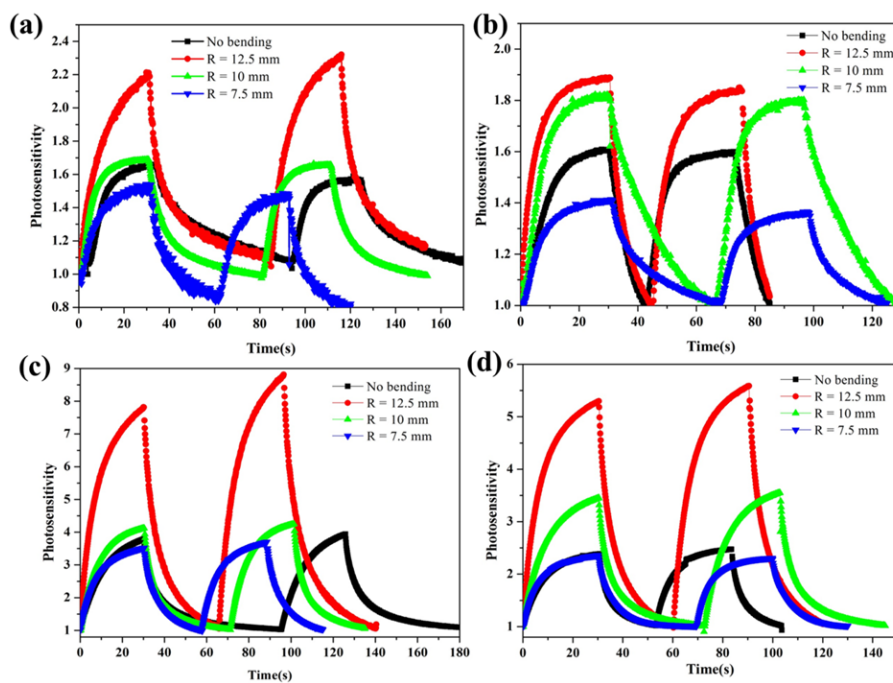


**Fig. 15:** Current of as-synthesized ZnO/rGO with bending radius; (a) ZnO, (b) ZnO/rGO (10%), (c) ZnO/rGO (20%), and (d) ZnO/rGO (30%).

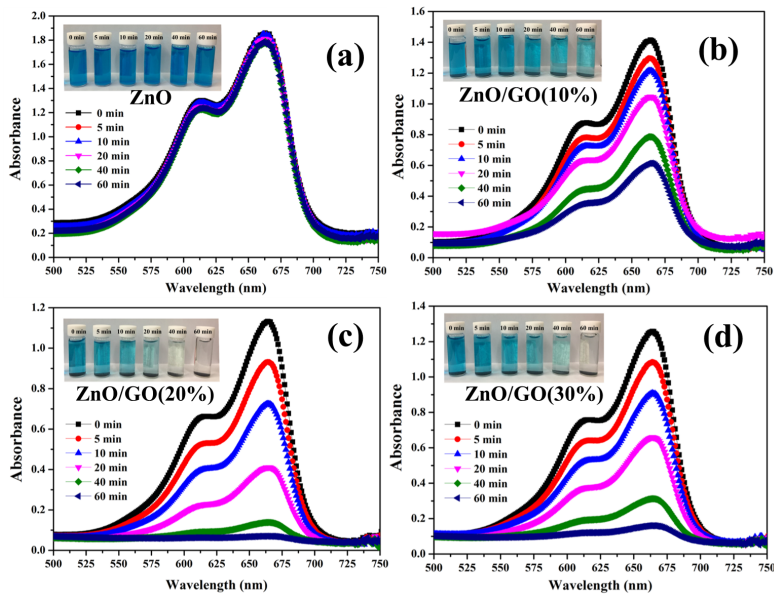


**Fig. 16:** Time-dependent absorption spectra of Methyl blue (MB) solution under visible light using (a) ZnO, (b) ZnO/rGO (10%), (c) ZnO/rGO (20%), and (d) ZnO/rGO (30%) as a photocatalyst.

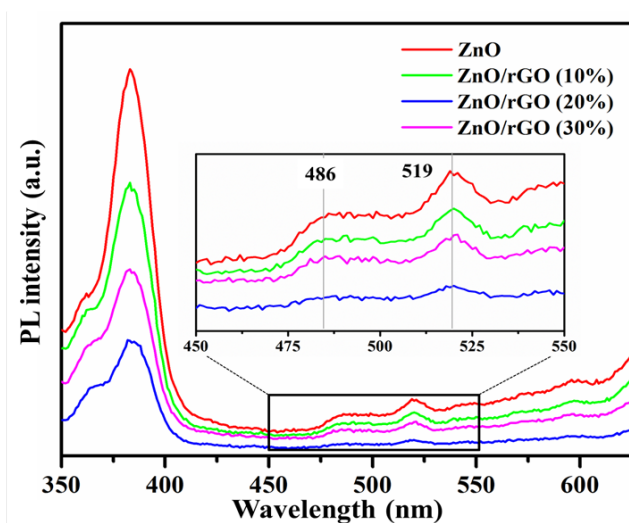


**Fig. 17:** The photoluminescence spectra of pristine ZnO and as-synthesized ZnO/rGO.

**Table 9:** Comparisons of photosensitivity and time-dependent photocurrent response between the present work and other reported UV detectors.

Structure	Substrate	UV intensity (W/cm <sup>2</sup> )	Bias voltage (V)	Dark current (A)	Photosensitivity ( $I_{UV}/I_{Dark}$ )	Response time (s)	Ref
Mg/ZnO thin film	glass	$3.20 \times 10^{-3}$	4	$4.64 \times 10^{-3}$	1.01	-	[126]
ZnO nanowires	SiO <sub>2</sub> /Si	$0.42 \times 10^{-3}$	1.5	$0.50 \times 10^{-6}$	<4	-	[127]
ZnO nanowires	SiO <sub>2</sub> /Si	$2 \times 10^{-3}$	0.1	$12.70 \times 10^{-6}$	1.51	0.2	[128]
	SiO <sub>2</sub> /Si	$19.50 \times 10^{-3}$	0.1	$12.50 \times 10^{-6}$	1.4	0.3	[128]
ZnO	p-Si	0.80	3	$3.50 \times 10^{-6}$	1.71	-	[129]
Ti-doped ZnO thin film	glass	$2 \times 10^{-3}$	5	$15.00 \times 10^{-9}$	6.80	135	[130]
ZnO/rGO	glass	$0.80 \times 10^{-3}$	2	$7.00 \times 10^{-6}$	4	44	[131]
ZnO/GO	glass	$0.80 \times 10^{-3}$	4	-	20.1	-	[132]
ZnO/rGO(20%)	transparent film	$0.62 \times 10^{-3}$	2	$3.98 \times 10^{-9}$	8.81	18.16	This work

**Table 10:** Comparisons of photocatalytic activity between the present work and other reported researchs.

Catalyst	Catalyst concentration (g L <sup>-1</sup> )	Light source	MB concentration (mg L <sup>-1</sup> )	Degradation rate (%) and time (s)	k <sub>c</sub> (min <sup>-1</sup> )	ref
ZnO/GO(3%)	0.4	Metal halide lamp	10	92%/30	0.042	[133]
ZnO/g-C <sub>3</sub> N <sub>4</sub> /GO (50%)	0.3	Visible light	10	99%/90	0.030	[134]
GO/ZnO (1:2)	0.4	UV light (254 nm)	5	94.5%/60	-	[135]
ZnO/rGO (2.5%)	0.5	Mercury lamp (310-400 nm)	10	80%/120	0.012	[136]
ZnO NPs/rGO	0.3	Hg lamp (365 nm)	10	99.5%/180	-	[137]
ZnO/rGO	0.1	Mercury lamp (365-366 nm)	10	83%/10	-	[138]
ZnO/rGO	0.15	Hg lamp (365 nm)	5	88%/260	-	[139]
ZnO/rGO (1.5%)	0.2	Natural sunlight	5	82.3%/-	-	[140]
ZnO/g-C <sub>3</sub> N <sub>4</sub>	0.2	4-Visible light lamp (545 nm)	10	99%/180	0.033	[141]
ZnO/rGO (20%)	0.2	Fluorescent lamp	10	93.78%/60	0.0482	This work

## **4 Cerium-Oxide-Nanoparticle-Decorated Zinc Oxide with Enhanced Photocatalytic Degradation of Methyl Orange**

### **4.1 Introduction**

In this chapter, we present the surface modification of ZnO by using metal doping. Min et al. synthesized ZnO nanoparticles with copper doping by using a sol-gel technique for photocatalytic applications, and these showed higher methyl blue degradation (88%, 6 h) compared with undoped ZnO [41]. In recent years, rare-earth (RE) metals have been used as dopants in RE/ZnO; these include Er[54], [142], Eu[55], [56], [143], Nd[57], [58], Tm[51], and La[59]–[61]. Suwanboon et al. synthesized La-doped zinc oxide nanoparticles (La/ZnO NPs) using a precipitation and mechanical milling technique, and they investigated the blue-light-fluorescent-lamp-driven photodegradation activity of methyl blue. Photocatalysts based on La/ZnO NPs showed that the photocatalytic degradation performance improved with an increase in La doping, and the methyl orange (MO) degradation reached 93% after 120 min under light illumination [144]. Kumar et al. reported the enhanced photocatalytic decomposition of Rhodamine B dye by chemically synthesized Nd-doped ZnO powder. Introducing Nd into ZnO can induce defect formation (like antisite oxygen and interstitial oxygen) in Nd-doped ZnO powder, which would play an important role in trapping electron carriers and charge separation [145]. Presently, there are few research reports on Ce-doped ZnO nanocomposites for photocatalytic applications [146], [147]. Shen et al. prepared the 3D flower-like mesoporous cerium–zinc oxide for

sunlight-driven photodegradation of Rhodamine B (RhB), which showed 85.1% degradation in 125 min [62]. Overall, researchers reported that RE doping can generate different defects in RE/ZnO, which can tune the band gap to lower energy in order to use visible light as a light source instead of UV light. Additionally, RE ion dopants can prevent electron recombination by trapping electrons, thus improving photocatalytic activity.

In this research, we report cerium-oxide-nanoparticle-decorated zinc oxide by using a simple one-pot hydrothermal process. The effects of Ce ion doping on surface morphology and composition and on optical properties were systematically studied. As-prepared cerium-oxide-nanoparticle-decorated zinc oxide was manipulated to evaluate the photodegradation activity of methyl orange (MO) under fluorescent lamp illumination.

## **4.2 Experimental Details**

Zinc nitrate hexahydrate ( $\text{Zn}(\text{NO}_3)_2 \cdot 6\text{H}_2\text{O}$ ) was supplied from Sigma-Aldrich, Korea. Cerium nitrate hexahydrate ( $\text{Ce}(\text{NO}_3)_3 \cdot 6\text{H}_2\text{O}$ ) and sodium hydroxide (NaOH) were obtained from Daejung Chemicals and Metals, Korea. Methyl orange ( $\text{C}_{14}\text{H}_{14}\text{N}_3\text{NaO}_3\text{S}$ ) was supplied by Samchun Pure Chemical, Korea. Deionized water (DI) was utilized for all sample preparations and cleaning processes. All chemicals were used as received without further purification.

#### **4.2.1 Preparation of Ce/ZnO Nanocomposites**

Cerium-oxide-nanoparticle-decorated zinc oxide was synthesized using a simple one-pot hydrothermal technique. Specifically, 3.25 g of zinc nitrate hexahydrate and pre-calculated amounts of 3%, 5%, and 7% Ce ion precursor (named 3%, 5%, 7% Ce/ZnO, respectively) were added in 120 mL of DI water. The mixed solution was stirred at 500 rpm for 20 min. Then, 1 g of NaOH solution (25 mg/mL in DI) was introduced drop-wise into the prepared solution until the pH reached 10 and the color turned into a milky color. Then, the mixed solution was transferred to a 200 mL Teflon-lined stainless steel autoclave and kept for 16 h under 160 °C. Then, samples were collected and washed several times by DI in order to remove unwanted ions. After that, samples were kept at 70 °C for 12 h in order dry.

#### **4.2.2 Material Characterization**

X-ray diffraction was performed to investigate the phase structures of the samples. Field emission scanning electron microscopy and high-resolution transmission electron microscopy were utilized to clarify the morphologies and crystalline structures. An X-ray photoelectron spectrometer was utilized to analyze the surface compositions and chemical states of samples. Optical properties were investigated using a UV-vis spectrometer. A PL spectrometer was used to characterize the charge recombination.

### **4.2.3 Evaluation of Photocatalytic Activity**

The photocatalytic activity was measured by the degradation of methyl orange during light illumination. To assess the adsorption of methyl orange, 10 mg of sample powder was added to 50 mL of 10 ppm methyl orange under magnetic stirring at 500 rpm. After that, the mixed solution was placed in the dark for 20 min in order to provide an adsorption–desorption equilibrium. Then, a fluorescent lamp, used as a light source, was activated to examine the photocatalytic degradation for 1 h. After light illumination, 2 mL of a mixed solution was collected at specified time intervals and was filtered through a polytetrafluoroethylene filter (PTFE, pore size: 0.2  $\mu$ m). Then, the absorption spectra of the collected solution were investigated by UV–visible spectrometry.

## **4.3 Results and Discussion**

### **4.3.1 Surface morphology, surface composition and optical properties**

The XRD patterns of pristine ZnO, CeO<sub>2</sub> [148], and Ce/ZnO samples (3%, 5%, and 7% of Ce ions) are shown in Fig. 18. It can be seen that the XRD pattern of pristine ZnO corresponds to the reflection planes of the wurtzite hexagonal ZnO phase (JCPDS No. 89-13971) [149], while as-synthesized Ce/ZnO samples show additional peaks corresponding to the reflection planes of the cubic-structured CeO<sub>2</sub> (JCPDS No. 34-394) [150]. The lattice constants of ZnO and CeO<sub>2</sub> crystals can be calculated from the X-ray diffraction (XRD) results using a space lattice equation [151], [152]:



Cubic-structured CeO<sub>2</sub>:

$$\frac{1}{d_{hkl}^2} = \frac{1}{a^2}(h^2 + k^2 + l^2). \quad (17)$$

Wurtzite hexagonal ZnO:

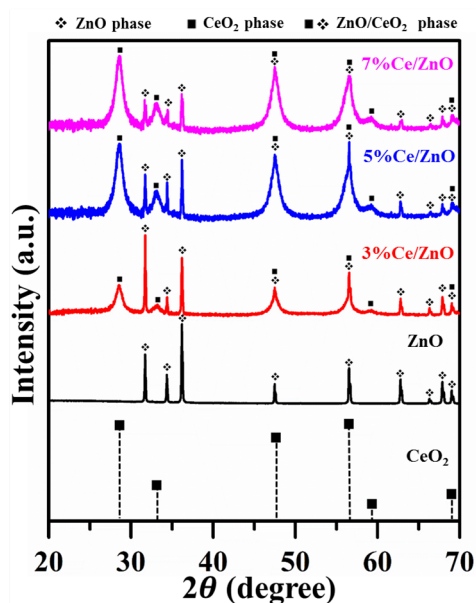
$$\frac{1}{d_{hkl}^2} = \left[ \frac{4}{3}(h^2 + hk + k^2) + l^2 \left( \frac{a}{c} \right)^2 \right] \frac{1}{a^2}, \quad (18)$$

where  $d$  is the spacing between planes of atoms and  $h$ ,  $k$ , and  $l$  are miller indices. Here,  $a$  and  $c$  are the lattice constants of the crystal. The sizes of ZnO and CeO<sub>2</sub> crystals can be calculated by Scherer's equation [153]:

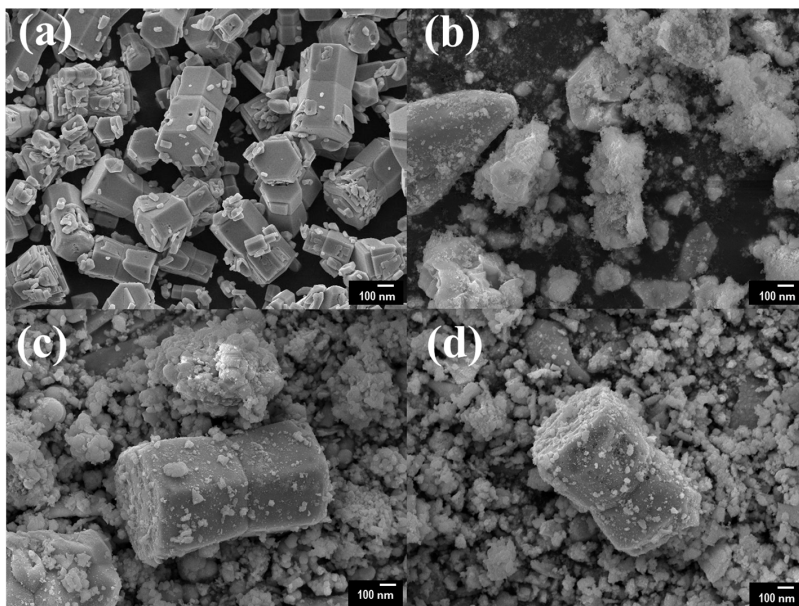
$$t = \left( \frac{\lambda K}{\beta \cos \theta} \right), \quad (19)$$

where  $t$  is average crystal size,  $\lambda$  is the X-ray wavelength,  $K$  is a dimensionless shape factor,  $\beta$  is the broadening at half of the maximum intensity, and  $\theta$  is Bragg's angle. In the XRD results, it is clearly seen that the pristine ZnO sample is more crystalline compared to the as-prepared Ce/ZnO samples. In addition, it can be recognized that the impurity of CeO<sub>2</sub> crystals is exhibited by the broadening peak of CeO<sub>2</sub> crystals. Thus, from the XRD data, we can only determine the crystal size from the ZnO peak (calculated crystal sizes from several reflection planes of pristine ZnO and Ce/ZnO samples are shown in Table 13). The average crystal sizes and lattice constants are summarized in Table 11. As Ce ion doping increased, the intensity of the ZnO reflection plane decreased and became broader, while the intensity of the CeO<sub>2</sub> reflection plane increased. Interestingly, even though the amount of zinc is higher than cerium, the intensity of the ZnO was lower than the intensity of the CeO<sub>2</sub>. This is due to the scattering

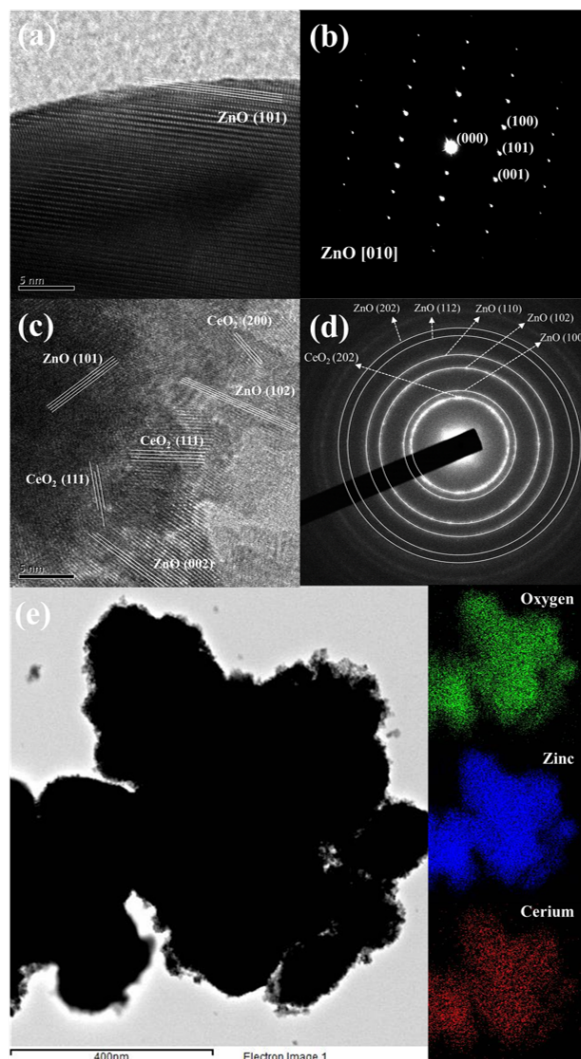
factors of zinc and cerium atoms [154]. That is, the  $\text{Zn}^{2+}$  has a lower scattering factor compared with  $\text{Ce}^{4+}$  in Ce/ZnO samples. The scattering factor ( $f$ ) of an atom is governed by  $\sin(\theta/\lambda)$  ( $\theta$  is the scattering angle and  $\lambda$  is the wavelength of the X-ray) and the atomic number. Therefore, it could be said that heavier atoms can be detected more easily than lighter atoms in the crystal structure. Additionally, it can be seen that the crystal size of Ce/ZnO was reduced compared with that of pristine ZnO. This result agrees with a result obtained by L.L. Lu et al. [155]. Although  $\text{Ce}^{4+}$  has a higher ionic radius compared with  $\text{Zn}^{2+}$ ,  $\text{Ce}^{4+}$  ions possibly move into the ZnO matrix due to the low decomposition temperature of nitrate. Thus,  $\text{Ce}^{4+}$  can enter/intermingle in the ZnO matrix and substitute for the  $\text{Zn}^{2+}$  position to form  $\text{CeO}_2$ .



**Fig. 18:** X-ray diffraction patterns of pristine ZnO, CeO<sub>2</sub> [156], and as-synthesized Ce/ZnO samples.



**Fig. 19:** Field-emission scanning electron microscopy (FE-SEM) images of (a) pristine ZnO, (b) 3% Ce/ZnO, (c) 5% Ce/ZnO, and (d) 7% Ce/ZnO samples.



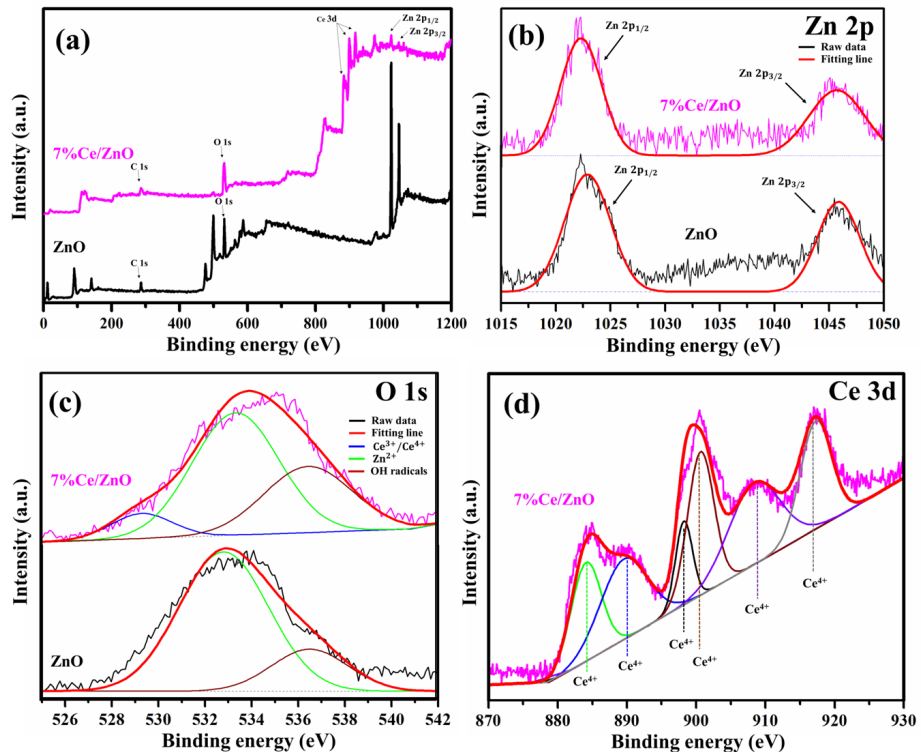
**Fig. 20:** HR-TEM images and SAED patterns of (a,b) pristine ZnO and (c,d) 7% Ce/ZnO nanocomposites; (e) energy dispersive spectroscopy (EDS) mapping of 7% Ce/ZnO samples.

Fig. 19 presents the surface morphology and composition of pristine ZnO and Ce/ZnO samples that were observed by field-emission scanning electron microscopy (FE-SEM). The pristine ZnO has a hexagonal rod-like structure with an average particle size of 432 nm (the Size distribution of pristine ZnO is shown

in Fig. 27). Ce ion doping had no effect on the shape of the Ce/ZnO. However, the average particle size of the Ce/ZnO showed an increase due to the introduction of Ce into the ZnO structure. HR-TEM was performed to gain deep insight into the crystal structure, growth direction, and elemental composition. HR-TEM images and SAED patterns of pristine ZnO and 7% Ce/ZnO are demonstrated in Fig. 20. Based on the HR-TEM of pristine ZnO in Fig. 20(a), the interplanar spacing was measured to be 0.24 nm, corresponding to the (101) reflection plane of a wurtzite hexagonal ZnO structure. Additionally, the SAED pattern further confirmed the structure of pristine ZnO, as shown in Fig. 20(b). HR-TEM images and SAED patterns of ZnO with 7% Ce doping samples (Fig. 20(c)- 20(d)) revealed the presence of ZnO and CeO<sub>2</sub> in Ce/ZnO samples. Energy dispersive spectroscopy (EDS) mapping was also provided, as shown in Fig. 20(e). This strongly indicates the successful doping of Ce into the ZnO matrix.

**Table 11:** Lattice parameters, crystalline sizes, average particle sizes, and optical energy band gaps.

Sample	XRD				FE-SEM Average particle size (nm)	UV-visible $E_g$ (eV), $R^2$
	ZnO			CeO <sub>2</sub>		
	a (Å)	c (Å)	t	a (Å)		
ZnO	3.253	5.211	92.6	-	432	3.06, 0.970
3% Ce/ZnO	3.252	5.211	93.3	5.400	674	2.93, 0.991
5% Ce/ZnO	3.252	5.208	85.3	5.405	695	2.48, 0.990
7% Ce/ZnO	3.251	5.207	86.0	5.405	691	2.22, 0.994



**Fig. 21:** X-ray photoelectron spectroscopy (XPS) spectra of pristine ZnO and 7% Ce/ZnO samples: (a) Survey spectrum and deconvoluted XPS spectrum of (b) Zn 2p, (c) O 1s, and (d) Ce 3d.

The surface compositions and chemical states of pristine ZnO and 7% Ce/ZnO samples were clarified using X-ray photoelectron spectroscopy (XPS) as presented in Fig. 21. The XPS survey (Fig. 21(a)) reveals the respective elements with the corresponding characteristic peaks and compositions (Zn, Ce, O, and C). The summary of the XPS peak positions and the % area of ZnO and 7% Ce/ZnO samples are supplied in Table 14. The deconvoluted Zn 2p peak of pristine ZnO and Ce/ZnO was fitted with two Gaussian peaks corresponding to Zn 2p<sub>1/2</sub> (1022.30 eV) and Zn 2p<sub>3/2</sub> (1045.69 eV), as shown in Fig. 21(b). The deconvoluted O 1s peaks (Fig. 21(c)) show two types of surface oxygen on

pristine ZnO at 533.33 and 536.44 eV, which are associated with  $\text{Zn}^{2+}$  and chemisorbed oxygens (surface hydroxyl groups) [157]. The 7% Ce/ZnO sample shows two peaks, i.e., the same as the pristine ZnO with an additional peak at 529.32 nm, which contributed to  $\text{Ce}^{3+}/\text{Ce}^{4+}$  ion bonding with oxygen due to the introduction of Ce into the ZnO lattice [63]. Fig. 21(d) shows the deconvoluted Ce 3d peaks, which consist of binding energies, representing the integrated peaks of  $\text{Ce}^{4+}$  (884.09, 889.53, 898.21, 900.62, 908.37, and 917.26 eV). No peaks related to  $\text{Ce}^{3+}$  were noted, indicating the existence of  $\text{Ce}^{4+}$  in the ZnO matrix [64]. Along with the XRD results, after Ce doping, the peak intensity of the ZnO crystal decreased and became broadened. It could be pointed out that the introduction of Ce into the ZnO matrix can cause impurity/defect formation.

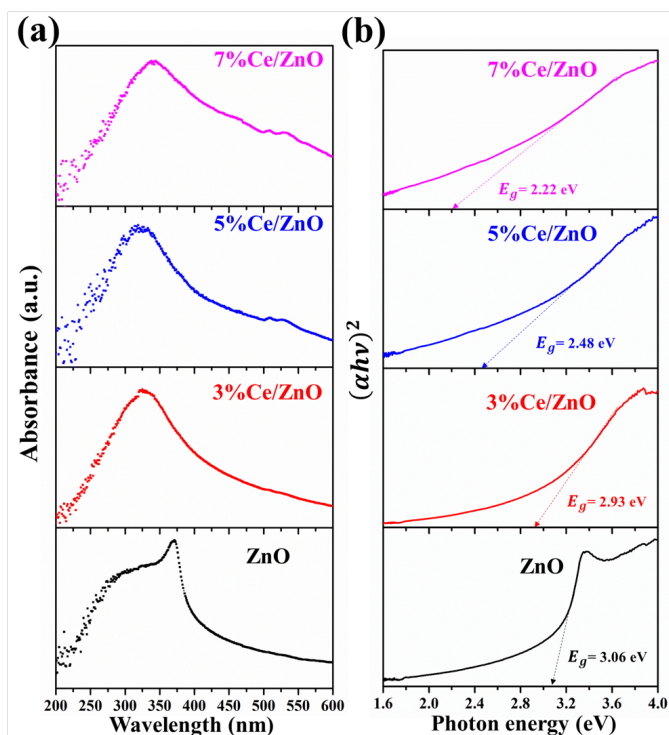


**Fig. 22:** UV-visible spectroscopy of the pristine ZnO and Ce/ZnO samples: (a) Absorption spectra and (b) optical band-gap energy.

The optical properties of the pristine ZnO and Ce/ZnO samples were investigated by UV–visible spectroscopy. Fig. 22(a) exhibits the absorption spectra of as-prepared Ce/ZnO with different % Ce doping. As shown in Fig. 22, the absorption wavelength of pristine ZnO was observed at 365 nm. The absorption wavelength of Ce/ZnO shifted to lower wavelengths with an increase in Ce ion doping. The optical absorption coefficient ( $\alpha$ ) can be calculated as follows [149], [156], [158]:

$$(\alpha h\nu)^2 = D(h\nu - E_g), \quad (20)$$

where  $D$  is a constant which is called the band-tailing parameter,  $h\nu$  is the photon energy, and  $E_g$  is the energy band gap. According to Eq. (20), the energy band gap of as-prepared materials was calculated by conventional extrapolation of the plot of  $\alpha h\nu^2$  and  $h\nu$  at  $\alpha = 0$ , as shown in Fig. 22(b). The calculated energy band gaps of the pristine ZnO and Ce/ZnO samples are summarized in Table 11. It can be seen that the optical energy band gap of Ce/ZnO samples decreased with an increase in Ce ion doping from 3.06 eV (ZnO) to 2.22 eV (7% Ce/ZnO). This indicates that the Ce ion doping helps to tune a narrower optical energy band gap of Ce/ZnO compared to that of pristine ZnO, which tends to be beneficial for photocatalytic activity improvement.

Photoluminescence (PL) spectra were studied with the excitation wavelength of 325 nm at room temperature. As shown in Fig. 23, the PL spectra of the pristine ZnO and Ce/ZnO samples show an emission peak in the UV region of 387 nm, accompanied by two weaker peaks at 443 and 489 nm. The UV emission can be attributed to the band-to-band radiation of pristine ZnO, which is responsible for photogenerated electron–hole recombination. Two



weaker broad emission peaks, which are located in the visible region from 425 to 500 nm, correspond to impurities in the ZnO structure, such as oxygen vacancies and interstitial oxygen [149]. However, luminescent quenching of the Ce/ZnO samples was observed in the order of 7% Ce/ZnO, 5% Ce/ZnO, 3% Ce/ZnO, and pristine ZnO. This suggests that an increase in Ce ion doping can reduce charge carrier recombination. Regarding the results, the decreasing charge recombination could be caused by the existence of more defects/oxygen vacancies and the heterojunction between CeO<sub>2</sub> and ZnO.

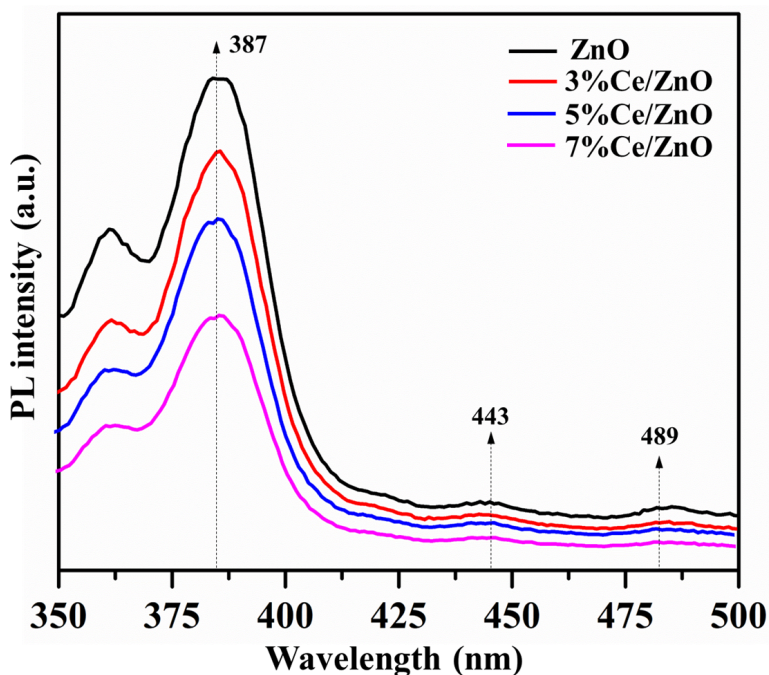


**Fig. 23:** The photoluminescence spectra of the pristine ZnO and Ce/ZnO samples.

### 4.3.2 Photocatalytic Activity Studies

The photocatalytic activities of the pristine ZnO and Ce/ZnO catalysts were evaluated in terms of the degradation of MO under a fluorescent lamp. The fluorescent lamp as a light source contributes to the UV and visible light emissions, as shown in Fig. 28. The overlapping area between fluorescent lamp emission and MO absorption was expected to provide photons for photocatalytic reactions. MO degradation was measured by observing the change in the adsorption spectra of MO at 464 nm, as shown in Fig. 24. The percentage of MO photodegradation was calculated using the formula [59];

$$\%Photodegradation = [(A_0 - A_t)/A_0] \times 100, \quad (21)$$

where  $A_0$  and  $A_t$  are the initial and final absorbances of MO, respectively. The percentage of MO photodegradation with different Ce ion doping was calculated and tabulated in Table 12. Photocatalysts based on Ce/ZnO showed higher photocatalytic activity, which can degrade 94.06% of MO after 60 min. In contrast, the photocatalysts based on pristine ZnO can degrade 69.42% of MO. The results suggest an improvement of MO photocatalytic degradation due to an increase in Ce ion doping.

The mechanism and effectiveness of photodegradation of MO was studied through the kinetic adsorption. Fig. 25 exhibits the variation in absorption of the MO solution with the presence of the pristine ZnO and Ce/ZnO samples as a function of illumination time, which was fitted to the first- and second-order kinetic adsorption models, as given by:

First-order kinetic adsorption model:

$$\ln C_t = \ln C_0 - k_1 t. \quad (22)$$

Second-order kinetic adsorption model:

$$\frac{1}{C_t} = \frac{1}{C_0} + k_2 t, \quad (23)$$

where  $C_t$  and  $C_0$  are the final and initial absorptions of MO under fluorescent lamp illumination, respectively;  $k_1$  and  $k_2$  are the first- and second-order kinetic reaction rate constants;  $t$  is the fluorescent lamp illumination time. The summary of the calculated  $k_1$ ,  $k_2$ ,  $R_1^2$ , and  $R_2^2$  was tabulated, as shown in Table 12. It can be seen that the correlation coefficient of the first-order kinetic adsorption model showed a lower value compared with that of the second-order kinetic adsorption model. This indicates that the second-order kinetic model is more suitable and applicable for predicting a kinetic adsorption of photocatalysts in the presence of MO (Table 12). Variations in the reaction rate values indicate that an increase in Ce ion doping in Ce/ZnO catalysts improves the photodegradation reaction. The comparison of photocatalytic MO degradation activity based on Ce/ZnO catalysts is summarized in Table 15. Compared with other reports, our Ce/ZnO catalyst showed a higher photocatalytic activity performance and faster degradation time with 7% cerium.

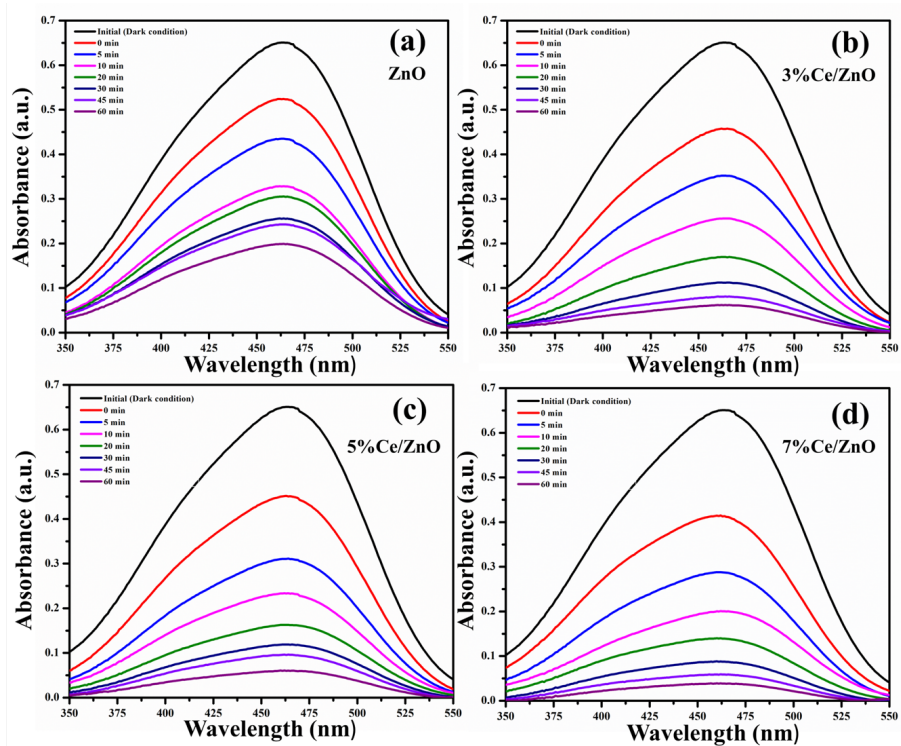


**Fig. 24:** Change in absorption spectra of the (a) pristine ZnO, (b) 3% Ce/ZnO, (c) 5% Ce/ZnO, and (d) 7% Ce/ZnO catalysts during photodegradation of methyl orange.

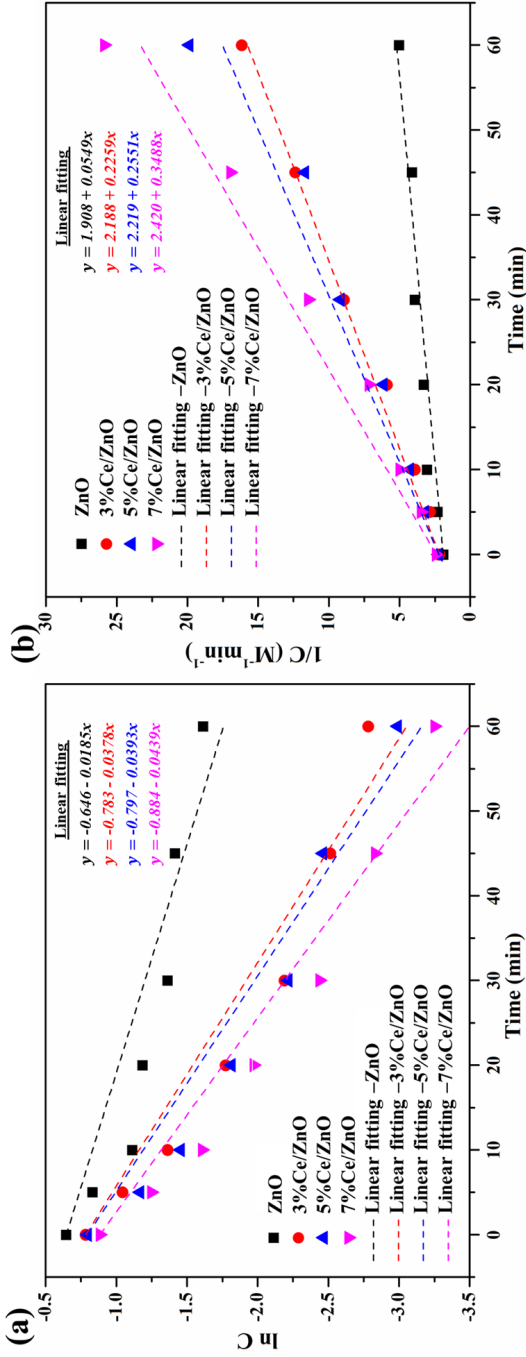


**Fig. 25:** (a) First- and (b) second-order kinetic adsorption curves of the pristine ZnO and Ce/ZnO catalysts during photodegradation of methyl orange.

A possible photocatalytic degradation mechanism of the Ce/ZnO catalysts is displayed in Fig. 26. The band-edge positions of the conduction ( $E_{CB}$ ) and valence band ( $E_{VB}$ ) of metal-oxide semiconductors can be calculated using the equations [64]:

$$E_{CB} = X - E_c - 0.5 \times E_g \quad (24)$$

$$E_{VB} = E_g - E_{CB}, \quad (25)$$

where  $X$  is the electronegativity of ZnO and CeO<sub>2</sub> (5.79 for ZnO and 5.56 eV for CeO<sub>2</sub>),  $E_c$  is the free electron energy on the hydrogen electrode scale (4.5 eV), and  $E_g$  is the band-gap energy (3.18 for ZnO and 3.00 eV for CeO<sub>2</sub>). According to the conduction and valence band equations, the calculated  $E_{CB}$  and  $E_{VB}$  of ZnO were located at  $-0.30$  and  $2.88$  eV. In contrast, the calculated  $E_{CB}$  and  $E_{VB}$  of CeO<sub>2</sub> were located at  $-0.44$  and  $2.56$  eV. A CeO<sub>2</sub>/ZnO heterojunction forms due to the band-edge potentials between ZnO and CeO<sub>2</sub>, which is beneficial for photocatalytic activity in terms of preventing charge recombination. Additionally, some Ce<sup>4+</sup> ions may have drifted to the surface of the ZnO, which can promote more trapped electrons by the reaction  $\text{Ce}^{4+} + \text{e}^- \rightarrow \text{Ce}^{3+}$ . The product of this reaction can react with oxygen molecules to form superoxide radicals by the reaction  $\text{Ce}^{3+} + \text{O}_2 \rightarrow \text{Ce}^{4+} + \text{O}_2^{*-}$ . The generated radicals (superoxide radicals and hydroxyl radicals) then degrade MO and produce oxidized organic products. As a result, it can be seen that an increase in Ce ion doping can improve the photodegradation reaction rate compared with pristine ZnO. We can draw a conclusion that Ce ion doping in Ce/ZnO plays an important role in providing narrower optical energy band-gap tunability and defect generation, such as oxygen vacancies and oxygen interstitials, which controls photocatalytic activity. Additionally, the CeO<sub>2</sub>/ZnO heterojunction would

provide a carrier pathway to separate photogenerated electron-hole pairs, obstructing charge recombination in Ce/ZnO.

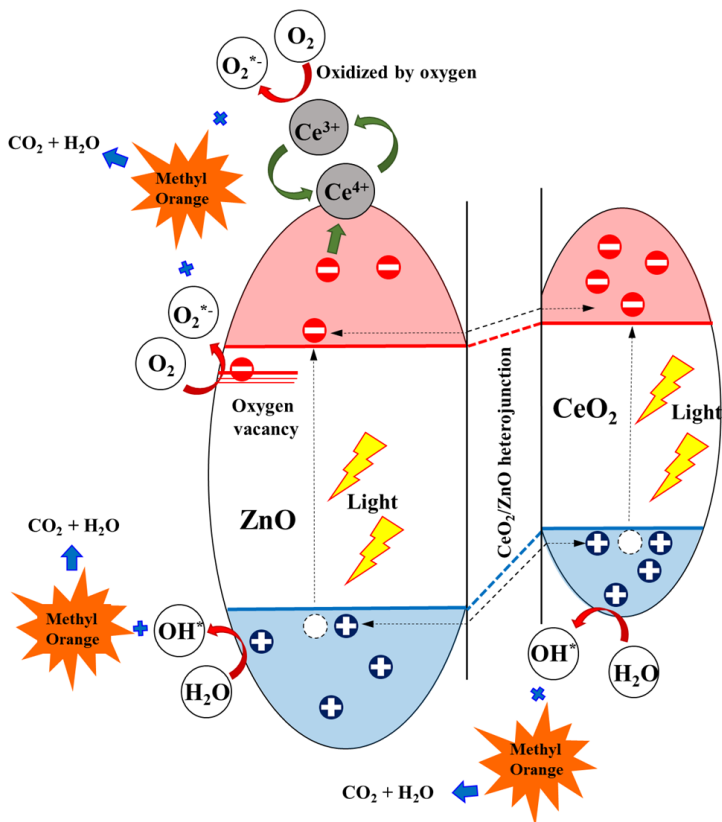


**Fig. 26:** Electron trapping and charge transfer for methyl orange (MO) degradation using the Ce/ZnO catalysts.

**Table 12:** Summary of the first- and second-order kinetic adsorption rate constants and correlation coefficients of photocatalytic degradation of methyl orange based on the pristine ZnO and Ce/ZnO catalysts.

Sample	Photocatalytic Activity				MO Degradation (%) in 1 h
	$k_1$	$R_1^2$	$k_2$	$R_2^2$	
ZnO	0.019	0.981	0.055	0.991	69.42
3%Ce/ZnO	0.038	0.988	0.226	0.991	90.43
5%Ce/ZnO	0.040	0.989	0.255	0.991	92.61
7%Ce/ZnO	0.044	0.990	0.349	0.992	94.06

#### 4.4 Conclusions

Briefly, a simple one-pot hydrothermal technique was utilized to prepare cerium-oxide- nanoparticle-decorated zinc oxide for photocatalytic application. It was found that an increase in Ce doping does not affect the morphology of Ce/ZnO, which remains unchanged in comparison with the hexagonal wurtzite structures of pristine ZnO. XRD and XPS analyses revealed the existence of a cubic CeO<sub>2</sub> phase and Ce<sup>4+</sup> ions in Ce-doped ZnO composite samples. Additionally, an increase in Ce doping in ZnO results in narrower optical energy band tunability and reduced charge recombination. When compared with pristine ZnO, the Ce/ZnO catalysts showed superior photocatalytic degradation of methyl orange, which increased from 69.42% (ZnO) to 94.06% (7% Ce/ZnO) under a fluorescent lamp illumination time of 60 min. This may be due to the Ce<sup>4+</sup> ions, which can trap more electrons, resulting in an increase in generated radicals. Moreover, CeO<sub>2</sub>/ZnO heterojunctions were formed, which provide a carrier pathway to obstruct charge recombination and improve the photocatalytic degradation performance. Thus, cerium-oxide-nanoparticle-decorated zinc oxide



has great potential as a material for water decontamination applications due to its simple synthesis, low-cost materials, and superior photocatalytic degradation performance.

## 4.5 Supporting informations

### Chemical materials

- Zinc nitrate hexahydrate was purchased from Sigma-Aldrich, Korea (Gyeonggi, South Korea)
- Cerium nitrate hexahydrate was obtained from Daejung Chemicals Metals (Gyeonggi, South Korea)
- Sodium hydroxide was obtained from Daejung Chemicals Metals (Gyeonggi, South Korea)
- Methyl orange was supplied by Samchun pure chemical (Gyeonggi, South Korea).

### Characterization instruments

- XRD (Rigaku D/MAZX 2500V/PC model, Tokyo, Japan)
- FE-SEM (JEOL-JSM-7600F, Tokyo, Japan)
- HR-TEM (JEM-2100F-JEOL, Japan)
- XPS (Thermo Fisher Scientific Co., USA)
- UV-visible spectrometer (Spectra Max Plus 384, Molecular Devices, USA)
- PL spectrometer (473 nm diode laser; G9800A; Agilent Technologies, Santa Clara, CA, USA)

- Fluorescent lamp as a light source (EL20W; OSRAM dulux superstar)
- \*\* The emission spectrum of fluorescent lamp was shown in Figure 28

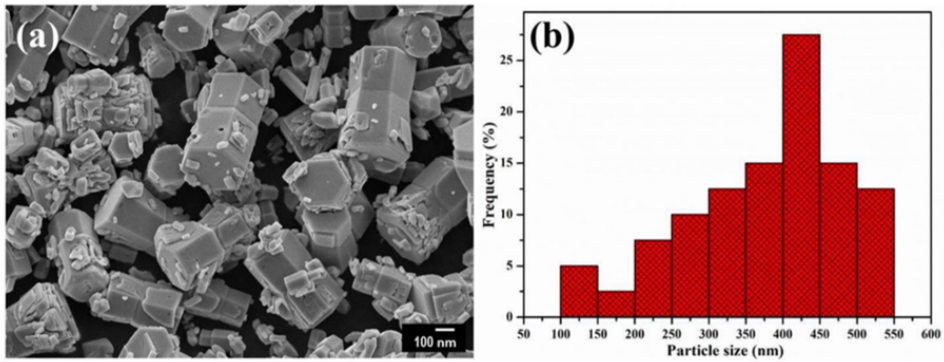


**Fig. 27:** FE-SEM image and size distribution of pristine ZnO.

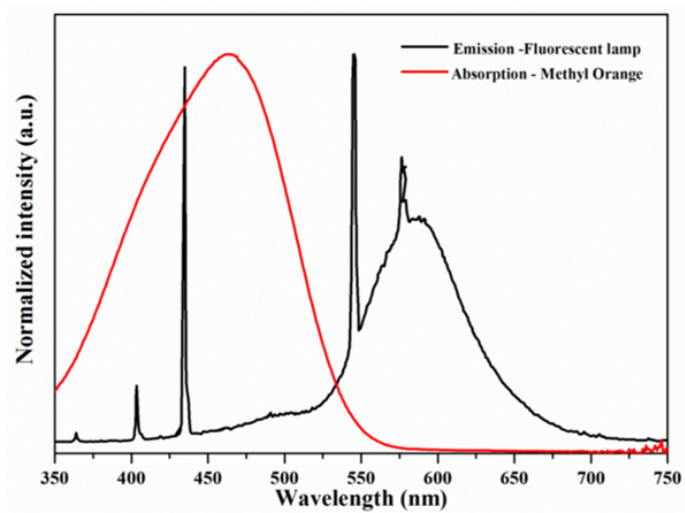


**Fig. 28:** The emission spectrum of fluorescent lamp (compact fluorescent lamp) and absorption spectrum of MO.

**Table 13:** Calculated crystal size from several reflection planes of pristine ZnO and Ce/ZnO samples.

Sample	Crystal size from ZnO reflection plan (nm)					Average crystal size (nm)
	(100)	(002)	(101)	(103)	(200)	
ZnO	95.9	94.2	94.9	92.9	85.1	92.6
3%Ce/ZnO	94.9	142.4	67.0	79.6	82.7	93.3
5%Ce/ZnO	58.3	94.0	110.9	82.7	80.5	85.3
7%Ce/ZnO	64.8	92.5	108.9	83.8	80.1	86.0

**Table 14:** XPS peak position and %area of ZnO and 7%Ce/ZnO nanocomposites.

Elemental composition		ZnO		7%Ce/ZnO	
		Peak position (eV)	%Area	Peak position (eV)	%Area
Zn 2p	Zn 2p <sub>1/2</sub>	1022.9	58.5	1022.3	52
	Zn 2p <sub>3/2</sub>	1045.9	41.5	1045.7	43
O 1s	Ce <sup>3+</sup> /Ce <sup>4+</sup>	-	-	529.3	8.5
	Zn <sup>2+</sup>	532.8	79.5	533.3	59
	OH radicals	536.5	20.5	536.4	32.5
Ce 3d	Ce <sup>4+</sup> :V <sub>0</sub>	-	-	884.1	15.2
	Ce <sup>4+</sup> :V <sub>2</sub>	-	-	889.5	19.4
	Ce <sup>4+</sup> :V <sub>3</sub>	-	-	898.2	7.3
	Ce <sup>4+</sup> :U <sub>0</sub>	-	-	900.6	19.4
	Ce <sup>4+</sup> :U <sub>2</sub>	-	-	908.4	21.5
	Ce <sup>4+</sup> :U <sub>3</sub>	-	-	917.3	17.2

**Table 15:** The comparison of photocatalytic MO degradation activity based on Ce/ZnO catalysts.

Sample	Synthesis technique	Light source	MO degradation (%)	Light illumination time (min)	Reaction rate constant ( $\text{min}^{-1}$ )	R <sup>2</sup>	Ref
7%Ce/ZnO	Solvothermal	Solar simulator	95	80	0.043	-	[159]
0.5%Ce/ZnO	Hydrothermal	Visible light	64	-	0.018	-	[160]
3%Ce/ZnO	Chemical-precipitation	UV lamp	84	60	-	-	[161]
9%Ce/ZnO	Chemical-precipitation VS technique-	-	30	60	0.007	-	[162]
10%Ce/ZnO	Thermal evaporation	Visible light	95.9	150	0.001	-	[163]
7%Ce/ZnO	Hydrothermal	Fluorescent lamp	94.6	60	0.044	0.990	This work

## **5 Surface Charge Modification of ZnO Nanoparticles Using Aniline with Improved Photodegradation Performance**

### **5.1 Introduction**

In this chapter, we present the surface modification of ZnO by using Specific charge and polar molecule functionalization. The photocatalytic activity of materials is mostly dependent on their surface properties such as particle size, crystalline phase, surface defects, and surface charge [164]–[166]. To improve surface adsorption and charge transfer, many studies have been done on surface modifications using metal/non-metal doping and polar molecule functionalization [41], [51]–[53], [167], [168]. Renquan Guan, et al synthesized ZnO/graphitic carbon nitride (g-C<sub>3</sub>N<sub>4</sub>) composites, which improve photocatalytic activity by increasing the charge carrier and hindering charge recombination [169]. Debasrita Dash, et al prepared europium (Eu)-doped ZnO nanoparticles, which have a higher surface area compared to pristine ZnO. Additionally, introducing Eu into ZnO, generates a defect state, which traps photogenerated electron-hole pairs, resulting in the improvement of photocatalytic efficiency [170]. Specific charge and polar molecule functionalization of a material surface is an attractive technique that capably enhances dye adsorption on the material surface [167], [168]. Hyunwoong Park, et al reported nafion (an anionic perfluorinated polymer) functionalized on titanium dioxide (TiO<sub>2</sub>) which modifies the surface charge and enhances the photocatalytic degradation of the cationic dye by opposite charge-induced adsorption and an increase in electron injection [168].

However, aniline-functionalized ZnO based on photocatalytic dye degradation has not yet been reported.

In this study, we present a simple synthesis of ZnO via a hydrothermal technique, followed by tailoring of its surface charge using aniline, and systematically characterizing and investigating MO photodegradation. Compared to pristine ZnO, aniline-functionalized ZnO showed a higher photodegradation performance.

## **5.2 Experimental Details**

Chemical precursors and characterization equipment information are provided in supplementary detail section. Deionized water (DI) was used to prepare and clean sample. All chemicals were utilized in a sample synthesis process as received without any further purification.

### **5.2.1 Preparation of ZnO Nanoparticles**

ZnO nanoparticles were simply synthesized using hydrothermal technique as previously described. Briefly, 0.4M of zinc acetate was dissolved in 170 ml of deionized (DI) water while stirring. A sodium hydroxide solution was separately prepared and added dropwise into as-prepared zinc solution to a pH of 10. Next, this mixture was transferred to a Teflon-lined stainless steel autoclave and heated to 180°C for 12 hr. The sample was collected by filtration, wash with DI water several times to remove unwanted ions, and dried at 70°C for 24 h (referred to ZnO).

### **5.2.2 Functionalization of aniline on ZnO nanoparticles**

Aniline solution was prepared by mixing a pre-calculated amount of aniline (1, 2 and 3 mole/L) with an ethanol/DI (4:1) solution with stirring for 30 min. To functionalize aniline onto ZnO, 0.5 g of prepared ZnO nanoparticles was immersed in the aniline solution and stirred for 12 h. Finally, aniline-functionalized samples were purified by dialysis using DI water, collected by filtration and dried in oven at 70°C for 24 h. The samples were named by ZnO/An1, ZnO/An2 and ZnO/An3, respectively.

### **5.2.3 Material Characterization**

Field-emission scanning electron microscopy and high-resolution transmission electron microscopy were utilized to clarify the surface morphology and crystalline structures. X-ray diffraction was performed to characterize the phase structures of the samples. Fourier transform infrared spectroscopy and X-ray photoelectron spectrometer were utilized to investigate the functional groups and chemical valence states of the samples. The optical properties were studied using UV-vis diffuse reflectance spectrometry. The Zetasizer equipment was utilized to investigate an average particle size and surface charge (zeta potential- $\zeta$ ).

### **5.2.4 Evaluation of Photocatalytic Activity**

For the photocatalytic study, 10 mg of as-synthesized samples was dispersed into 50 mL of methyl orange (MO) solution (10 ppm in DI water) with stirring (500 rpm). The mixed solution was placed in a dark box for 20 min to provide an



adsorption-desorption equilibrium. Then, Fluorescent lamp, as a light source, was activated to investigate the photocatalytic degradation of MO for 30 min. The photocatalytic activity was monitored using a UV-visible spectrometer, measuring decreases in the MO absorption peak (at 464 nm) at specific time intervals.

## **5.3 Results and Discussions**

### **5.3.1 Surface morphology and crystalline structure studies**

Figure 29(a)-29(d) shows FE-SEM and HR-TEM image of ZnO and aniline-functionalized ZnO. It can be seen that the surface morphology of ZnO sample was composed of nanorods and nanoparticles while functionalized ZnO sample also showed a similar particle shape. Zetasizer was utilized to determine the average particle size of all samples which is summarized as shown in Table 16. It was found that all of samples show small changing of average particle size after functionalized aniline.

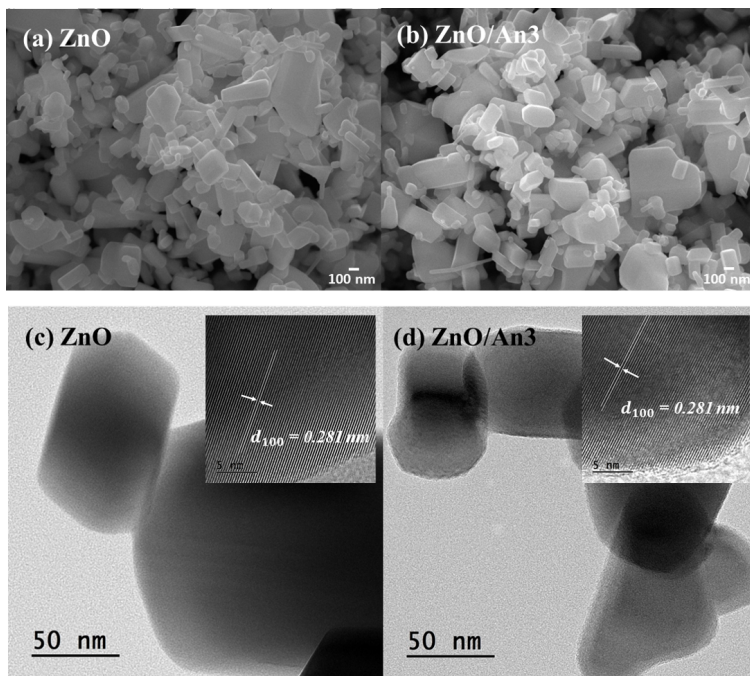


**Fig. 29:** FE-SEM and HR-TEM images of ZnO and functionalized ZnO samples.

**Table 16:** Summaries of crystal information, and surface charge.

Sample	XRD		Zetasizer Nano ZS		
	Lattice constant		Crystal size (nm)	Average size (nm)	Zeta potential (mV)
	a (Å)	c (Å)			
ZnO	3.25	5.21	91.6	232.1	18.24
ZnO/An1	3.25	5.21	87.5	250.9	20.34
ZnO/An2	3.25	5.21	90.1	253.3	23.48
ZnO/An3	3.25	5.21	86.8	246.2	25.54

XRD patterns of samples are shown in Figure 30. It can be seen that the diffraction peaks of all samples exhibit a prominent peak at  $31.7^\circ$  (100),  $34.4^\circ$  (002),  $36.2^\circ$  (101),  $47.5^\circ$  (102),  $56.5^\circ$  (110),  $62.8^\circ$  (103),  $66.3^\circ$  (200),  $67.9^\circ$  (112),  $69.0^\circ$  (201),  $72.5^\circ$  (004),  $76.9^\circ$  (202) corresponding to hexagonal ZnO wurtzite structure (JCPDS card of 89-13971) [171]. No diffraction peaks corresponding to

aniline, were observed in any samples. The lattice constants ( $a$  and  $c$ ) of samples can be calculated using following hexagonal space lattice formula [149];

$$\frac{1}{d_{hkl}^2} = \left(\frac{4}{3}\right)\left(\frac{h^2 + hk + k^2}{a^2}\right) + \left(\frac{l^2}{c^2}\right), \quad (26)$$

where  $d_{hkl}$  is the lattice spacing,  $h$ ,  $k$ , and  $l$  are miller indices. The average crystal size ( $t$ ) of samples was calculated using Scherer's equation [149];

$$t = \left(\frac{0.9\lambda}{\beta \cos\theta}\right), \quad (27)$$

where  $\lambda$  is the X-ray wavelength,  $\beta$  is the corrected full width at half maximum (FWHM), and  $\theta$  is the Bragg's angle. The crystal information is summarized in Table 16. There were small changes in average crystal size and particle size after aniline was functionalized on ZnO. However, aniline functionalization did not affect to the morphology and the lattice constant of ZnO.

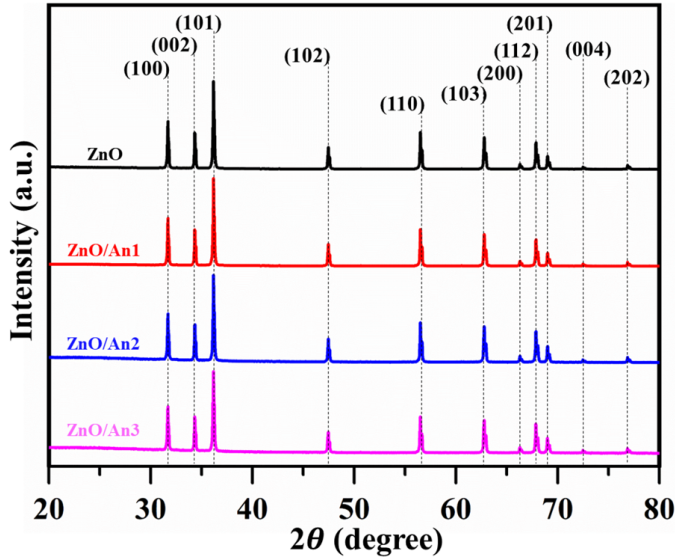


**Fig. 30:** XRD patterns of ZnO and functionalized ZnO samples.

### 5.3.2 Surface composition analysis

Figure 31(a) shows FT-IR of samples which exhibits broad IR band around  $3300\text{-}3600\text{ cm}^{-1}$  and  $400\text{-}600\text{ cm}^{-1}$  corresponding to stretching vibration of OH and Zn-O, respectively. In addition, prominent peak around  $900\text{-}1200\text{ cm}^{-1}$  attributed to carboxyl C-O and alkoxy C-O stretching was observed. It is clearly seen that functionalized ZnO samples show additional peaks at  $1384.2\text{ cm}^{-1}$  and  $1632.2\text{ cm}^{-1}$  which are attributed to C-N stretching and N-H bend (primary amine) vibrational mode [172], respectively (Figure 31(b)-31(c)). This indicates to the existence of aniline molecule on ZnO surface.

ZnO and functionalized ZnO samples were subjected to study their surface chemical composition using a X-ray photoelectron spectrometer as shown in Figure 32. Figure 32(a) exhibits the XPS survey spectra of ZnO and ZnO/An3 with the presence of C, O, N and Zn elements. The deconvoluted XPS of N 1s peak was shown in Figure 32(b). Compared to pristine ZnO samples, functionalized ZnO samples reveals the C-N peak at  $399.81\text{ eV}$  and C-NH<sub>3</sub><sup>+</sup> peak at  $401.72\text{ eV}$  which confirms the existence of aniline on ZnO surface [172]. Additionally, XPS peak shifting of Zn 2p was observed after aniline functionalization as shown in Figure 32(c), consisting of Zn 2p<sub>1/2</sub> from  $1022.28\text{ eV}$  (ZnO) to  $1022.48\text{ eV}$  (ZnO/An3) and Zn 2p<sub>3/2</sub> from  $1045.38\text{ eV}$  (ZnO) to  $1045.58\text{ eV}$  (ZnO/An3). This indicates to the chemical interaction between aniline molecules and Zn surface. Along with FT-IR, this is a good agreement to confirm the successful aniline molecule functionalization on ZnO surface.

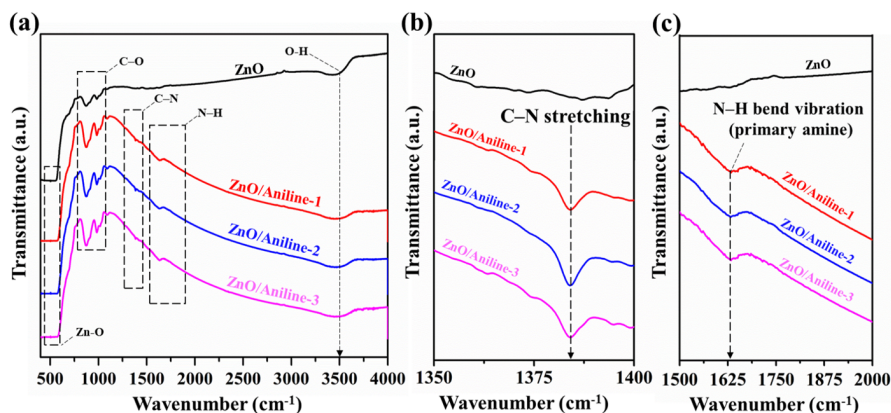


**Fig. 31:** FT-IR of ZnO and functionalized ZnO samples; (a) 400-4000  $\text{cm}^{-1}$ , (b) C-N stretching region: 1350-1400  $\text{cm}^{-1}$ , and (c) N-H bend vibrational region: 1500-2000  $\text{cm}^{-1}$ .

The above surface modification using aniline on ZnO surface can be further studied by measuring zeta potential ( $\zeta$ ) as tabulated in Table 16. After aniline functionalization, the zeta potential ( $\zeta$ ) of samples was increased from 18.24 mV (ZnO) to 25.54 mV (ZnO/An3). It can be ascribed that the surface charge modification using aniline directly manipulates to the electrostatic interaction between positively charged aniline and ZnO, resulting to the protonation reaction of positively charged-aniline molecules on ZnO surface and increase in zeta potential value.

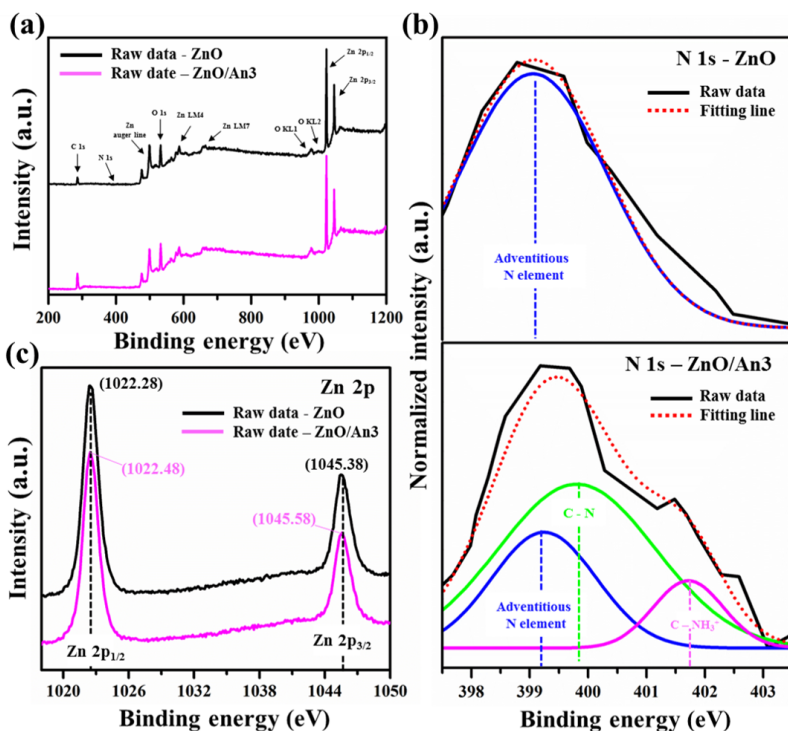


**Fig. 32:** XPS of ZnO and ZnO/An3 samples; (a) XPS Survey spectrum, (b) deconvoluted XPS N 1s and (c) XPS Zn 2p.

### 5.3.3 Optical property studies

Optical properties were characterized by using UV-vis diffuse reflectance spectrometer as shown in Figure 33. UV-vis (DRS) spectra of functionalized ZnO samples show a hypsochromic shift as that of surface chemical interaction between aniline molecule and ZnO. The optical band gap ( $E_g$ ) samples were determined from reflective spectra using the Kubelka–Munk function as given by [173]

$$(F(R)hv) = A(hv - E_g)^{\frac{1}{2}} \quad (28)$$

where  $F(R) = (1-R)^2/2R$  and  $R$  is the reflectance. According to Equation 26, the band gap of materials has been calculated by conventional extrapolation of the plot of  $(F(R))^2$  and  $h\nu$  at  $F(R) = 0$ , as shown in inset of Figure 33. The small shift in the energy band gap was observed and expected to enhance the photogenerated electron/hole pairs efficiency and photocatalytic performance. The calculated optical energy band gap was summarized in Table 17.

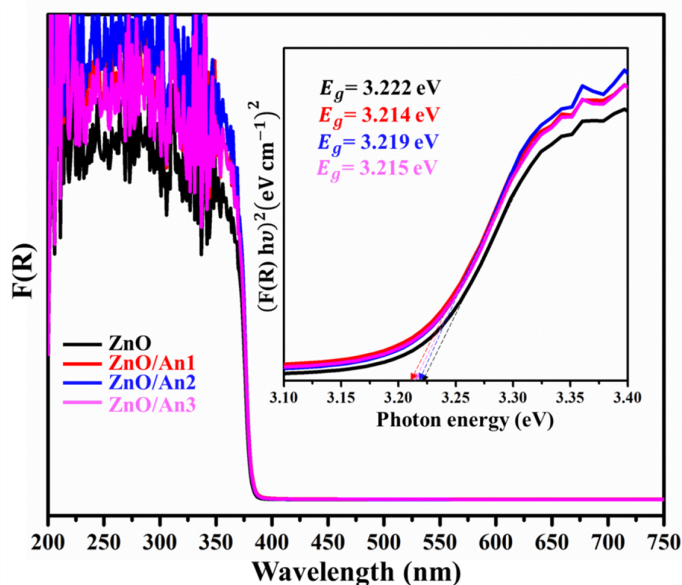


**Fig. 33:** UV-vis spectra of ZnO and functionalized ZnO samples; (inset) optical energy band gap.

### 5.3.4 Photocatalytic activity of aniline functionalized ZnO

Photocatalytic performance of samples under fluorescent lamp is demonstrated as a function of absorption peak and wavelength with different illumination time of 0, 5, 10, 20, 30, 45, and 60 min, as shown in Figure 35. The absorption region of MO was observed at 464 nm. The photocatalytic degradation of MO, was calculated

as the following equation [174];

$$\%Degradation = \left( \frac{A_0 - A_t}{A_0} \right) \times 100, \quad (29)$$

where  $A_0$  and  $A_t$  is the absorbances of MO a initial time and after irradiation at  $t$  min. The calculated %degradation of samples was summarized in Table 17 and the variation in the absorption band of MO solution with the presence of ZnO and aniline functionalized ZnO samples as a function of illumination time, was exhibited in Figure 34(a). It can be seen that an increase in aniline functionalization can intensively improve photocatalytic degradation ability of ZnO. An increase in aniline concentration on functionalized ZnO increased MO degradation from 39.96% (ZnO) to 98.29% (ZnO/An3) in 60 min. Photocatalytic activity of MO degradation is studie though the first order kinetic adsorption,as following [175], [176]

$$\ln \left( \frac{c_t}{c_0} \right) = -k_c t, \quad (30)$$

where  $c_0$  and  $c_t$  are the concentration of MO solution before and after light illumination,  $t$  is light illumination time, and  $k_c$  is the photocatalytic reaction rate constant (slope in Figure 34(b)). This revealed that an increase in aniline concentration in ZnO improved photocatalytic reaction rate constant ( $k_c$ ) from  $0.008 \text{ min}^{-1}$  (ZnO) to  $0.066 \text{ min}^{-1}$  (ZnO/An3). This was due to an aniline molecule( $\text{C}_6\text{H}_5\text{-NH}_3^+$ ) working as the active site to protonate on ZnO surface, that could easily absorb and decompose MO (anionic dye). Our results revealed that aniline (as positive charge) modified on ZnO surface effectively improve surface adsorption of MO. Upon light illumination, photogenerated radicals



(superoxide and hydroxyl radicals) could oxidize and mineralize MO to green products faster compared to pristine ZnO.

**Table 17:** Optical energy band gap and photocatalytic performance.

Sample	UV-visible	Photocatalytic performance		
	$E_g$ (eV)	MO degradation	$k_c$ ( $\text{min}^{-1}$ )	$R^2$
ZnO	3.222	39.96%	0.008	0.9516
ZnO/An1	3.214	74.09%	0.021	0.9635
ZnO/An2	3.219	96.63%	0.054	0.9948
ZnO/An3	3.215	98.29%	0.066	0.9975

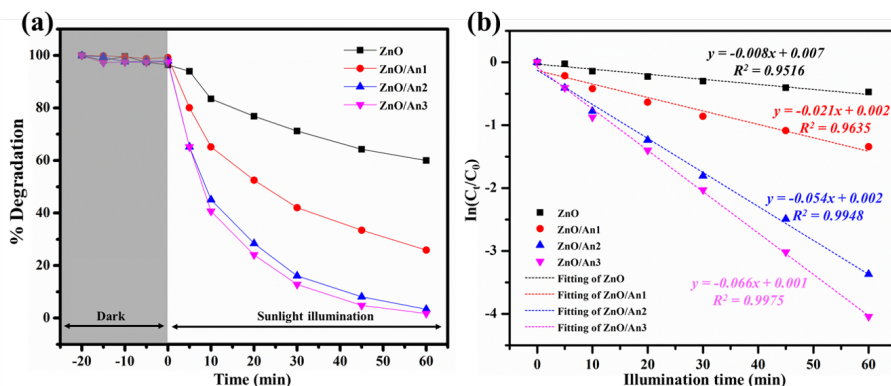


**Fig. 34:** (a) Photodegradation percentage, and (b) kinetic adsorption curves during MO photodegradation of ZnO and functionalized ZnO samples.

## 5.4 Conclusions

Aniline molecules were attached onto ZnO surface by using impregnation technique. Aniline acted as a positive charge modifier on ZnO surface. This modified ZnO showed promising improvement for MO dye adsorption by enhancing the electrostatic interaction between positive aniline functionalized ZnO and negative MO molecules. The photocatalytic degradation of MO was

observed over 98%, faster than ZnO in an hour. The acceleration in photocatalytic degradation suggested that aniline functionalization could be viable option to modify surface charge and improve photocatalytic performance for advance materials.

## 5.5 Supporting informations

### Chemical materials

- Zinc nitrate hexahydrate was purchased from Sigma-Aldrich, Korea (Gyeonggi, South Korea)
- Sodium hydroxide was obtained from Daejung Chemicals Metals (Gyeonggi, South Korea)
- Aniline was from Sigma-Aldrich, Korea (Gyeonggi, South Korea).
- Methyl orange was supplied by Samchun pure chemical (Gyeonggi, South Korea).

### Characterization instruments

- Field-emission scanning electron microscopy (FE-SEM, JEOL-JSM-7600F, Tokyo, Japan)
- High-resolution transmission electron microscopy (HR-TEM, JEM-2100F-JEOL, Tokyo, Japan)
- X-ray diffraction (XRD, Rigaku D/MAZX 2500V/PC model, Tokyo, Japan)
- Fourier transform infrared spectroscopy (FT-IR, Thermo Electron Co., USA)
- X-ray photoelectron spectrometer (XPS, Thermo Fisher Scientific Co., USA)
- UV-vis diffuse reflectance spectrometer (UV-vis DRS, Spectra Max Plus 384, Molecular Devices, USA)

- Zeta potential analyzer (Zetasizer Nano ZS, MALVERN, USA)
- Fluorescent lamp as a light source (EL20W; OSRAM dulux superstar)

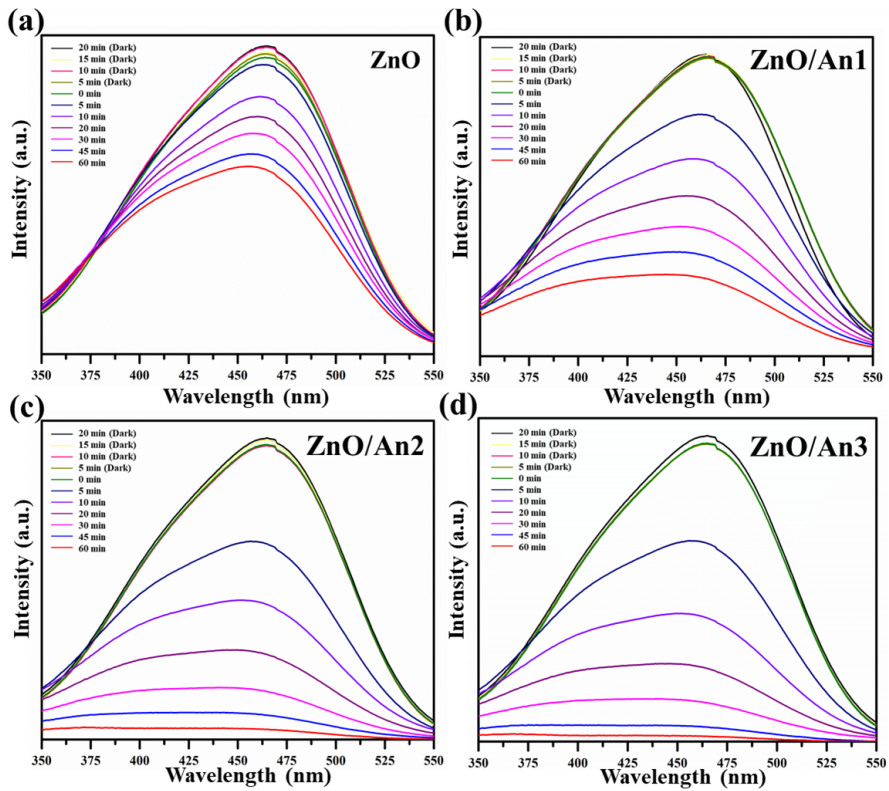


**Fig. 35:** Change in absorption spectra of the (a) pristine ZnO, (b) ZnO/An1, (c) ZnO/An2, and (d) ZnO/An3 catalysts during photodegradation of MO.

## 6 Conclusions

In summary, the photocatalytic degradation property of materials is mostly dependent on their surface properties such as particle size, crystalline phase, surface defects, and surface charge. This research is based on the idea of improving a photocatalytic degradation property of ZnO, by using different strategies such as nonmetal and metal doping and specific charge and polar molecule functionalization.

For nonmetal doping strategies, I have chosen GO as a nonmetal dopant model. Hydrothermal technique to prepare ZnO/rGO nanocomposites with high photosensitivity and high photodegradation of MB has been observed. This study indicates that using the optimal amount of GO additive plays a significant role in not only nanoparticle–nanorod tunability, but also in inducing the intrinsic defect formation of ZnO. The ZnO/rGO based on UV detection and photocatalyst outperformed pristine ZnO, as the GO additive generates more defects and disorder, leading to increase absorbed oxygen for carrier concentration increment. Additionally, it provides the alternative charge carrier pathway to prevent charge carrier recombination and prolong photocatalytic reaction life time.

For metal doping strategies, I have selected cerium as a metal dopant model. A simple hydrothermal technique was utilized to prepare cerium-oxide-nanoparticle-decorated zinc oxide for photocatalytic application. It was found that an increase in Ce doping does not affect the morphology of Ce/ZnO, which remains unchanged in comparison with the hexagonal wurtzite structures of pristine ZnO. XRD and XPS analyses revealed the existence of a cubic CeO<sub>2</sub>

phase and  $\text{Ce}^{4+}$  ions in Ce-doped ZnO composite samples. Additionally, an increase in Ce doping in ZnO results in narrower optical energy band tunability and reduced charge recombination. When compared with pristine ZnO, the Ce/ZnO catalysts showed superior photocatalytic degradation of methyl orange, which increased from 69.42% (ZnO) to 94.06% (7% Ce/ZnO) in 60 min. This may be due to the  $\text{Ce}^{4+}$  ions, which can trap more electrons, resulting in an increase in generated radicals. Moreover,  $\text{CeO}_2/\text{ZnO}$  heterojunctions were formed, which provide a carrier pathway to obstruct charge recombination and improve the photocatalytic degradation performance.

For specific charge and polar molecule functionalization strategies, I have chosen aniline as a specific charge molecule model. Aniline molecules were attached onto ZnO surface by using impregnation technique. Aniline acted as a positive charge modifier on ZnO surface. This modified ZnO showed promising improvement for MO dye adsorption by enhancing the electrostatic interaction between positive aniline functionalized ZnO and negative MO molecules. The photocatalytic degradation of MO was observed over 98%, faster than ZnO in an hour. The acceleration in photocatalytic degradation suggested that aniline functionalization could be viable option to modify surface charge and improve photocatalytic performance for advance materials

## References

- [1] A. Paliwal, A. Sharma, M. Tomar, and V. Gupta, “Carbon monoxide (co) optical gas sensor based on zno thin films,” *Sensors and Actuators B: Chemical*, vol. 250, pp. 679–685, 2017.
- [2] Y. Hou and A. H. Jayatissa, “Influence of laser doping on nanocrystalline zno thin films gas sensors,” *Progress in Natural Science: Materials International*, vol. 27, no. 4, pp. 435–442, 2017.
- [3] V. M. Latyshev, T. O. Berestok, A. Opanasyuk, A. Korniyushchenko, and V. I. Perekrestov, “Nanostructured zno films for potential use in lpg gas sensors,” *Solid State Sciences*, vol. 67, pp. 109–113, 2017.
- [4] W. Ponhan, S. Phadungdhithidhada, and S. Choopun, “Fabrication of ethanol sensors based on zno thin film field-effect transistor prepared by thermal evaporation deposition,” *Materials Today: Proceedings*, vol. 4, no. 5, pp. 6342–6348, 2017.
- [5] A. F. V. da Fonseca, R. L. Siqueira, R. Landers, J. L. Ferrari, N. L. Marana, J. R. Sambrano, F. d. A. La Porta, and M. A. Schiavon, “A theoretical and experimental investigation of eu-doped zno nanorods and its application on dye sensitized solar cells,” *Journal of Alloys and Compounds*, vol. 739, pp. 939–947, 2018.
- [6] T Marimuthu, N Anandhan, R Thangamuthu, and S Surya, “Influence of solution viscosity on hydrothermally grown zno thin films for dssc applications,” *Superlattices and Microstructures*, vol. 98, pp. 332–341, 2016.

- [7] K. Kaewyai, S. Choopun, A. Gardchareon, P. Ruankham, S. Phadungdhitidhada, and D. Wongratanaphisan, "Effects of mixed-phase copper oxide nanofibers in zno dye-sensitized solar cells on efficiency enhancement," *Journal of Nanoscience and Nanotechnology*, vol. 17, no. 8, pp. 5475–5480, 2017.
- [8] T. Iqbal, A. Aziz, M. Khan, S. Andleeb, H. Mahmood, A. A. Khan, R. Khan, and M. Shafique, "Surfactant assisted synthesis of zno nanostructures using atmospheric pressure microplasma electrochemical process with antibacterial applications," *Materials Science and Engineering: B*, vol. 228, pp. 153–159, 2018.
- [9] T. Voss and S. R. Waldvogel, "Hybrid leds based on zno nanowire structures," *Materials Science in Semiconductor Processing*, vol. 69, pp. 52–56, 2017.
- [10] M. Liu, K. Li, F. Kong, J. Zhao, Q. Yue, and X. Yu, "Improvement of the light extraction efficiency of light-emitting diodes based on zno nanotubes," *Photonics and Nanostructures-Fundamentals and Applications*, vol. 16, pp. 9–15, 2015.
- [11] G. Zhu, R. Yang, S. Wang, and Z. L. Wang, "Flexible high-output nanogenerator based on lateral zno nanowire array," *Nano letters*, vol. 10, no. 8, pp. 3151–3155, 2010.
- [12] K. Liu, M. Sakurai, and M. Aono, "Zno-based ultraviolet photodetectors," *Sensors*, vol. 10, no. 9, pp. 8604–8634, 2010.
- [13] R Paul, R. Gayen, S Biswas, S. V. Bhat, and R Bhunia, "Enhanced uv detection by transparent graphene oxide/zno composite thin films," *RSC advances*, vol. 6, no. 66, pp. 61 661–61 672, 2016.



- [14] Y. Su, G. Xie, T. Xie, Y. Long, Z. Ye, X. Du, Z. Wu, and Y. Jiang, "Piezophototronic uv photosensing with zno nanowires array," in *2015 IEEE SENSORS*, IEEE, 2015, pp. 1–4.
- [15] V.-T. Tran, Y. Wei, H. Yang, Z. Zhan, and H. Du, "All-inkjet-printed flexible zno micro photodetector for a wearable uv monitoring device," *Nanotechnology*, vol. 28, no. 9, p. 095 204, 2017.
- [16] T. Lv, L. Pan, X. Liu, T. Lu, G. Zhu, and Z. Sun, "Enhanced photocatalytic degradation of methylene blue by zno-reduced graphene oxide composite synthesized via microwave-assisted reaction," *Journal of Alloys and Compounds*, vol. 509, no. 41, pp. 10 086–10 091, 2011.
- [17] H. Jung, T.-T. Pham, and E. W. Shin, "Interactions between zno nanoparticles and amorphous g-c3n4 nanosheets in thermal formation of g-c3n4/zno composite materials: The annealing temperature effect," *Applied Surface Science*, vol. 458, pp. 369–381, 2018.
- [18] J. He, C. Niu, C. Yang, J. Wang, and X. Su, "Reduced graphene oxide anchored with zinc oxide nanoparticles with enhanced photocatalytic activity and gas sensing properties," *RSC Advances*, vol. 4, no. 104, pp. 60 253–60 259, 2014.
- [19] C. Rodwihok, S. Choopun, P. Ruankham, A. Gardchareon, S. Phadungthitidhada, and D. Wongratanaphisan, "Uv sensing properties of zno nanowires/nanorods," *Applied Surface Science*, vol. 477, pp. 159–165, 2019.
- [20] S. Heinonen, J.-P. Nikkanen, E. Huttunen-Saarivirta, and E. Levänen, "Investigation of long-term chemical stability of structured zno films in

- aqueous solutions of varying conditions,” *Thin Solid Films*, vol. 638, pp. 410–419, 2017.
- [21] M Kahouli, A Barhoumi, A. Bouzid, A Al-Hajry, and S Guermazi, “Structural and optical properties of zno nanoparticles prepared by direct precipitation method,” *superlattices and Microstructures*, vol. 85, pp. 7–23, 2015.
- [22] D. Bhatia, H. Sharma, R. Meena, and V. Palkar, “A novel zno piezoelectric microcantilever energy scavenger: Fabrication and characterization,” *Sensing and bio-sensing research*, vol. 9, pp. 45–52, 2016.
- [23] E. Nour, O. Nur, and M. Willander, “Zinc oxide piezoelectric nano-generators for low frequency applications,” *Semiconductor Science and Technology*, vol. 32, no. 6, p. 064 005, 2017.
- [24] P. Wang and H. Du, “Zno thin film piezoelectric mems vibration energy harvesters with two piezoelectric elements for higher output performance,” *Review of Scientific Instruments*, vol. 86, no. 7, p. 075 002, 2015.
- [25] J Zhang, X. Li, J. Lu, P Wu, J Huang, Q Wang, B Lu, Y. Zhang, B. Zhao, and Z. Ye, “Evolution of electrical performance of zno-based thin-film transistors by low temperature annealing,” *AIP Advances*, vol. 2, no. 2, p. 022 118, 2012.
- [26] X. Wen, W. Wu, Y. Ding, and Z. L. Wang, “Piezotronic effect in flexible thin-film based devices,” *Advanced Materials*, vol. 25, no. 24, pp. 3371–3379, 2013.

- [27] K. Choi, T. Kang, and S.-G. Oh, "Preparation of disk shaped zno particles using surfactant and their pl properties," *Materials Letters*, vol. 75, pp. 240–243, 2012.
- [28] E. Gharoy Ahangar, M. H. Abbaspour-Fard, N. Shahtahmassebi, M. Khojastehpour, and P. Maddahi, "Preparation and characterization of pva/zno nanocomposite," *Journal of food processing and preservation*, vol. 39, no. 6, pp. 1442–1451, 2015.
- [29] M. Al-Fori, S. Dobretsov, M. T. Z. Myint, and J. Dutta, "Antifouling properties of zinc oxide nanorod coatings," *Biofouling*, vol. 30, no. 7, pp. 871–882, 2014.
- [30] S. Liang, K. Xiao, Y. Mo, and X. Huang, "A novel zno nanoparticle blended polyvinylidene fluoride membrane for anti-irreversible fouling," *Journal of membrane science*, vol. 394, pp. 184–192, 2012.
- [31] J.-M. Herrmann, "Heterogeneous photocatalysis: Fundamentals and applications to the removal of various types of aqueous pollutants," *Catalysis today*, vol. 53, no. 1, pp. 115–129, 1999.
- [32] D Rajamanickam and M Shanthi, "Photocatalytic degradation of an organic pollutant by zinc oxide–solar process," *Arabian Journal of Chemistry*, vol. 9, S1858–S1868, 2016.
- [33] M. Rauf and S. S. Ashraf, "Fundamental principles and application of heterogeneous photocatalytic degradation of dyes in solution," *Chemical engineering journal*, vol. 151, no. 1-3, pp. 10–18, 2009.
- [34] Z. Yu, L.-C. Yin, Y. Xie, G. Liu, X. Ma, and H.-M. Cheng, "Crystallinity-dependent substitutional nitrogen doping in zno and its

- improved visible light photocatalytic activity,” *Journal of colloid and interface science*, vol. 400, pp. 18–23, 2013.
- [35] O. Bechambi, S. Sayadi, and W. Najjar, “Photocatalytic degradation of bisphenol a in the presence of c-doped zno: Effect of operational parameters and photodegradation mechanism,” *Journal of Industrial and Engineering Chemistry*, vol. 32, pp. 201–210, 2015.
- [36] B. P. Nenavathu, A. K. Rao, A. Goyal, A. Kapoor, and R. K. Dutta, “Synthesis, characterization and enhanced photocatalytic degradation efficiency of se doped zno nanoparticles using trypan blue as a model dye,” *Applied Catalysis A: General*, vol. 459, pp. 106–113, 2013.
- [37] M Rezaei and A Habibi-Yangjeh, “Simple and large scale refluxing method for preparation of ce-doped zno nanostructures as highly efficient photocatalyst,” *Applied surface science*, vol. 265, pp. 591–596, 2013.
- [38] S. Yun, J. Lee, J. Chung, and S. Lim, “Improvement of zno nanorod-based dye-sensitized solar cell efficiency by al-doping,” *Journal of Physics and Chemistry of Solids*, vol. 71, no. 12, pp. 1724–1731, 2010.
- [39] D. Zhu, T. Hu, Y. Zhao, W. Zang, L. Xing, and X. Xue, “High-performance self-powered/active humidity sensing of fe-doped zno nanoarray nanogenerator,” *Sensors and Actuators B: Chemical*, vol. 213, pp. 382–389, 2015.
- [40] R. Wang, J. H. Xin, Y. Yang, H. Liu, L. Xu, and J. Hu, “The characteristics and photocatalytic activities of silver doped zno nanocrystallites,” *Applied Surface Science*, vol. 227, no. 1-4, pp. 312–317, 2004.

- [41] M. Fu, Y. Li, P. Lu, J. Liu, F. Dong, *et al.*, “Sol–gel preparation and enhanced photocatalytic performance of cu-doped zno nanoparticles,” *Applied Surface Science*, vol. 258, no. 4, pp. 1587–1591, 2011.
- [42] R. Saleh and N. F. Djaja, “Transition-metal-doped zno nanoparticles: Synthesis, characterization and photocatalytic activity under uv light,” *Spectrochimica Acta Part A: Molecular and Biomolecular Spectroscopy*, vol. 130, pp. 581–590, 2014.
- [43] G Poongodi, R. M. Kumar, and R Jayavel, “Influence of s doping on structural, optical and visible light photocatalytic activity of zno thin films,” *Ceramics International*, vol. 40, no. 9, pp. 14 733–14 740, 2014.
- [44] C. Kim, S. J. Doh, S. G. Lee, S. J. Lee, and H. Y. Kim, “Visible-light absorptivity of a zincoxysulfide (znox<sub>s1-x</sub>) composite semiconductor and its photocatalytic activities for degradation of organic pollutants under visible-light irradiation,” *Applied Catalysis A: General*, vol. 330, pp. 127–133, 2007.
- [45] S Janitabar Darzi, A Mahjoub, and A Bayat, “Sulfur modified zno nanorod as a high performance photocatalyst for degradation of congoredazo dye,” *International Journal of Nano Dimension*, vol. 6, no. 4, pp. 425–431, 2015.
- [46] J. Macías-Sánchez, L Hinojosa-Reyes, A. d. Caballero-Quintero, W De La Cruz, E Ruiz-Ruiz, A Hernández-Ramírez, and J. Guzmán-Mar, “Synthesis of nitrogen-doped zno by sol–gel method: Characterization and its application on visible photocatalytic degradation of 2, 4-d and picloram herbicides,” *Photochemical & Photobiological Sciences*, vol. 14, no. 3, pp. 536–542, 2015.

- [47] A. B. Lavand and Y. S. Malghe, "Synthesis, characterization and visible light photocatalytic activity of nitrogen-doped zinc oxide nanospheres," *Journal of Asian Ceramic Societies*, vol. 3, no. 3, pp. 305–310, 2015.
- [48] Y. Qiu, H. Fan, G. Tan, M. Yang, X. Yang, and S. Yang, "Effect of nitrogen doping on the photo-catalytic properties of nitrogen doped zno tetrapods," *Materials Letters*, vol. 131, pp. 64–66, 2014.
- [49] S. Shinde, C. Bhosale, and K. Rajpure, "Photocatalytic degradation of toluene using sprayed n-doped zno thin films in aqueous suspension," *Journal of Photochemistry and Photobiology B: Biology*, vol. 113, pp. 70–77, 2012.
- [50] S. Kuriakose, B. Satpati, and S. Mohapatra, "Enhanced photocatalytic activity of co doped zno nanodisks and nanorods prepared by a facile wet chemical method," *Physical Chemistry Chemical Physics*, vol. 16, no. 25, pp. 12 741–12 749, 2014.
- [51] A Mondal, N Giri, S Sarkar, S Majumdar, and R Ray, "Tuning the photocatalytic activity of zno by tm (tm= fe, co, ni) doping," *Materials Science in Semiconductor Processing*, vol. 91, pp. 333–340, 2019.
- [52] N. Khalid, A Hammad, M. Tahir, M Rafique, T Iqbal, G Nabi, and M. Hussain, "Enhanced photocatalytic activity of al and fe co-doped zno nanorods for methylene blue degradation," *Ceramics International*, vol. 45, no. 17, pp. 21 430–21 435, 2019.
- [53] A. Riaz, A. Ashraf, H. Taimoor, S. Javed, M. A. Akram, M. Islam, M. Mujahid, I. Ahmad, and K. Saeed, "Photocatalytic and photostability behavior of ag-and/or al-doped zno films in methylene blue and rhodamine b under uv-c irradiation," *Coatings*, vol. 9, no. 3, p. 202, 2019.

- [54] I. Ahmad, "Inexpensive and quick photocatalytic activity of rare earth (er, yb) co-doped zno nanoparticles for degradation of methyl orange dye," *Separation and Purification Technology*, p. 115 726, 2019.
- [55] B Poornaprakash, U Chalapathi, M. C. Sekhar, V Rajendar, S. P. Vattikuti, M. S. P. Reddy, Y. Suh, and S.-H. Park, "Effect of eu<sup>3+</sup> on the morphology, structural, optical, magnetic, and photocatalytic properties of zno nanoparticles," *Superlattices and Microstructures*, vol. 123, pp. 154–163, 2018.
- [56] W. Mohamed and A. M. Abu-Dief, "Synthesis, characterization and photocatalysis enhancement of eu<sub>2</sub>o<sub>3</sub>-zno mixed oxide nanoparticles," *Journal of Physics and Chemistry of Solids*, vol. 116, pp. 375–385, 2018.
- [57] U. Alam, A. Khan, D. Ali, D. Bahnemann, and M Muneer, "Comparative photocatalytic activity of sol–gel derived rare earth metal (la, nd, sm and dy)-doped zno photocatalysts for degradation of dyes," *RSC advances*, vol. 8, no. 31, pp. 17 582–17 594, 2018.
- [58] S. B. Satpal and A. A. Athawale, "Synthesis of zno and nd doped zno polyscales for removal of rhodamine 6g dye under uv light irradiation," *Materials Research Express*, vol. 5, no. 8, p. 085 501, 2018.
- [59] L. T. Nguyen, L. T. Nguyen, A. T. Duong, B. D. Nguyen, N. Quang Hai, V. H. Chu, T. D. Nguyen, and L. G. Bach, "Preparation, characterization and photocatalytic activity of la-doped zinc oxide nanoparticles," *Materials*, vol. 12, no. 8, p. 1195, 2019.
- [60] P Hemalatha, S. Karthick, K. Hemalatha, M. Yi, H.-J. Kim, and M Alagar, "La-doped zno nanoflower as photocatalyst for methylene

- blue dye degradation under uv irradiation,” *Journal of Materials Science: Materials in Electronics*, vol. 27, no. 3, pp. 2367–2378, 2016.
- [61] T. Jia, W. Wang, F. Long, Z. Fu, H. Wang, and Q. Zhang, “Fabrication, characterization and photocatalytic activity of la-doped zno nanowires,” *Journal of Alloys and compounds*, vol. 484, no. 1-2, pp. 410–415, 2009.
- [62] Z. Shen, Q. Zhang, C. Yin, S. Kang, H. Jia, X. Li, X. Li, Y. Wang, and L. Cui, “Facile synthesis of 3d flower-like mesoporous ce-zno at room temperature for the sunlight-driven photocatalytic degradations of rhb and phenol,” *Journal of colloid and interface science*, vol. 556, pp. 726–733, 2019.
- [63] S. Rajendran, M. M. Khan, F. Gracia, J. Qin, V. K. Gupta, and S. Arumainathan, “Ce 3+-ion-induced visible-light photocatalytic degradation and electrochemical activity of zno/ceo2 nanocomposite,” *Scientific reports*, vol. 6, p. 31 641, 2016.
- [64] M. M. Khan, W. Khan, M. Ahamed, and A. N. Alhazaa, “Microstructural properties and enhanced photocatalytic performance of zn doped ceo2 nanocrystals,” *Scientific reports*, vol. 7, no. 1, p. 12 560, 2017.
- [65] X. Chang, Z. Li, X. Zhai, S. Sun, D. Gu, L. Dong, Y. Yin, and Y. Zhu, “Efficient synthesis of sunlight-driven zno-based heterogeneous photocatalysts,” *Materials & Design*, vol. 98, pp. 324–332, 2016.
- [66] C. Bosch-Navarro, E. Coronado, C. Martí-Gastaldo, J. Sánchez-Royo, and M. G. Gómez, “Influence of the ph on the synthesis of reduced graphene oxide under hydrothermal conditions,” *Nanoscale*, vol. 4, no. 13, pp. 3977–3982, 2012.



- [67] A. I. Uddin, D.-T. Phan, and G.-S. Chung, “Low temperature acetylene gas sensor based on ag nanoparticles-loaded zno-reduced graphene oxide hybrid,” *Sensors and Actuators B: Chemical*, vol. 207, pp. 362–369, 2015.
- [68] M. D. Stoller, S. Park, Y. Zhu, J. An, and R. S. Ruoff, “Graphene-based ultracapacitors,” *Nano letters*, vol. 8, no. 10, pp. 3498–3502, 2008.
- [69] A. A. Balandin, S. Ghosh, W. Bao, I. Calizo, D. Teweldebrhan, F. Miao, and C. N. Lau, “Superior thermal conductivity of single-layer graphene,” *Nano letters*, vol. 8, no. 3, pp. 902–907, 2008.
- [70] K. I. Bolotin, K. J. Sikes, Z. Jiang, M. Klima, G. Fudenberg, J. Hone, P. Kim, and H. Stormer, “Ultrahigh electron mobility in suspended graphene,” *Solid state communications*, vol. 146, no. 9-10, pp. 351–355, 2008.
- [71] C. Lee, X. Wei, J. W. Kysar, and J. Hone, “Measurement of the elastic properties and intrinsic strength of monolayer graphene,” *science*, vol. 321, no. 5887, pp. 385–388, 2008.
- [72] B Paulchamy, G Arthi, and B. Lignesh, “A simple approach to stepwise synthesis of graphene oxide nanomaterial,” *J Nanomed Nanotechnol*, vol. 6, no. 1, p. 1, 2015.
- [73] Y. Liu, Y. Hu, M. Zhou, H. Qian, and X. Hu, “Microwave-assisted non-aqueous route to deposit well-dispersed zno nanocrystals on reduced graphene oxide sheets with improved photoactivity for the decolorization of dyes under visible light,” *Applied Catalysis B: Environmental*, vol. 125, pp. 425–431, 2012.
- [74] D. Fu, G. Han, F. Yang, T. Zhang, Y. Chang, and F. Liu, “Seed-mediated synthesis and the photo-degradation activity of zno-graphene hybrids

- excluding the influence of dye adsorption,” *Applied surface science*, vol. 283, pp. 654–659, 2013.
- [75] S. Liu, H. Sun, S. Liu, and S. Wang, “Graphene facilitated visible light photodegradation of methylene blue over titanium dioxide photocatalysts,” *Chemical Engineering Journal*, vol. 214, pp. 298–303, 2013.
- [76] X. Zhou, T. Shi, and H. Zhou, “Hydrothermal preparation of zno-reduced graphene oxide hybrid with high performance in photocatalytic degradation,” *Applied surface science*, vol. 258, no. 17, pp. 6204–6211, 2012.
- [77] Y. Feng, N. Feng, Y. Wei, and G. Zhang, “An in situ gelatin-assisted hydrothermal synthesis of zno–reduced graphene oxide composites with enhanced photocatalytic performance under ultraviolet and visible light,” *RSC advances*, vol. 4, no. 16, pp. 7933–7943, 2014.
- [78] H. Wu, S. Lin, C. Chen, W. Liang, X. Liu, and H. Yang, “A new zno/rgo/polyaniline ternary nanocomposite as photocatalyst with improved photocatalytic activity,” *Materials Research Bulletin*, vol. 83, pp. 434–441, 2016.
- [79] F. S. Omar, H. Nay Ming, S. M. Hafiz, and L. H. Ngee, “Microwave synthesis of zinc oxide/reduced graphene oxide hybrid for adsorption-photocatalysis application,” *International Journal of Photoenergy*, vol. 2014, 2014.
- [80] H. N. Tien, N. T. Khoa, S. H. Hahn, J. S. Chung, E. W. Shin, S. H. Hur, *et al.*, “One-pot synthesis of a reduced graphene oxide–zinc oxide sphere

- composite and its use as a visible light photocatalyst,” *Chemical Engineering Journal*, vol. 229, pp. 126–133, 2013.
- [81] R. Hong, T. Pan, J. Qian, and H. Li, “Synthesis and surface modification of zno nanoparticles,” *Chemical Engineering Journal*, vol. 119, no. 2-3, pp. 71–81, 2006.
- [82] G. Farzi, R. Tayebee, and S. Naghibinasab, “Surface modification of zno nano-particles with trimetoxymethyl silane and oleic acid and studying their dispersion in organic media,” 2015.
- [83] P. Hu, N. Han, D. Zhang, J. C. Ho, and Y. Chen, “Highly formaldehyde-sensitive, transition-metal doped zno nanorods prepared by plasma-enhanced chemical vapor deposition,” *Sensors and Actuators B: Chemical*, vol. 169, pp. 74–80, 2012.
- [84] R. A. Sperling and W. J. Parak, “Surface modification, functionalization and bioconjugation of colloidal inorganic nanoparticles,” *Philosophical Transactions of the Royal Society A: Mathematical, Physical and Engineering Sciences*, vol. 368, no. 1915, pp. 1333–1383, 2010.
- [85] X. Zhang, Y. Xia, and T. He, “Tuning photoluminescence properties of zno nanorods via surface modification,” *Materials Chemistry and Physics*, vol. 137, no. 2, pp. 622–627, 2012.
- [86] R. Hong, J. Li, L. Chen, D. Liu, H. Li, Y. Zheng, and J. Ding, “Synthesis, surface modification and photocatalytic property of zno nanoparticles,” *Powder Technology*, vol. 189, no. 3, pp. 426–432, 2009.
- [87] J. Luo, X. Dai, S. Bai, Y. Jin, Z. Ye, and X. Guo, “Ligand exchange of colloidal zno nanocrystals from the high temperature and nonaqueous approach,” *Nano-Micro Letters*, vol. 5, no. 4, pp. 274–280, 2013.

- [88] D. Kwon, J. Park, J. Park, S. Y. Choi, and T. H. Yoon, “Effects of surface-modifying ligands on the colloidal stability of zno nanoparticle dispersions in in vitro cytotoxicity test media,” *International journal of nanomedicine*, vol. 9, no. Suppl 2, p. 57, 2014.
- [89] S. Kango, S. Kalia, A. Celli, J. Njuguna, Y. Habibi, and R. Kumar, “Surface modification of inorganic nanoparticles for development of organic–inorganic nanocomposites—a review,” *Progress in Polymer Science*, vol. 38, no. 8, pp. 1232–1261, 2013.
- [90] S. Kuriakose, N. Bhardwaj, J. Singh, B. Satpati, and S. Mohapatra, “Structural, optical and photocatalytic properties of flower-like zno nanostructures prepared by a facile wet chemical method,” *Beilstein journal of nanotechnology*, vol. 4, no. 1, pp. 763–770, 2013.
- [91] W.-J. Ong, S.-Y. Voon, L.-L. Tan, B. T. Goh, S.-T. Yong, and S.-P. Chai, “Enhanced daylight-induced photocatalytic activity of solvent exfoliated graphene (seg)/zno hybrid nanocomposites toward degradation of reactive black 5,” *Industrial & Engineering Chemistry Research*, vol. 53, no. 44, pp. 17 333–17 344, 2014.
- [92] S. Pati, S. Majumder, and P Banerji, “Role of oxygen vacancy in optical and gas sensing characteristics of zno thin films,” *Journal of alloys and compounds*, vol. 541, pp. 376–379, 2012.
- [93] X. Zhang, J. Qin, Y. Xue, P. Yu, B. Zhang, L. Wang, and R. Liu, “Effect of aspect ratio and surface defects on the photocatalytic activity of zno nanorods,” *Scientific reports*, vol. 4, p. 4596, 2014.
- [94] S. B. Darling, “Perspective: Interfacial materials at the interface of energy and water,” *Journal of Applied Physics*, vol. 124, no. 3, p. 030 901, 2018.

- [95] P. Raizada, A. Sudhaik, and P. Singh, "Photocatalytic water decontamination using graphene and zno coupled photocatalysts: A review," *Materials Science for Energy Technologies*, 2019.
- [96] M. Thepnurat, P. Ruankham, S. Phadunghitidhada, A. Gardchareon, D. Wongratanaphisan, and S. Choopun, "Efficient charge-transport uv sensor based on interlinked zno tetrapod networks," *Surface and Coatings Technology*, vol. 306, pp. 25–29, 2016.
- [97] S. Ghosh, K. Das, N Tripathy, G Bose, D. Kim, T. Lee, J. M. Myoung, and J. Kar, "Ultraviolet photodetection characteristics of zinc oxide thin films and nanostructures," in *IOP Conference Series: Materials Science and Engineering*, IOP Publishing, vol. 115, 2016, p. 012 035.
- [98] Q Humayun, U Hashim, C. Ruzaidi, and K. L. Foo, "The strategy to control the morphology of zno nanostructure uv sensor," in *IOP Conference Series: Materials Science and Engineering*, IOP Publishing, vol. 99, 2015, p. 012 017.
- [99] A. Lee, J. A. Libera, R. Z. Waldman, A. Ahmed, J. R. Avila, J. W. Elam, and S. B. Darling, "Conformal nitrogen-doped tio<sub>2</sub> photocatalytic coatings for sunlight-activated membranes," *Advanced Sustainable Systems*, vol. 1, no. 1-2, p. 1 600 041, 2017.
- [100] S. F. Akhtarianfar, A. Khayatian, R. Shakernejad, M. Almasi-Kashi, and S. W. Hong, "Improved sensitivity of uv sensors in hierarchically structured arrays of network-loaded zno nanorods via optimization techniques," *RSC advances*, vol. 7, no. 51, pp. 32 316–32 326, 2017.

- [101] L. Shafiei, S. Darbari, and F. Dehghan Nayeri, "Realization of a reduced graphene oxide/zno nanorod photodetector, suitable for self-powered applications," *Scientia Iranica*, vol. 25, no. 3, pp. 1824–1834, 2018.
- [102] C. Chen, P. Zhou, N. Wang, Y. Ma, and H. San, "Uv-assisted photochemical synthesis of reduced graphene oxide/zno nanowires composite for photoresponse enhancement in uv photodetectors," *Nanomaterials*, vol. 8, no. 1, p. 26, 2018.
- [103] Z. Wang, X. Zhan, Y. Wang, S. Muhammad, Y. Huang, and J. He, "A flexible uv nanosensor based on reduced graphene oxide decorated zno nanostructures," *Nanoscale*, vol. 4, no. 8, pp. 2678–2684, 2012.
- [104] M. Azarang, A. Shuhaimi, R. Yousefi, and M. Sookhakian, "Effects of graphene oxide concentration on optical properties of zno/rgo nanocomposites and their application to photocurrent generation," *Journal of Applied Physics*, vol. 116, no. 8, p. 084 307, 2014.
- [105] L.-W. Zhang, H.-B. Fu, and Y.-F. Zhu, "Efficient tio<sub>2</sub> photocatalysts from surface hybridization of tio<sub>2</sub> particles with graphite-like carbon," *Advanced Functional Materials*, vol. 18, no. 15, pp. 2180–2189, 2008.
- [106] P. Makal and D. Das, "Superior photocatalytic dye degradation under visible light by reduced graphene oxide laminated tio<sub>2</sub>-b nanowire composite," *Journal of Environmental Chemical Engineering*, vol. 7, no. 5, p. 103 358, 2019.
- [107] M. Khandelwal and A. Kumar, "Electrochemical behavior of glycine-mediated n-doped reduced graphene oxide," *New Journal of Chemistry*, vol. 41, no. 16, pp. 8333–8340, 2017.

- [108] V. Mote, V. Huse, Y Purushotham, S. Shah, and B. Dole, "Synthesis and characterization of mn doped zns nanometer-sized particles," in *AIP Conference Proceedings*, American Institute of Physics, vol. 1447, 2012, pp. 217–218.
- [109] P. Teo, H. Lim, N. Huang, C. H. Chia, and I Harrison, "Room temperature in situ chemical synthesis of fe<sub>3</sub>o<sub>4</sub>/graphene," *Ceramics International*, vol. 38, no. 8, pp. 6411–6416, 2012.
- [110] S. V. Kumar, N. Huang, N Yusoff, and H. Lim, "High performance magnetically separable graphene/zinc oxide nanocomposite," *Materials Letters*, vol. 93, pp. 411–414, 2013.
- [111] M. Khandelwal, Y. Li, A. Molla, S. H. Hur, and J. S. Chung, "Single precursor mediated one-step synthesis of ternary-doped and functionalized reduced graphene oxide by ph tuning for energy storage applications," *Chemical Engineering Journal*, vol. 330, pp. 965–978, 2017.
- [112] M. Khandelwal, Y. Li, S. H. Hur, and J. S. Chung, "Surface modification of co-doped reduced graphene oxide through alkanolamine functionalization for enhanced electrochemical performance," *New Journal of Chemistry*, vol. 42, no. 2, pp. 1105–1114, 2018.
- [113] A Maulana, A. Nugraheni, D. Jayanti, S Mustofa, M. Baqiya, *et al.*, "Defect and magnetic properties of reduced graphene oxide prepared from old coconut shell," in *IOP Conference Series: Materials Science and Engineering*, IOP Publishing, vol. 196, 2017, p. 012021.
- [114] N. Sharma, V. Sharma, Y. Jain, M. Kumari, R. Gupta, S. Sharma, and K Sachdev, "Synthesis and characterization of graphene oxide (go) and

- reduced graphene oxide (rgo) for gas sensing application,” in *Macromolecular Symposia*, Wiley Online Library, vol. 376, 2017, p. 1 700 006.
- [115] M. Shahid, Y. Wang, J. Yang, T. Li, J. Cheng, M. Zhang, Y. Xing, C. Wan, and W. Pan, “Synergetic enhancement in photosensitivity and flexibility of photodetectors based on hybrid nanobelt network,” *Advanced Materials Interfaces*, vol. 4, no. 22, p. 1 700 909, 2017.
- [116] G Wisz, I Virt, P Sagan, P Potera, and R Yavorskyi, “Structural, optical and electrical properties of zinc oxide layers produced by pulsed laser deposition method,” *Nanoscale research letters*, vol. 12, no. 1, p. 253, 2017.
- [117] E Muchuweni, T. Sathiaraj, and H Nyakoty, “Synthesis and characterization of zinc oxide thin films for optoelectronic applications,” *Heliyon*, vol. 3, no. 4, e00285, 2017.
- [118] L. Chen, Z. Xu, J. Li, B. Zhou, M. Shan, Y. Li, L. Liu, B. Li, and J. Niu, “Modifying graphite oxide nanostructures in various media by high-energy irradiation,” *RSC Advances*, vol. 4, no. 2, pp. 1025–1031, 2014.
- [119] R Al-Gaashani, S. Radiman, A. Daud, N Tabet, and Y. Al-Douri, “Xps and optical studies of different morphologies of zno nanostructures prepared by microwave methods,” *Ceramics International*, vol. 39, no. 3, pp. 2283–2292,
- [120] F. C. Romeiro, M. A. Rodrigues, L. A. Silva, A. C. Catto, L. F. da Silva, E. Longo, E. Nossol, and R. C. Lima, “Rgo-zno nanocomposites for high electrocatalytic effect on water oxidation obtained by



- microwave-hydrothermal method,” *Applied Surface Science*, vol. 423, pp. 743–751, 2017.
- [121] G. R. Dillip, A. N. Banerjee, V. C. Anitha, B. Deva Prasad Raju, S. W. Joo, and B. K. Min, “Oxygen vacancy-induced structural, optical, and enhanced supercapacitive performance of zinc oxide anchored graphitic carbon nanofiber hybrid electrodes,” *ACS applied materials & interfaces*, vol. 8, no. 7, pp. 5025–5039, 2016.
- [122] M Zare, S Safa, R Azimirad, and S Mokhtari, “Graphene oxide incorporated zno nanostructures as a powerful ultraviolet composite detector,” *Journal of Materials Science: Materials in Electronics*, vol. 28, no. 9, pp. 6919–6927, 2017.
- [123] H. W. Noh, S. M. Jeong, J. Cho, and J.-I. Hong, “Ultrahigh photosensitivity of the polar surfaces of single crystalline zno nanoplates,” *Nanoscale*, vol. 10, no. 15, pp. 6801–6805, 2018.
- [124] G. Jing, X. Zhang, and D. Yu, “Effect of surface morphology on the mechanical properties of zno nanowires,” *Applied Physics A*, vol. 100, no. 2, pp. 473–478, 2010.
- [125] S. K. Mandal, K. Dutta, S. Pal, S. Mandal, A. Naskar, P. K. Pal, T. Bhattacharya, A. Singha, R. Saikh, S. De, *et al.*, “Engineering of zno/rgo nanocomposite photocatalyst towards rapid degradation of toxic dyes,” *Materials Chemistry and Physics*, vol. 223, pp. 456–465, 2019.
- [126] V. S. Rana, J. K. Rajput, T. K. Pathak, and L. Purohit, “Multilayer mgzno/zno thin films for uv photodetectors,” *Journal of Alloys and Compounds*, vol. 764, pp. 724–729, 2018.

- [127] Y. Lang, H. Gao, W. Jiang, L. Xu, and H. Hou, "Photoresponse and decay mechanism of an individual zno nanowire uv sensor," *Sensors and Actuators A: Physical*, vol. 174, pp. 43–46, 2012.
- [128] L.-C. Chao, C.-C. Ye, Y.-P. Chen, and H.-Z. Yu, "Facile fabrication of zno nanowire-based uv sensors by focused ion beam micromachining and thermal oxidation," *Applied surface science*, vol. 282, pp. 384–389, 2013.
- [129] A Bedia, F. Bedia, B Benyoucef, and S Hamzaoui, "Electrical characteristics of ultraviolet photodetector based on zno nanostructures," *Physics Procedia*, vol. 55, pp. 53–60, 2014.
- [130] P. Shewale, N. Lee, S. Lee, K. Kang, and Y. Yu, "Ti doped zno thin film based uv photodetector: Fabrication and characterization," *Journal of Alloys and Compounds*, vol. 624, pp. 251–257, 2015.
- [131] S Safa, R Sarraf-Mamoory, and R Azimirad, "Investigation of reduced graphene oxide effects on ultra-violet detection of zno thin film," *Physica E: Low-dimensional Systems and Nanostructures*, vol. 57, pp. 155–160, 2014.
- [132] M Zare, S Safa, R Azimirad, and S Mokhtari, "Graphene oxide incorporated zno nanostructures as a powerful ultraviolet composite detector," *Journal of Materials Science: Materials in Electronics*, vol. 28, no. 9, pp. 6919–6927, 2017.
- [133] J. Qin, X. Zhang, Y. Xue, N. Kittiwattanothai, P. Kongsittikul, N. Rodthongkum, S. Limpanart, M. Ma, and R. Liu, "A facile synthesis of nanorods of zno/graphene oxide composites with enhanced photocatalytic activity," *Applied surface science*, vol. 321, pp. 226–232, 2014.

- [134] W.-K. Jo and N. C. S. Selvam, "Enhanced visible light-driven photocatalytic performance of zno-g-c3n4 coupled with graphene oxide as a novel ternary nanocomposite," *Journal of hazardous materials*, vol. 299, pp. 462–470, 2015.
- [135] H Munawaroh, P. Sari, S Wahyuningsih, and A. Ramelan, "The photocatalytic degradation of methylene blue using graphene oxide (go)/zno nanodrums," in *AIP Conference Proceedings*, AIP Publishing LLC, vol. 2014, 2018, p. 020 119.
- [136] M. Jabeen, M. Ishaq, W. Song, L. Xu, I. Maqsood, and Q. Deng, "Uv-assisted photocatalytic synthesis of zno-reduced graphene oxide nanocomposites with enhanced photocatalytic performance in degradation of methylene blue," *ECS Journal of Solid State Science and Technology*, vol. 6, no. 4, pp. M36–M43, 2017.
- [137] M. Azarang, A. Shuhaimi, R. Yousefi, A. M. Golsheikh, and M Sookhakian, "Synthesis and characterization of zno nps/reduced graphene oxide nanocomposite prepared in gelatin medium as highly efficient photo-degradation of mb," *Ceramics International*, vol. 40, no. 7, pp. 10 217–10 221, 2014.
- [138] J. He, C. Niu, C. Yang, J. Wang, and X. Su, "Reduced graphene oxide anchored with zinc oxide nanoparticles with enhanced photocatalytic activity and gas sensing properties," *RSC Advances*, vol. 4, no. 104, pp. 60 253–60 259, 2014.
- [139] T. Lv, L. Pan, X. Liu, T. Lu, G. Zhu, and Z. Sun, "Enhanced photocatalytic degradation of methylene blue by zno-reduced graphene

- oxide composite synthesized via microwave-assisted reaction,” *Journal of Alloys and Compounds*, vol. 509, no. 41, pp. 10 086–10 091, 2011.
- [140] F. S. Omar, H. Nay Ming, S. M. Hafiz, and L. H. Ngee, “Microwave synthesis of zinc oxide/reduced graphene oxide hybrid for adsorption-photocatalysis application,” *International Journal of Photoenergy*, vol. 2014, 2014.
- [141] H. Jung, T.-T. Pham, and E. W. Shin, “Interactions between zno nanoparticles and amorphous g-c3n4 nanosheets in thermal formation of g-c3n4/zno composite materials: The annealing temperature effect,” *Applied Surface Science*, vol. 458, pp. 369–381, 2018.
- [142] S Bouhouche, F Bensouici, M Toubane, A Azizi, A Otmani, K Chebout, F Kezzoula, R Tala-Ighil, and M Bououdina, “Effect of er<sup>3+</sup> doping on structural, morphological and photocatalytical properties of zno thin films,” *Materials Research Express*, vol. 5, no. 5, p. 056 407, 2018.
- [143] M. Hernández-Carrillo, R Torres-Ricárdez, M. García-Mendoza, E Ramírez-Morales, L Rojas-Blanco, L. Díaz-Flores, G. Sepúlveda-Palacios, F Paraguay-Delgado, and G Pérez-Hernández, “Eu-modified zno nanoparticles for applications in photocatalysis,” *Catalysis Today*, 2018.
- [144] S. Suwanboon, P. Amornpitoksuk, A. Sukolrat, and N. Muensit, “Optical and photocatalytic properties of la-doped zno nanoparticles prepared via precipitation and mechanical milling method,” *Ceramics International*, vol. 39, no. 3, pp. 2811–2819, 2013.
- [145] S. Kumar and P. Sahare, “Nd-doped zno as a multifunctional nanomaterial,” *Journal of rare earths*, vol. 30, no. 8, pp. 761–768, 2012.

- [146] E. Cerrato, C. Gionco, M. C. Paganini, E. Giamello, E. Albanese, and G. Pacchioni, "Origin of visible light photoactivity of the ceo<sub>2</sub>/zno heterojunction," *ACS Applied Energy Materials*, vol. 1, no. 8, pp. 4247–4260, 2018.
- [147] L. Zhu, H. Li, P. Xia, Z. Liu, and D. Xiong, "Hierarchical zno decorated with ceo<sub>2</sub> nanoparticles as the direct z-scheme heterojunction for enhanced photocatalytic activity," *ACS applied materials & interfaces*, vol. 10, no. 46, pp. 39 679–39 687, 2018.
- [148] M. Chelliah, J. B. B. Rayappan, and U. M. Krishnan, "Synthesis and characterization of cerium oxide nanoparticles by hydroxide mediated approach," *J. Appl. Sci*, vol. 12, no. 16, pp. 1734–1737, 2012.
- [149] C. Rodwihok, D. Wongratanaphisan, Y. L. Thi Ngo, M. Khandelwal, S. H. Hur, and J. S. Chung, "Effect of go additive in zno/rgo nanocomposites with enhanced photosensitivity and photocatalytic activity," *Nanomaterials*, vol. 9, no. 10, p. 1441, 2019.
- [150] A. R. Arakaki, S. M. Cunha, W. K. Yoshito, V. Ussui, and D. R. R. Lazar, "Influence of organic solvent on solvothermal synthesis of samaria and gadolinia doped ceria–nickel oxide composites," in *Materials Science Forum*, Trans Tech Publ, vol. 727, 2012, pp. 1317–1322.
- [151] C. Rodwihok, S. Choopun, P. Ruankham, A. Gardchareon, S. Phadungthitidhada, and D. Wongratanaphisan, "Uv sensing properties of zno nanowires/nanorods," *Applied Surface Science*, 2017.
- [152] M. Kurian and C. Kunjachan, "Investigation of size dependency on lattice strain of nanoceria particles synthesised by wet chemical methods," *International Nano Letters*, vol. 4, no. 4, pp. 73–80, 2014.

- [153] Y. Xu, J. Zou, X. Lin, W. Wu, W. Li, B. Yang, and M. Shi, "Quality-improved gan epitaxial layers grown on striped patterned sapphire substrates ablated by femtosecond laser," *Applied Sciences*, vol. 8, no. 10, p. 1842, 2018.
- [154] B. G. Mishra and G. R. Rao, "Promoting effect of ceria on the physicochemical and catalytic properties of ceo<sub>2</sub>-zno composite oxide catalysts," *Journal of Molecular Catalysis A: Chemical*, vol. 243, no. 2, pp. 204–213, 2006.
- [155] L. Lu, R. Li, T. Peng, K. Fan, and K. Dai, "Effects of rare earth ion modifications on the photoelectrochemical properties of zno-based dye-sensitized solar cells," *Renewable Energy*, vol. 36, no. 12, pp. 3386–3393, 2011.
- [156] S. K. Suram, P. F. Newhouse, and J. M. Gregoire, "High throughput light absorber discovery, part 1: An algorithm for automated tauc analysis," *ACS combinatorial science*, vol. 18, no. 11, pp. 673–681, 2016.
- [157] J. Gupta, J. Mohapatra, and D Bahadur, "Visible light driven mesoporous ag-embedded zno nanocomposites: Reactive oxygen species enhanced photocatalysis, bacterial inhibition and photodynamic therapy," *Dalton Transactions*, vol. 46, no. 3, pp. 685–696, 2017.
- [158] R. A. AbuMousa, U. Baig, M. A. Gondal, M. S. AlSalhi, F. Y. Alqahtani, S. Akhtar, F. S. Aleanizy, and M. A. Dastageer, "Photo-catalytic killing of hela cancer cells using facile synthesized pure and ag loaded wo 3 nanoparticles," *Scientific reports*, vol. 8, no. 1, pp. 1–11, 2018.
- [159] B. Chouchene, T. B. Chaabane, L. Balan, E. Girot, K. Mozet, G. Medjahdi, and R. Schneider, "High performance ce-doped zno nanorods for sunlight-

- driven photocatalysis,” *Beilstein journal of nanotechnology*, vol. 7, no. 1, pp. 1338–1349, 2016.
- [160] T. Xia, J. Zhao, P. Tang, L. Sun, and B. Pan, “Preparation of ce doped zno microspheres and its visible-light photocatalytic activity,” *Integrated Ferroelectrics*, vol. 197, no. 1, pp. 139–145, 2019.
- [161] C. Liu, J. Xu, S. Cui, and H. Yu, “Photocatalytic activity of ce-doped zno nanoparticles,” *Materials and Technology, China*, pp. 349–353, 2018.
- [162] N. F. Djaja, R. Saleh, *et al.*, “Characteristics and photocatalytic activities of ce-doped zno nanoparticles,” *Materials Sciences and Applications*, vol. 4, no. 02, p. 145, 2013.
- [163] S. Rajendran, M. M. Khan, F. Gracia, J. Qin, V. K. Gupta, and S. Arumainathan, “Ce 3+-ion-induced visible-light photocatalytic degradation and electrochemical activity of zno/ceo 2 nanocomposite,” *Scientific reports*, vol. 6, p. 31 641, 2016.
- [164] M. Samadi, M. Zirak, A. Naseri, E. Khorashadizade, and A. Z. Moshfegh, “Recent progress on doped zno nanostructures for visible-light photocatalysis,” *Thin Solid Films*, vol. 605, pp. 2–19, 2016.
- [165] C. B. Ong, L. Y. Ng, and A. W. Mohammad, “A review of zno nanoparticles as solar photocatalysts: Synthesis, mechanisms and applications,” *Renewable and Sustainable Energy Reviews*, vol. 81, pp. 536–551, 2018.
- [166] H. Park, Y. Park, W. Kim, and W. Choi, “Surface modification of tio<sub>2</sub> photocatalyst for environmental applications,” *Journal of Photochemistry and Photobiology C: Photochemistry Reviews*, vol. 15, pp. 1–20, 2013.

- [167] H. Park and W. Choi, "Photocatalytic reactivities of nafion-coated  $\text{tio}_2$  for the degradation of charged organic compounds under uv or visible light," *The Journal of Physical Chemistry B*, vol. 109, no. 23, pp. 11 667–11 674, 2005.
- [168] —, "Visible-light-sensitized production of hydrogen using perfluorosulfonate polymer-coated  $\text{tio}_2$  nanoparticles: An alternative approach to sensitizer anchoring," *Langmuir*, vol. 22, no. 6, pp. 2906–2911, 2006.
- [169] R. Guan, J. Li, J. Zhang, Z. Zhao, D. Wang, H. Zhai, and D. Sun, "Photocatalytic performance and mechanistic research of  $\text{zno/g-c}_3\text{n}_4$  on degradation of methyl orange," *ACS omega*, vol. 4, no. 24, pp. 20 742–20 747, 2019.
- [170] D. Dash, N. Panda, and D. Sahu, "Photoluminescence and photocatalytic properties of europium doped  $\text{zno}$  nanoparticles," *Applied Surface Science*, vol. 494, pp. 666–674, 2019.
- [171] T. Santhaveesuk, K. Shimano, K. Suematsu, and S. Choopun, "Size-independent and ultrahigh  $\text{co}$  gas sensor based on  $\text{tio}_2$  modified  $\text{zno}$  tetrapods," *physica status solidi (a)*, vol. 215, no. 14, p. 1 700 784, 2018.
- [172] H. Yu, P. Xiao, J. Tian, F. Wang, and J. Yu, "Phenylamine-functionalized  $\text{rgo/tio}_2$  photocatalysts: Spatially separated adsorption sites and tunable photocatalytic selectivity," *ACS applied materials & interfaces*, vol. 8, no. 43, pp. 29 470–29 477, 2016.



- [173] R. Köferstein, L. Jäger, and S. G. Ebbinghaus, “Magnetic and optical investigations on  $\text{LaFeO}_3$  powders with different particle sizes and corresponding ceramics,” *Solid State Ionics*, vol. 249, pp. 1–5, 2013.
- [174] H. Wu, S. Lin, C. Chen, W. Liang, X. Liu, and H. Yang, “A new  $\text{ZnO}/\text{rGO}/\text{polyaniline}$  ternary nanocomposite as photocatalyst with improved photocatalytic activity,” *Materials Research Bulletin*, vol. 83, pp. 434–441, 2016.
- [175] T.-D. Nguyen-Phan, E. J. Kim, S. H. Hahn, W.-J. Kim, and E. W. Shin, “Synthesis of hierarchical rose bridal bouquet-and humming-top-like  $\text{TiO}_2$  nanostructures and their shape-dependent degradation efficiency of dye,” *Journal of colloid and interface science*, vol. 356, no. 1, pp. 138–144, 2011.
- [176] T.-T. Pham, C. Nguyen-Huy, H.-J. Lee, T.-D. Nguyen-Phan, T. H. Son, C.-K. Kim, and E. W. Shin, “Cu-doped  $\text{TiO}_2$ /reduced graphene oxide thin-film photocatalysts: Effect of Cu content upon methylene blue removal in water,” *Ceramics International*, vol. 41, no. 9, pp. 11 184–11 193, 2015.

## Biography

<b>Name</b>	Chatchai Rodwihok (JC)
<b>Date of birth</b>	1989/08/10
<b>Education</b>	
2017-2020	Doctor of Philosophy ( <b>Chemical Engineering</b> ) School of Chemical Engineering University of Ulsan, South Korea
<b>*Thesis topic</b>	Surface modification of zinc oxide nanoparticles for improved photocatalytic properties <b>Supervisor:</b> Prof. Jin Suk Chung
2015-2017	Certificate of Korean Language Training ( <b>Intermediate Class</b> ) Sun Moon University, South Korea
2012-2014	Master of Science ( <b>Applied Physics</b> ) Department of Physics and Materials Science Chiang Mai University, Thailand
<b>*Thesis topic</b>	Synthesis and characterization of vertically aligned ZnO nanowires for gas sensor applications <b>Supervisor:</b> Assoc. Prof. Duangmanee Wongratanaphisan
2008-2012	Bachelor of Science ( <b>Physics</b> ) Department of Physics and Materials Science Chiang Mai University, Thailand
<b>*Thesis topic</b>	Numerical analysis of heavy rain and flooding in the south of Thailand from WRF simulation <b>Supervisor:</b> Asst. Prof. Wonchai Promnopas
<b>Scholarships</b>	Bachelor degree: POSN-Thai Government Master degree: Thailand Center of Excellence in Physics Doctoral degree: GKS-Korean Government
<b>Publications</b>	(First author) "UV sensing properties of ZnO nanowires/nanorods" <b>Applied Surface Science</b> , 2019 (IF: 5.155, Q1) "Effect of GO additive in ZnO/rGO nanocomposites with enhanced photosensitivity and photocatalytic activity" <b>Nanomaterials</b> , 2019 (IF: 4.034, Q1) "Cerium-oxide-nanoparticle-decorated zinc oxide with enhanced photocatalytic degradation of methyl orange" <b>Applied Science</b> , 2020 (IF: 2.217, Q1) "Improved photocatalytic activity of surface charge functionalized ZnO nanoparticles using aniline" <b>Applied Surface Science</b> , 2020 (IF: 5.155, Q1) – under reviewing